Universidade de Lisboa
Faculdade de Ciências
Departamento de Física

Bone recognition in UTE MR images by artificial neural networks for attenuation correction of brain imaging in MR/PET scanners

André Filipe dos Santos Ribeiro

Dissertação
Mestrado Integrado em Engenharia Biomédica e Biofísica
Perfil em Radiações em Diagnóstico e Terapia

2012

Universidade de Lisboa
Faculdade de Ciências
Departamento de Física

Bone recognition in UTE MR images by artificial neural networks for attenuation correction of brain imaging in MR/PET scanners

André Filipe dos Santos Ribeiro

Dissertação orientada por Professor Pedro Almeida e Dr. Rota Kops

Mestrado Integrado em Engenharia Biomédica e Biofísica

Perfil em Radiações em Diagnóstico e Terapia

2012

Acknowledgments

- First I want to thanks to Dr. Elena Rota Kops, who helped me finding a place to stay in Juelich, Germany. Moreover, I want to thanks her for the help in the development of the present work and on the revision of the written thesis.

- I want to thanks Prof. Pedro Almeida, who gave his disponibility to be my supervisor and which contact Prof. Hans Herzog for an opportunity in the Forschungszentrum Juelich, Juelich, Germany. Also, I want to thanks for the revision of the written thesis.

- To Prof. Hans Herzog for the opportunity to work in one of the best places regarding PET/MRI. For all the pacience regarding Erasmus/Thesis paperwork a sincerily thank you.

- To my girlfriend, Cláudia Lopes, who helped me when I most needed, who gave me her company and understanding in a very difficult year. Moreover, I want to thank her for the HUGE help in the development of the artwork developed for this thesis.

- To my friends Nuno Silva and João Monteiro, who helped me projecting, debugging and developing the ideas that made this thesis.

- To Philip Lohmann and Martin Weber for their friendship and integrating us in their environment.

- To the Erasmus Programme and University of Lisbon that partialy found my stay abroad.

- Last but not least to Prof. Guiomar Evans for helping me with the bureaucratic issues related to studing abroad.

- To whom I forgot to mention that helped directly on indirectly on the development of this work a honest THANK YOU!

Resumo

Para a quantificação em Tomografia por Emissão de Positrões (PET, acrónimo em inglês para Positron Emission Tomography) a correcção da atenuação de fotões (AC, acrónimo em inglês para Attenuation Correction) nos tecidos é essencial. Actualmente, técnicas híbridas como a combinação de PET com Tomografia Axial Computurizada (CT, acrónimo em inglês para Computed Tomography) benficiam do mapa de correcção da atenuação que deriva da imagem de CT. Esta modalidade combina análise funcional de PET com análise anatómica de CT, oferecendo uma grande vantagem sobre PET convencional. Protótipos clínicos de equipamentos conjugando as técnicas de PET e Ressonância Mágnetica (MR, acrónimo em inglês para Magnetic Ressonance) têm também vindo a ser desenvolvidos datando desde os finais de 1990.

Grandes vantagens de PET/MR comparativamente com PET/CT podem ser enumeradas: O MR proporciona um contraste superior ao CT; o CT leva a adição de dose radiativa enquanto que o MR não; Imagem simultânea por CT não é possível enquanto que por MR é.

Contudo, as imagens de MR não são capazes de proporcionar mapas de correcção de atenuação como as imagens de CT. Os vóxeis das imagens de MR correlacionam-se com a densidade dos núcleos de hidrogénio nos tecidos e com as propriadades de relaxamento dos mesmos, ao invés dos coeficientes de atenuação de massa relacionados com a densidade electrónica. Consequentemente, os métodos de AC por MR são bastante mais complicados do que os métodos de AC por CT.

Dois grupos metodológicos de AC baseados em MR têm sido propostos: abordagens por segmentação das imagens de MR e abordagens por template/atlas. O primeiro efectua a segmentação das imagens de MR em n estruturas, sendo dados coeficientes de atenuação especificos válidos para 511keV para cada estrutura. O segundo funciona segundo um template de MR e correspondente template de atenuação ou uma base de dados MR/CT. No primeiro caso, o template de MR é registado não-linearmente para a imagem especifica de MR do paciente e as mesmas transformações são aplicadas ao template de atenuação, gerando um mapa de atenuação especifico para o paciente. No segundo caso, a

combinação de reconhecimento de padrões locais com registo atlas origina uma imagem pseudo-CT que é posteriomente transformada para ser usada como mapa de atenuação.

Estas técnicas contudo ainda apresentam desvantagens: a técnica de AC por segmentação de MR depende da implementação do método de segmentação, bem como do número de estruturas segmentadas. Por outro lado, as técnicas de AC por template/atlas são difíceis de generalizar para corpo inteiro devido à variabilidade entre sujeitos.

Neste trabalho foram desenvolvido dois métodos de AC que discriminam ar, tecidos moles e osso baseados em intensidade de MRI. Isto é efectuado pela acquisição de imagens com uma sequência de MR denomidada tempo de eco ultra curto (UTE, acrónimo em inglês para Ultrashort Echo Time). Adicionalmente, uma imagem de template de atenuação é usada para guiar a classificação dos três tecidos e para derivar dois métodos contínuos novos.

Uma sequência UTE de MR foi adquirida em 9 sujeitos com 2 tempos de eco (0.07 e 2.46 ms) resultando em 2 imagens para cada sujeito. Adicionalmente foi adquirida 1 imagem de CT para cada paciente. 3 tipos de artefactos nas imagens adquiridas foram identificados, sendo artefactos de movimento e inomogenidades de intensidade nas imagens de MR, e artefactos de metal nas imagens de CT. Adicionalmente, problemas de coregisto entre a imagem de CT e de MR foram verificados.

O coregisto perfeito entre as imagens de CT e MR é complicado uma vez que as modalidades não são adquiridas nos mesmos scanners. Também, em alguns casos, a orientação da cabeça no scanner de CT é bastante diferente da orientação da cabeça no scanner de MR, resultando em grandes diferenças entre a imagem de CT e de MR. Estas diferenças podem influenciar os métodos de AC de duas formas: Em primeiro lugar os métodos de AC que optimizam os seus parâmetros de uma forma autónoma usam normalmente uma imagem referência como por exemplo uma imagem de CT coregistada com as imagens de MR do sujeito. Se a imagem de CT não estiver perfeitamente coregistada os métodos autónomos não são óptimos. Em segundo lugar a interpretação dos métodos de AC por comparação do mapa de AC gerado e derivado por CT não é inteiramente correcta.

Apesar de os artefactos de metal serem um problema para sequências típicas de MR, foi mostrado terem pouco impacto nas imagens de UTE. Contudo as imagens de CT apresentam artefactos de risca nas imediações dos implantes metálicos (3 em 9 sujeitos).

Ao contrário dos artefactos de metal, os artefactos de movimento afectam as imagens de MR. Foi mostrado que os dados analisados são largamente afectados por artefactos de movimento (5 em 9 sujeitos). Isto

causa um grande problema na derivação dos mapas de AC para o sujeito por qualquer método que use directamente as intensidades de MR das imagens corrompidas por este artefacto.

Inomogeneidades das intensidades de MR também foram identificados nas imagens de UTE. Este tipo de artefacto pode causar problemas na derivação do mapa de AC para o sujeito dependente da sua magnitude e de como influencia individualmente as diferentes imagens de UTE.

Para corrigir as inomogeneidades de campo antes da estimação do mapa de AC, foi apresentado um método para corrigir múltiplas imagens que não necessita de qualquer tipo de hardware adicional e é baseado na minimização da variação de informação.

É mostrado que o método proposto reduz as inomogeneidades de campo das imagens corruptas enquanto mantém (até um certo ponto) as imagens não corrompidas por ruído. Em imagens simuladas obtidas da base de dados do Brainweb a redução das inomogeneidades em todos os casos testados é reduzida drasticamente e aproxima as imagens de imagens não corrompidas por inomogeneidades de campo. Contudo, o método apresenta uma sobre-compensação dos efeitos das inomogeneidades e uma condição de paragem que não baseada apenas no número de iterações deve ser desenvolvida para evitar este problema. O método de correcção de inomogeneidades de campo foi também aplicado às imagens de MR obtidas e foi observado que o coeficiente de variação para os tecidos relevantes à estimação de AC decresceu após a aplicação da correcção, indicando maior homogenidade nestes tecidos após a correcção. Adicionalmente a comparação da classificação das imagens de MR em três tecidos (ar, osso e tecidos moles) antes e após a correcção de inomogeneidades foi efectuada. Foi observado que quando as imagens de MR não foram corrigidas para as inomogeneidades de intensidade uma sobreclassificação do osso na região ocipital foi verificada. Mais, perto do seio frontal a correcção das inomogeneidadas mostrou um melhoramento na classificação do osso e tecidos moles.

Como foi introduzido, as limitações dos métodos de AC actuais derivam do facto de que a informação anatómica introduzida pelas imagens de atlas e template ou a optimização de alguns parâmetros, subjectivos e difíceis de definir, são necessários para uma boa estimação do mapa de AC.

Desta forma três abordagens de redes neuronais artificais(ANN acrónimo do inglês para artifical neural networks) foram desenvolvidas: Mapa de organização autónoma (SOM acrónimo do inglês para Self-Organizing Map), rede neuronal alimentada para a frente (FFNN acrónimo do inglês para feedforward neural network) e uma rede neuronal probabilistica (PNN, acrónimo do inglês para probabilistic neural network). Estes

tipos de ANN foram escolhidos devido à sua rápida e fácil optimização de parâmetros.

A PNN tal como a FFNN são algoritmos de aprendizagem supervisionada. Contudo, o passo de aprendizagem da PNN é feito num passo único e simples. A PNN não necessita de grandes quantidades de dados e classifica eficientemente diferentes tipos de dados. Contudo, dos métodos propostos é a que requer maior intervenção pelo utilizador e o segundo mais lento (a seguir ao SOM). A SOM é um tipo de ANN que é treinada usando aprendizagem não supervisionada para produzir uma representação discreta e de menor complexidade do espaço de entrada. SOMs reduzem a complexidade dos sistemas produzingo um mapa com usualmente 1 ou 2 dimensões que apresenta as similaridades dos dados agrupando dados semelhantes perto uns dos outros. Desta forma SOM tenta aprender os padrões implícitos nos dados de entrada e retorna à saída uma imagem com diferentes classes sem a intervenção do utilizador.

As diferentes análises mostraram resultados ligeiramente diferentes relativamente ao método que obteve os melhores resultados. Contudo, todas as análises mostraram que os métodos desenvolvidos são mais precisos que os métodos currentemente utilizados. Os métodos ajudados pela imagem de template mostraram ser mais robustos e de mais especificidade que os métodos que não usaram template, contudo mostraram perder sensibilidade. Os métodos contínuos desenvolvidos mostraram-se promissores sendo que podem estimar diferentes coeficientes de atenuação dentro de um determinado limite para o mesmo tecido e assim contar com diferentes densidades para o mesmo tecido. Finalmente, esta tese mostra que AC por MR é possível e melhoramentos das técnicas propostas podem levar ao seu uso em scanners de PET/MR evitando a acquisição de uma imagem de CT e desta forma reduzindo a dose radiativa pelo paciente.

Abstract

Aim: Due to space and technical limitations in PET/MR scanners one of the difficulties is the generation of an attenuation correction (AC) map to correct the PET image data. Different methods have been suggested that make use of the images acquired with an ultrashort echo time (UTE) sequence. However, in most of them precise thresholds need to be defined and these may depend on the sequence parameters. In this thesis different algorithm based on artificial neural networks (ANN) are presented requiring little to any user interaction. **Material and methods:** An MR UTE sequence delivering two images with 0.07 ms and 2.46 ms echo times was acquired from a 3T MR-BrainPET for 9 patients. To correct for intensity inhomogeneities prior to attenuation map estimation a method based on multispetral images was developed and used to correct both images from UTE sequence. The training samples from the corrected images were feed to the proposed algorithms for learning and the methods posterior used for classification. The generated AC maps were compared to co-registered CT images based on the co-classification voxels, dice coefficients and sensitivity correction map (for the 9 patients), and relative differences (for 4 patients) in reconstructed PET images. **Results:** In overall the methods proposed showed high dice coefficients for air and soft tissue and lower to bone. Adittionaly, the proposed methods showed to present higher dice coefficients than remain methods. High linear correlation between the sensitivity correction maps was verified for all methods. The reconstructed PET images showed mean relative differences 5% for all methods except keereman method, where a mean of 6% was observed. **Discussion:** The different analysis showed slightly different results regarding the methods that perform best. Nevertheless, all the analysis showed that the methods developed work similar to better than the ones curently proposed. **Conclusion:** The methods aided by the template image showed to be more robust and with higher specificity than the ones without, altough loosing in sensitivity. Finally, the continuous methods developed showed to be promising as they can estimate different attenuation coefficients within a certain range for the same tissue and therefore account for different densities.

Contents

List of Figures

List of Tables

List of Abbreviations

AC Attenuation Correction

ACF Attenuation Correction Factor

ANN Artificial Neural Networks

APD Avalanche PhotoDiode

BL Blank Scan

BP Break Point

CJV Coefficients of Joint Variation

CT Computed Tomography

CV Coefficients of Variation

eV Electron Volt

FCUL Faculty of Sciences of the University of Lisbon

FFNN Feedforward Neural Network

FID Free Induction Decay

FOV Field Of View

FWHM Full Width Half Maximum

GE Gradient Echo

HL Hidden Layer

HU Hounsfield Units

IH Intensity Inhomogeneities

IL Input Layer

JE Joint Entropy

LOR Line Of Response

MARS Metal Artefact Reduction Sequence

MI Mutual Information

ML Maximum Likelihood

MLEM Maximum Likelihood Expectation Maximization

mMR Molecular Magnetic Ressonance

MR Magnetic Ressonance

MRI Magnetic Ressonance Imaging

nCJV Normalized Coefficients of Joint Variation

NMR Nuclear Magnetic Ressonance

OL Output Layer

OSEM Ordered Subsets Expectation Maximization

PD Proton Density

PET Positron Emission Tomography

PL Pattern Layer

PMT PhotoMultiplier Tube

PNN Probabilistic Neural Network

PVE partial Volume Effect

RF Radio Frequency

ROI Region Of Interest

SE Spin Echo

SiPM Silicon PhotoMultiplier

SL Summation Layer

SNR Signal to Noise Ratio

SOM Self-organizing Map

SPECT Single-Photon Emission Computed Tomography

SPM Statistical Parametric Mapping

T1 Spin-Lattice Relaxation Time

T2 Spin-Spin Relaxation Time

TE Echo Time

TR Repetition Time

TX Transmission Scan

UL University of Lisbon

UTE Ultrashort Echo Time

UTE1 1st echo image from UTE sequence

UTE2 2nd echo image from UTE sequence

VI variation of information

VOI Volume Of Interest

Chapter 1

Introduction

1.1 Situation/Aim/Purpose

For quantitative information of Positron Emission Tomography (PET) the attenuation correction (AC) of the photons in tissue is essential. In conventional PET (standalone PET) the distribution of the AC map is obtained by a transmission scan that uses either a point source containing a single-photon emitter [Karp et al., 1995] or a line source containing a positron emitter [Bailey, 1988]. On the other hand, in a multi-modal PET-CT technique, the AC map is derived from the Computer Tomography (CT) scan [Kinahan et al., 1998, Zaidi and Hasegawa, 2003].The latter technique combines functional analysis from PET with anatomical analysis from CT, giving a great advantage over standalone PET. This combination of functional and anatomical information is no more exclusive of PET/CT. A new modality has emerged combining PET and Magnetic Resonance Imaging (MRI). The first images of this multi-modal technique were reported in [Schlemmer et al., 2008].

Some great advantages of PET/MRI compared to PET/CT can be such as: CT does not provide the excellent contrast of soft tissues that MRI offers, CT leads to an addition of radiation dose and finally simultaneous imaging is not possible. However, MR images cannot directly provide AC maps as a CT scan is able. In short, CT images are produced at effective energies of 50-70 keV [Beyer et al., 1995] representing the actual AC distribution, thus providing a direct electronic density measure of the image volume. The CT-AC is calculated from the transformation of the CT attenuation values into the corresponding linear attenuation coefficients at 511 keV valid for PET. Because the voxels of the MR images correlate with the hydrogen nuclei density in tissues and with the relaxation properties of tissues, instead of with the mass attenuation coefficients related to the electronic density, the MR-based AC results to

be much more complicated than the CT-based AC.

Although preclinical prototypes of PET/MR scanners started in the late 1990's [Shao et al., 1997] MR-AC is still under development. Two methodological groups for MR-based AC have been focused: MR segmentation approaches and template/atlas-based approaches. The former performs a segmentation of the MR image into n structures, being assigned a specific AC valid for 511 keV to each structure [Schreibmann et al., 2010]. The latter follows from an MR template and the corresponding attenuation template [E.Rota Kops et al., 2009] or from a MR/CT database [Hofmann et al., 2008]. In the template method, the MR template is non-linearly registered to the patient's MR image of the patient and the same spatial transformations are then applied to the attenuation template, generating a specific attenuation map of the patient. In the atlas method, a combination of local pattern recognition and atlas registration yields a pseudo-CT image, which is used for AC after transformation into attenuation maps.

These techniques still present some drawbacks: the techniques of MR-based AC by segmentation depend on the implemented segmentation algorithm as well as on the number of segmented structures. On the other hand, the MR-based AC techniques by template/atlas are difficult to generalize to a whole-body AC, due to intersubject variability. For instance, the gas sacs in the abdominal region in a specific patient do not have corresponding in a typical template.

In this work, two different MRI-based attenuation correction methods were developed which are able to discriminate air, soft tissue and bone on the base of MRI intensity alone. This is done by acquiring images with an ultrashort echo time (UTE) MR sequence. Additionally, an attenuation template image was used to guide the classification of the 3 tissues and also for deriving 2 new continuous methods.

1.2 Outline

In chapter 2 the different image modalities used in this work are presented. First the principles of MR, from the basic principles to the image sequences and image degrading effects are introduced. An overview of the MRI hardware is also presented. Next the principles of PET are described from the basic principles to imaging principles and reconstruction. Also PET hardware is refereed. The last part of this chapter will cover the hybrid technique MR/PET, the advantages and design problems that arise from the combination of PET and MRI. The developed systems for the hybrid PET/MR are finally overview.

In chapter 3, as it is the focus of this work, the effect of attenuation

on the reconstructed images is discussed as well as the implementation of AC into the reconstruction algorithm. Finally, the different methods that can be used to derive the AC map are described, with special attention for the MRI-based attenuation correction methods that have been proposed.

In chapter 4 an analise of the most important artefacts that influence AC map estimation is described.

In chapter 5 and 6 the method developed is presented: pre-processing of the MR images, such as a new method for correction of field inhomogeneities in the MR images (chapter 5), and estimation of AC maps based on artificial neural networks (chapter 6). Further, the results obtained from the presented methods from those proposed by [Catana et al., 2010, Keereman et al., 2010, Rota Kops and Herzog, 2007] and those obtained from corresponding CT images are compared. Finally, the results are discussed and a conclusion to the presented and current published methods is given.

In chapter 7 a summary of the work at hand is shown, as well as, the future prospects of MR-based methods for AC map estimation.

Chapter 2

Hybrid medical imaging

2.1 Introduction

In this chapter the different image modalities used in this work are presented.

In section 2.2 the principles of MRI, from the most basic, such as spin principles, are briefly explained. The imaging principles of MRI, as well as, the most important MRI sequences and the UTE sequence which plays an important role in the presented work, are also presented. Furthermore, the image degrading effects due to the MR scanner or the patient are covered. Finally an overview of the main MRI hardware is introduced.

In section 2.3 the basic principles of PET are explained. The image degrading effects in PET are introduced briefly, leaving the attenuation effect (the theme of this work) for the next chapter. The two implemented image reconstruction techniques are explored and the advantages of each of them are given. Finally as in the previous section an overview of the main PET hardware is introduced.

In the last section (2.4), the hybrid technique PET/MR is covered with the advantages and design problems that arise from the combination of both modalities. Finally the developed systems for the hybrid PET/MR are overview.

2.2 Magnetic Resonance Imaging

2.2.1 Nuclear magnetic resonance (NMR): physical principles

2.2.1.1 Nuclear spin

All nucleons (neutrons and protons), composing any atomic nucleus, have one intrinsic quantum property named spin. The overall spin of the nucleus is determined by the spin quantum number s. The allowed values for s are non-negative integers or half-integers. Fermions (such as electrons, protons or neutrons) have half-integer values, whereas bosons (such as photon or mesons) have integer spin values. In atomic physics, the spin quantum number is a quantum number that parametrizes the intrinsic angular momentum of a given particle. The spin angular momentum, m_s, range from -s to s in integer steps, giving two possible angular momentum for fermions of -1/2 and +1/2 and three possible angular momentum for bosons of -1, 0, +1. It is this propriety that confers the different magnetic characteristics to the atomic nucleus.

Given an arbitrary direction z (usually determined by an external magnetic field) the spin z-projection can be related with the Planck's constant, h and the spin angular momentum m_s, Equation 2.1.

$$S_z = m_s h/(2\pi) \tag{2.1}$$

In the atomic nucleus protons and neutrons can pair in the same way as electrons in chemical bonds (one with a spin of +1/2 and one with a spin of -1/2) reducing the net spin to 0. Unpaired protons and neutrons contribute with 1/2 to the net spin of the nucleus, and when the overall is larger than 0 the nucleus will present a spin angular momentum and an associated magnetic moment μ. Some of the frequently used isotopes in NMR are presented in Table 2.1.

Table 2.1: Used isotopes in NMR,[Prasad, 2006].

Nucleus	Spin number	γ(MHz/T)
1H	1/2	42.576
13C	1/2	10.705
19F	1/2	40.053
23Na	3/2	11.262

The magnetic moment μ is linearly related to the spin quantum number s by the gyromagnetic ratio γ, Equation 2.2.

$$\mu = \gamma S \tag{2.2}$$

In NMR, not a single particle, but the overall particles are observed, Figure 2.1.

Regarding the first component (XY plane), in a steady state (without any external influence) the magnetic momentum of each particle in that plane is random and therefore it sums to 0. Regarding the second component if the particle is under a magnetic field the magnetization vector in that direction is not 0.

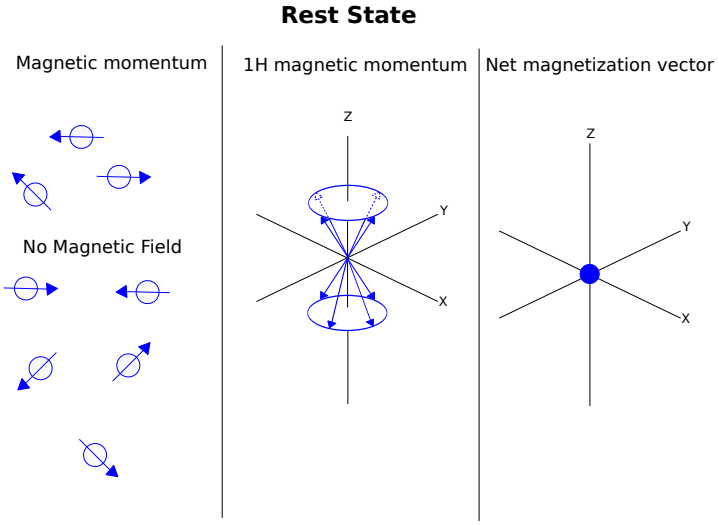

Figure 2.1: Illustration of single particle momentum and resulting net magnetization vector. When no magnetic field is applied the magnetic momentum of each particle can have a component in either X, Y or Z directions, and therefore both the component in the XY plane and the component oriented to the Z axis in the net magnetization vector are 0.

A conversion from the magnetic momentum of a single particle to the total magnetization of a whole volume must be performed. This is fairly simple as the total magnetization can be described as a net magnetization vector ($\vec{M}$) given by the sum of all particles' magnetic momentum, Equation 2.3.

$$\vec{M} = \sum \vec{\mu_i} \tag{2.3}$$

As the magnetic momentum of each particle can have a component in either X, Y or Z direction the net magnetization vector can also have a component in each of those directions. Two components of the magnetization vector are usually important in the study of NMR, namely the component in the XY plane and the component oriented to the Z axis.

Regarding the first component (XY plane), in the steady state (i.e. without any external influence) the magnetic momentum of each particle in that plane is random and therefore the overall sum equal to 0. Regarding the second component (Z direction) if the particle is under a magnetic field the magnetization vector in that direction is not 0. An example will be used to better explain this phenomenon.

For 1H (1 proton) only two magnetic momenta are allowed (+1/2 and -1/2) and the energy of both states is the same, therefore the number of atoms in each state is the same. Although if the proton is placed in a magnetic field the axis of the angular momentum coincides with the field direction and the resultant magnetic momentum does not have the same energy for the two states. The state which has the z-component parallel with the external field B_0 presents a lower energy than the state with the z-component anti-parallel with the external field B_0. The energy of these states is thus related with the magnetic moment μ_z and the external field B_0, Equation 2.4.

$$E = -\mu_z B_0 \tag{2.4}$$

Consequently the two states will no more have the same number of atoms in each state. At room temperature the number of particles oriented along the level of lower energy [Prasad, 2006], N^+, exceeds slightly the upper level N^-, in accordance to the Boltzmann statistics, Equation 2.5 (with k=1.3805 $\times$ 10^{-23} J/Kelvin and T in Kelvin).

$$N^-/N^+ = e^{-E/kT} \tag{2.5}$$

Due to the zero XY component and the overpopulation of particles oriented towards the external field the net magnetization vector has only one component in the z direction that points to the external field, Figure 2.2.

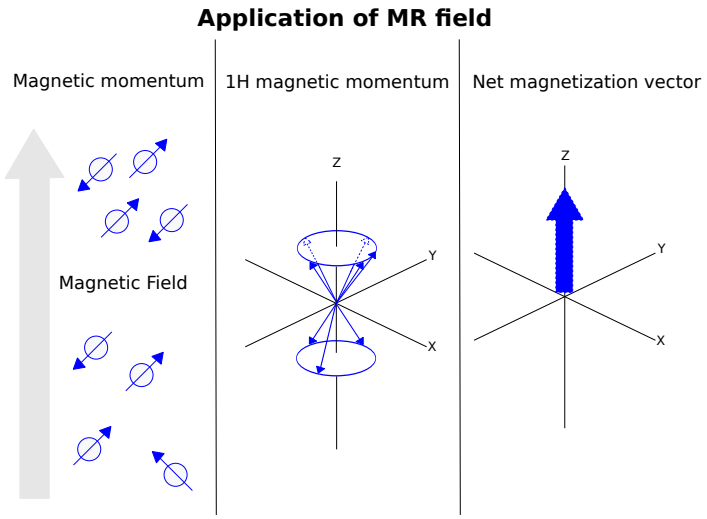

Figure 2.2: Illustration of single particle momentum and resulting net magnetization vector. When a magnetic field is applied in the Z direction more particles align parallel than anti-parallel to the direction of the magnetic field and a net magnetization vector parallel to the magnetic field is generated.

2.2.1.2 RF excitation and flip angle

It is possible that spin transition from one state to the other one happens by supplying energy to the net magnetization. This energy, however, must be equal to the energy transition of the two states, Equation 2.6 (derived from Equations 2.1, 2.2 and 2.4).

$$\Delta E = E^- - E^+ = \gamma B_0 h/2\pi \tag{2.6}$$

As the energy of the photon is given by $w_0 h/2\pi$, Equation 2.6 can be transformed into Equation 2.7, in which w_0 is the Larmor frequency.

$$w_0 = \gamma B_0 \tag{2.7}$$

For common isotopes used in NMR the Larmor frequency can be calculated by multiplying the gyromagnetic ratio γ of the isotope from Table 2.1 with the applied external field B_0 .

Giving a radio frequency RF field in the XY plane with the Larmor frequency, the particles in the spin-up state can therefore transit to the spin-down state. Adding to this effect, the individual particles will rotate in phase (phase coherence) allowing a transverse magnetization to appear. Regarding to the net magnetization vector the RF field will lead to the rotation of this vector, and the angle of rotation (flip angle, α)

depends only on the amplitude of the B1 field and the duration of the pulse, Equation 2.8, Figure 2.3.

$$\alpha = \gamma B_1 t \tag{2.8}$$

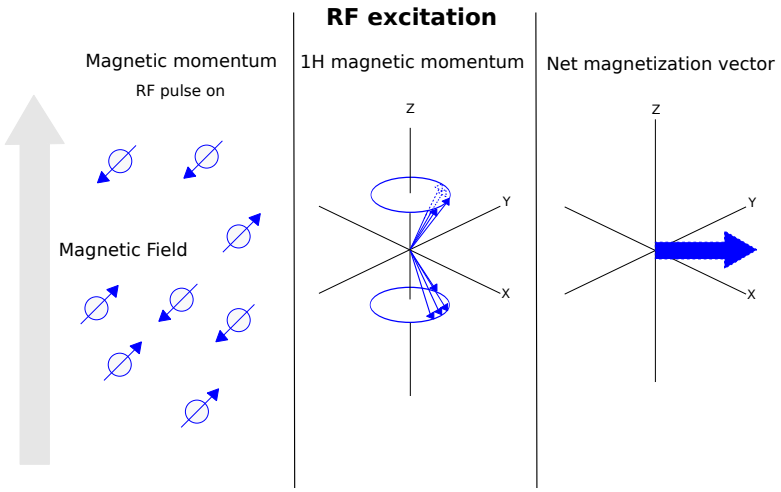

Figure 2.3: Illustration of single particle momentum and resulting net magnetization vector. When a RF pulse in the XY plane is applied along a static magnetic field in the Z direction the particles in the spin-up state can transit to the spin-down state direction decreasing the net magnetization vector in the Z direction. Moreover, the individual particles will rotate in phase (phase coherence) allowing a transverse magnetization (XY plane) to appear.

2.2.1.3 Relaxation

As the RF pulse is stopped the particles return to the rest state as well as the net magnetization vector, Figure 2.4. For this to happen the particles emit an RF wave with the Larmor frequency, being this wave called the free inductive decay (FID).The return to the equilibrium state is called relaxation and is governed by two physical phenomena: spin-lattice relaxation and spin-spin relaxation.

As the spins return to the spin-up state, the longitudinal component of the net magnetization vector returns to the rest state (spin-lattice relaxation). The equation that describes how the system returns to the equilibrium state (rest) after stimulation along the magnetization Mz is given according to Equation 2.9, being T1 the spin-lattice relaxation time.

$$Mz = M0 \times \left(1 - \mathrm{e}^{-t/T1}\right) \tag{2.9}$$

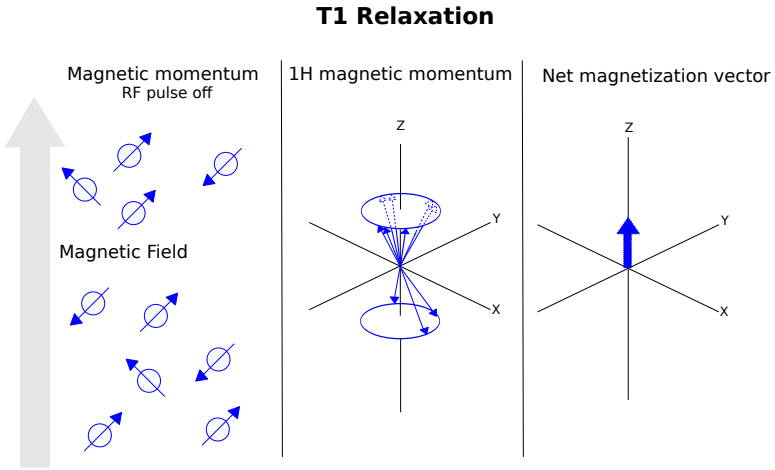

Figure 2.4: Illustration of single particle momentum and resulting net magnetization vector. When the RF pulse in the XY plane is stopped the spins return to the spin-up state, and therefore the longitudinal component of the net magnetization vector returns to the rest state.

Moreover, after stimulation the net magnetization starts to dephase (spin-spin relaxation), due to the inhomogeneities of the magnetic field B0 and the interaction between molecules, Figure 2.5. The equation that describes how the transverse magnetization Mxy returns to equilibrium is given accordingly to Equation 2.10, being T2 the spin-spin relaxation time.

$$\mathrm{Mxy} = \mathrm{Mxy}_0 \times \mathrm{e}^{-t/T2} \tag{2.10}$$

Both T1 and T2 relaxation times are dependent on the material composition and consequently also the acquired NMR signal. T1 and T2 relaxation times for some of the human head tissues are given in Table 2.2.

Table 2.2: T1 and T2 relaxation times for some human head tissues at 3T, [de Bazelair and Duhamel, 2004, McRobbie et al., 2007, Wansapura and Holland, 1999].

Tissue	T1(ms)	T2(ms)
white matter (brain tissue)	832	110
gray matter (brain tissue)	1331	80
CSF	3700	-
Muscle	898	29
Fat	382	68

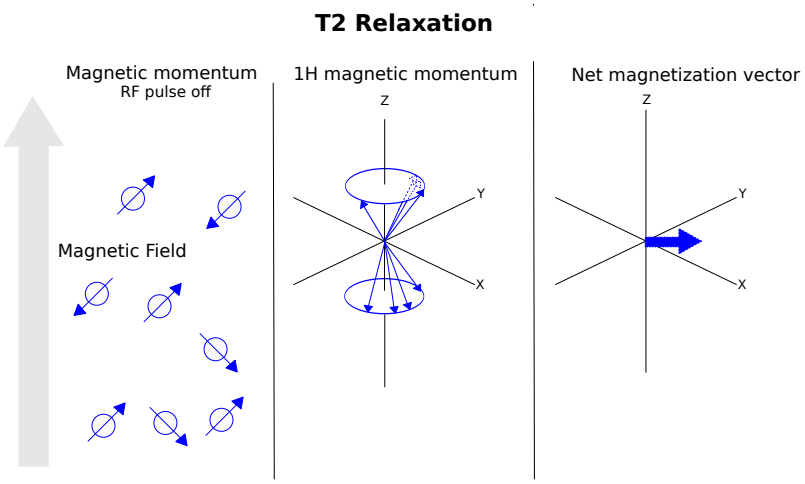

Figure 2.5: Illustration of single particle momentum and resulting net magnetization vector. When the RF pulse in the XY plane is stopped the net magnetization start to dephase and therefore the transverse component of the net magnetization vector returns to the rest state.

2.2.2 Imaging principles

2.2.2.1 Volume selection

In principle the resonance frequency of a spin is proportional to the field applied, as it was shown by Equation 2.7. So in the case of static field, B_0, all the spins under study will have the same resonance frequency. Therefore, if an RF pulse is applied with a bandwidth that contains the resonance frequency of one spin all spins will be excited, because they have the same resonance frequency. However, if each plane experiences a different field, the resonance frequency for the spins in the different planes will be different, and an RF pulse with a specific bandwidth (Δz) can be used to excite spins in a certain plane and not in the whole image. This can be accomplished using a magnetic field gradient, $B_1(z)$. With a magnetic field gradient the amplitude of the magnetic field varies with position, and consequently the resonance frequency, Figure 2.6. Equation 2.11 reflects how the resonance frequency changes with position:

$$\omega(z) = \gamma(B_0 + B_1(z)) \tag{2.11}$$

The thickness of the excited slice is then dependent on the bandwidth of the RF pulse and the steepness of the gradient, Equation 2.12.

$$\Delta z = \frac{\Delta w}{\gamma B_1(z)} \tag{2.12}$$

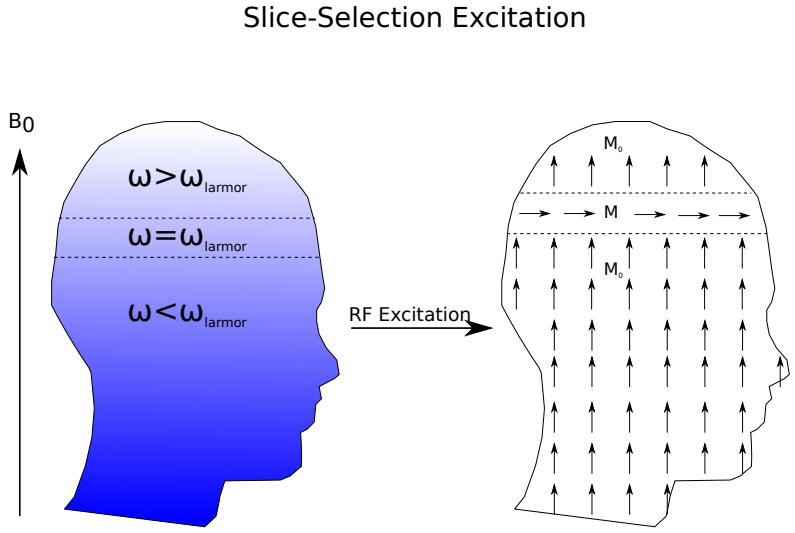

Figure 2.6: Illustration of slice selection excitation. Only the spins that precess at the Larmor frequency will be excited by the RF pulse and a transverse magnetization appears. Adapted from [Prasad, 2006].

2.2.2.2 Frequency and Phase encoding

To apply volume selection gradients in X (G_x) and Y (G_y) direction and perpendicular to the external field are used to encode frequency and phase information, respectively. Note that if a frequency encoding gradient is used in X direction, the phase encoding gradient must be used in the Y direction.

The frequency encoding gradient is used to impose a specific resonance frequency to the spins. Let's say, for example, that 3 spins from a certain volume due are excited due to volume selection. They will therefore exhibit the same resonance frequency and precess in phase. If we plot the amplitude of the signal retrieved against the frequency only one peak will be visible ($w_1 = w_2 = w_3$), because the field is the same for all the spins, Figure 2.7.

However, if each region (each line of the plane) experiences a different field, the resonance frequency for spins in the different regions will be different ($w_1 \neq w_2 = w_3$). With the frequency encoding gradient the amplitude of the magnetic field varies with position, and consequently the resonance frequency. In the example shown above, the 3 spins will no more experience the same field, and two peaks will appear, Figure 2.8.

The phase encoding gradient is used to impose a specific phase angle

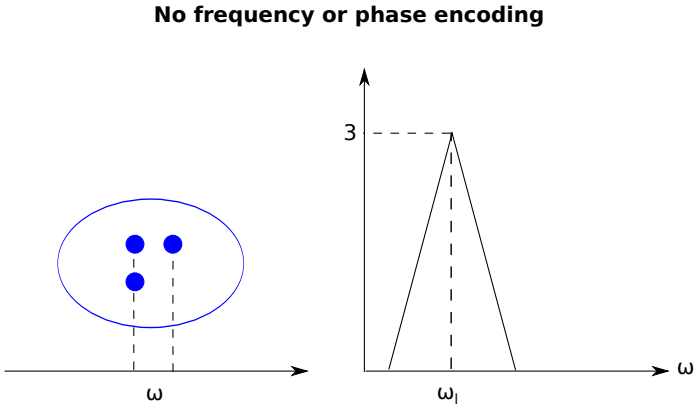

Figure 2.7: Ilustration of frequency and phase encoding. When no gradient is applied, all spins present the same frequency, therefore the final signal is grouped in a single frequency.

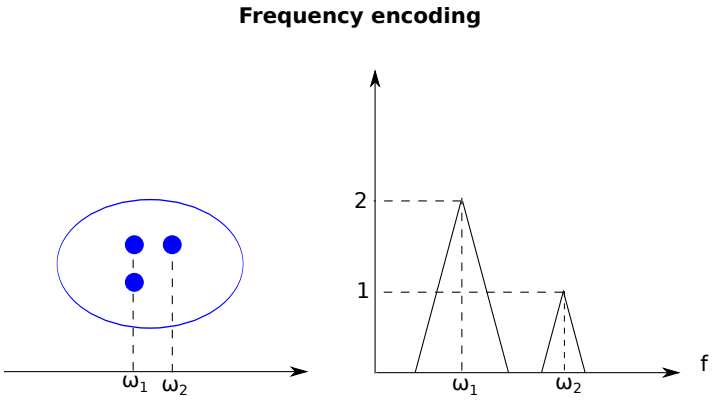

Figure 2.8: Ilustration of frequency and phase encoding. When a frequency gradient is applied, different lines experience a different frequency; therefore the signal from different lines is represented at different frequencies.

to a transverse magnetization vector. Let's say for example that the 3 spins are precessing as shown in Figure 2.9. If a gradient is applied in X or Y direction, the 3 spins will precess at different frequencies. When the gradient is turned off the resonance frequency experienced by the 3 spins is the same, but their phase is not.

Now the spins are coded in all 3 directions (x, y and z) and an image can be reconstructed by applying an inverse 3D Fourier transform on the recorded signal. In MRI the spatial frequency domain is called k-space in MRI and was introduced by Ljunggren [1983] and Twieg [1983].

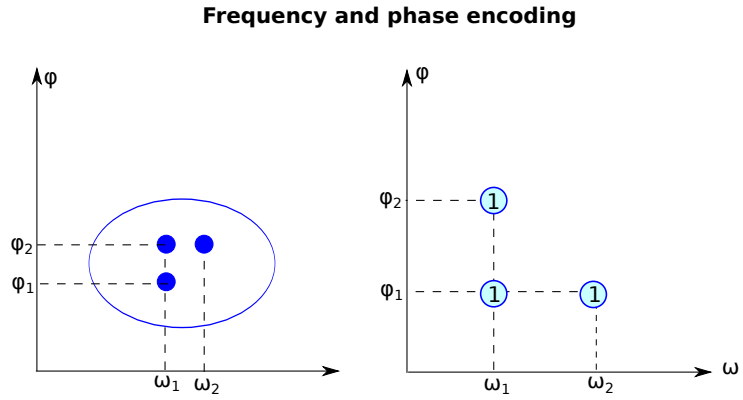

Figure 2.9: Ilustration of frequency and phase encoding. When a frequency and phase encoding gradients are applied each point will present a different frequency and phase, therefore the signal from each spin can be fully decorrelated.

2.2.2.3 Image Sequences

A pulse sequence is simply the definition of RF and gradient pulses, where the time interval between pulses their amplitude and the shape of the gradient affect the characteristics of the MR image. The programming of MRI pulse sequences is complex, but a deep understanding of it is essential for the acquisition of images with different kinds of contrast.

Most sequences are described by the repetition time (TR) and the echo time (TE) in milliseconds, and in case of a gradient echo sequence, by the flip angle.

There are two fundamental types of MR pulse sequences: Spin Echo (SE) and Gradient Echo (GE) sequences. The remaining developed MR sequences derive in some way from the combination of the SE and GE sequences.

2.2.2.3.1 Spin Echo (SE) Sequence In SE sequences, a 90° pulse flips the net magnetization vector into the transverse plane. When the RF pulse is stopped the spins start to dephase due to T1, T2 and T2* relaxations processes. To rephase the spins an 180° RF pulse is applied. During this pulse the spins, that were dephasing at a quicker rate will also rephase at a quicker rate, so that an echo is created (when the spins are rephasing).

A simple diagram of a conventional SE sequence is shown in Figure 2.10, [Prasad, 2006]. An 90° RF pulse is applied along with a slice selective gradient. After the RF pulse, G_x and G_y gradients are applied to spatial localize the spins. An 180° pulse is thereafter applied to rephase

the spins along with the same slice selective gradient. The signal (echo) is then acquired at a time around TE.

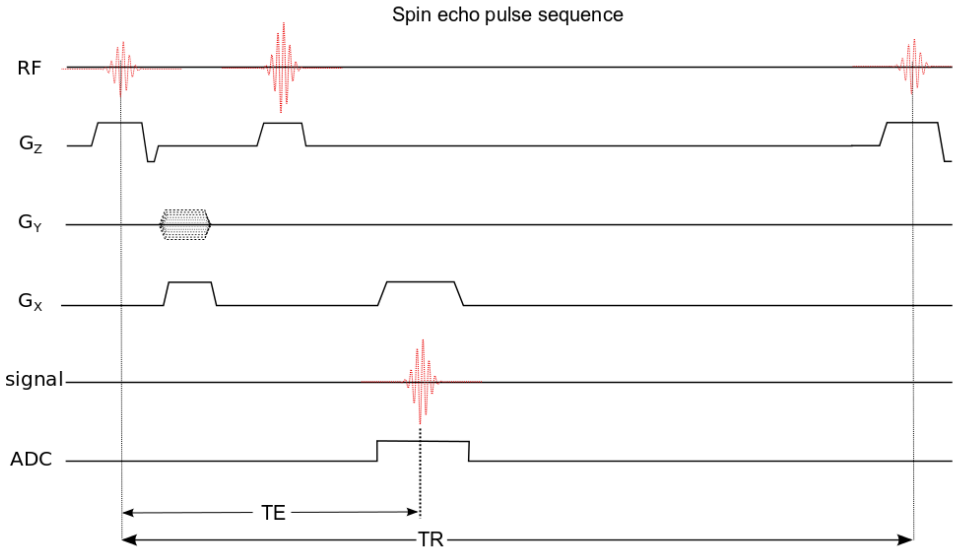

Figure 2.10: Scheme showing the spin echo sequence. Signal is only acquired where the analog to digital converter (ADC) is not zero.

2.2.2.3.2 Gradient Echo (GE) Sequence In GE sequences, an RF pulse is applied partially flipping the net magnetization vector into the transverse plane (flip angle). On opposite to SE sequences, gradients are used to dephase and rephase the transverse magnetization vector instead of the 180° RF pulse. A first gradient is applied to dephase and then a gradient with opposite sign is applied to rephase the spins. As gradients do not refocus field inhomogeneities, as the 180° RF pulse does, GE sequences with long TEs are T2* (time constant describing the exponential decay of signal, due to spin-spin interactions, magnetic field inhomogeneities, and susceptibility effects. weighted, rather than T2 (time constant describing the exponential decay of signal, due to spin-spin interactions only) weighted as SE sequences are.

A simple diagram of a conventional GE sequence is shown in Figure 2.11, [Prasad, 2006]. An RF pulse lower than 90° is applied along with a slice selective gradient. Gradients with opposed signs are used to rephase the signal. Finally, the signal (echo) is acquired at a time around TE. As there is no 180° RF pulse low flip angles can be applied, allowing shorter TR and therefore shorter acquisition scans than in SE sequences.

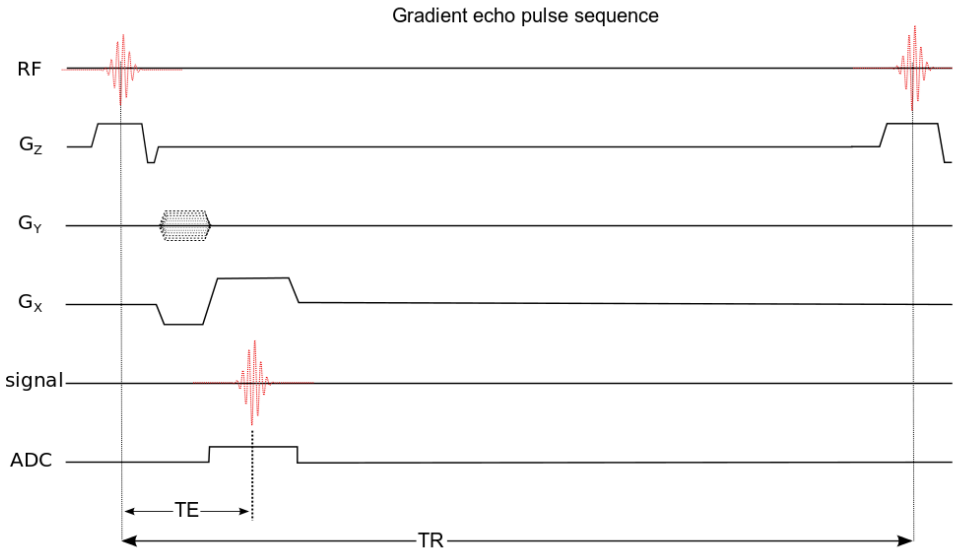

Figure 2.11: Scheme showing the gradient echo sequence. Signal is only acquired where the ADC is not zero.

2.2.2.3.3 Ultrashort Echo Time (UTE) Sequence Current sequence techniques image tissues using TEs between 10 and 200 ms, in both T1 (time constant describing the loss of signal, due to spin-lattice interactions) and T2 weighted images. However, some tissues present very short T2, Table 2.3, and therefore few or no signal is detected. This makes difficult to image these tissues.

Table 2.3: T2 relaxation times for some human tissues, [Holmesa and Bydderb, 2005].

Ligaments	4-10ms
Cortical bone	0.4-0.5ms
Dentine	0.15 ms
Knee menisci	5–8 ms
Achilles tendon	4–7 ms

Two major limitations to image short T2 can be stated. First, for tissues with short T2s, the relaxation of the transverse magnetization cannot be ignored in opposition to tissues with long T2. When a 90° RF pulse is applied to tissues with long T2 a complete flipping of the magnetization vector can be assumed because the duration of the RF pulse is much smaller than the relaxation time. On the contrary, for tissues with very short T2 the relaxation time must be accounted even when applying

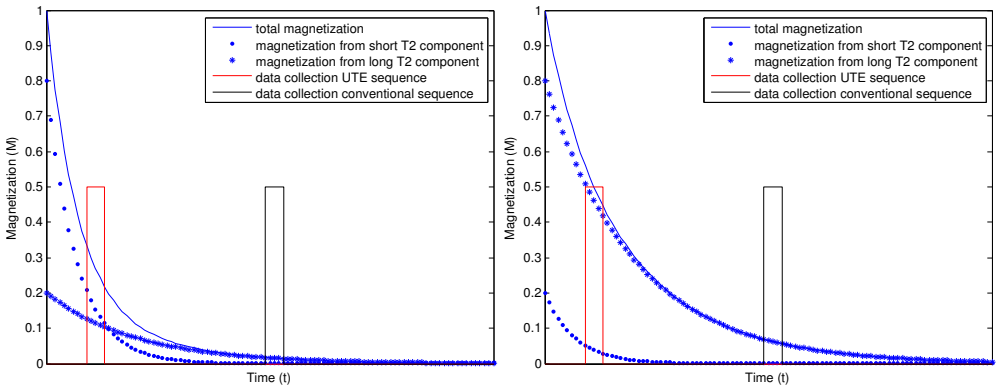

(a) High content of short T2 components.

(b) High content of long T2 components.

Figure 2.12: Transverse magnetization in respect of time for different tissue compositions of short and long T2 components. For tissues highly composed of short T2 components (a) the UTE sequence is able to collect signal from both short and long T2 components while conventional sequences do not acquire any signal. For tissues highly composed of long T2 components (b) the UTE sequence is able to collect signal from both short and long T2 components while conventional sequences can only obtain signal from long T2 components.

the RF pulse. Second, short T2 components present broader resonance peak when compared to long T2 components, therefore RF pulses slightly different from the Larmor frequency also excite these tissues, [Keereman, 2012].

The idea of UTE sequences is to image the tissues as quick as possible, before the signal from short T2 tissues fade away Figure 2.12. Three important factors are used to make this possible, namely: (1) short RF pulses, (2) radial sampling of k-space, (3) FID sampling.

1. The first factor is easily understandable, because when the RF pulse duration equals the T2 value the relaxation of the tissue cannot be ignored, so reducing the RF pulse as much as possible is essential.

2. In a normal Cartesian grid k-space sampling gradient pulses are needed for the initialization of each line. In contrast, in a radial k-space sampling the acquisition can be performed without applying any gradient. Moreover, radial sampling oversample the center of the k-space, increasing the signal-to-noise ratio (SNR) of low spatial frequencies in respect of high spatial frequencies.

3. As the tissues with short T2 start to decay rapidly, sequences that use gradients or 180° RF pulses before acquisition are not possible

due to time constrain. Instead, the acquisition of the FID signal can be performed immediately after the RF pulse.

%enditemize

After knowing the basic concepts for UTE imaging, the sequence procedure is simple, Figure 2.13.

In a 3D UTE sequence, [Rahmer et al., 2006], an RF pulse is first applied. This pulse must be as hard as possible (within safety values), and with a small flip angle ($< 10°$). This makes the RF pulse very short and allows imaging of tissues with extremely short T2.

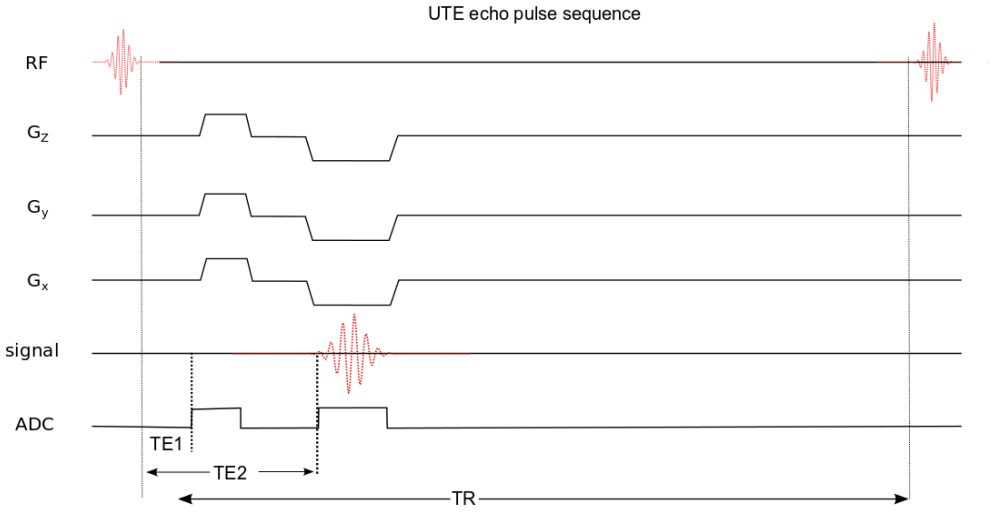

Figure 2.13: Scheme showing the UTE sequence.Signal is only acquired where the ADC is not zero.

After the RF pulse, a switch from transmission to reception is performed to allow acquisition (fast coils are therefore needed).

Acquisition of the FID signal starts with the application of the gradients. This is not usual in conventional sequences, where the acquisition is only performed when the gradients are in a stable strength value. With the use of the gradients, the k-space vector is acquired in a radial sampling from the center to outwards. Finally, to provide contrast between short and long T2 components, a gradient echo image is acquired using the UTE sequence. The gradient is inverted to acquire the k-space from one extreme to the other. This gradient must have the double of the area as before, meaning that strength and/or duration of the pulse must be increased.

2.2.2.4 Image degrading effects

As other imaging techniques MRI suffers from image degrading effects (or artefacts) that may affect the diagnostic quality. An artefact is something that appears in an image that is not present in the original object. Depending on their origin these can be classified as patient-dependent, signal processing dependent or hardware dependent. Due to the importance for the presented thesis motion and metal artefacts (Patient-related MR artefacts), as well as, B0, B1 and RF inhomogeneities (hardware-related artefacts) will be covered. More information about other types of MR artefacts and respective corrections can be found in [Erasmus et al., 2004, Pusey et al., 1986, Vadim Kuperman, 2000].

2.2.2.4.1 Metal artefacts Metal artefacts occur at interfaces of tissues with different magnetic susceptibilities, which cause local magnetic fields to distort the external magnetic field. The degree of distortion depends on the type of metal, type of interface, pulse sequence and imaging parameters, Figure 2.14. Reduction of these artefacts can be accomplished by using specific sequences, such as MARS (metal artefact reduction sequence) that use and additional gradient along the slice select gradient at the time the frequency encoding gradient is applied, [Olsen et al., 2000]. Although not a patient dependent MR artefact, metal artefacts due to metal components in the FOV of the MR are an important issue in hybrid techniques such as PET/MR.

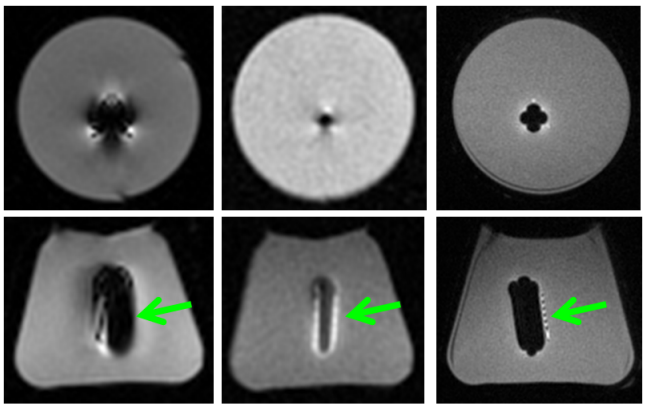

Figure 2.14: Imaging of a titanium screw in a 1% agarose Gel phantom using different sequences: 2D GE (1st column), 2D VAT SE (2nd column) and 3D UTE (3rd column) in the axial (1st row) and sagittal (2nd row) planes. Reduced artefacts can be seen with the 3D UTE sequence [Du et al., 2010].

2.2.2.4.2 Motion artefact Motion artefact is one of the most common artefacts in MR imaging, causing either ghost images or diffuse image noise in the phase-encoding direction Figure 2.15. The reason for mainly affecting data sampling in the phase-encoding direction is the significant difference in the time of acquisition in the frequency-encoding (miliseconds) and phase encoding (seconds) directions, [Erasmus et al., 2004]. Several methods can be used to reduce motion artefacts, such as patient immobilization, sedation, cardiac and respiratory gating [Costa et al., 2005, Pipe, 1999, Scott et al., 2010] or external monitoring for motion tracking [Gunther and Feinberg, 2004].

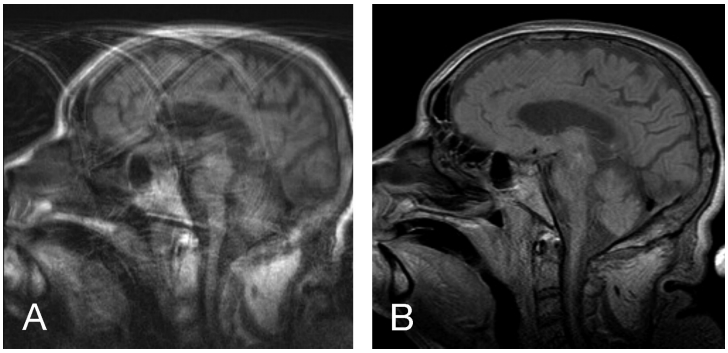

Figure 2.15: A) Sagittal T1 FSE image with considerable motion artefacts in patients undergoing mechanical ventilation. B) Same image as A) but with a navigator pulse to gate the patient's head motion, [Barnwell et al., 2007].

2.2.2.4.3 B0, B1 and RF inhomogeneities B0, B1 and RF inhomogeneities artefacts can derive either from spatial and/or intensity distortions, Figure 2.16. Three major components may induce such type of artefacts: (1) the external magnetic field (B0), (2) the gradient field (B1) or (3) the RF coils.

- Intensity distortions. Intensity distortions occur when the field in a certain position is different (with higher or lower magnitude) that in the rest of the image.

- Regarding gradient field inhomogeneties, they occur when from the centre of the applied gradient increases, yielding loss of field strength at the periphery. When the phase-encoding gradient is different from the frequency-encoding gradient, the width or the height of the voxel are different and a distortion results, [Pusey et al., 1986]. This can be avoided if square pixels (regarding the 2

spatial directions on the considered plane) or cubic voxels (regarding the 3 directions in the considered volume) are acquired. Furthermore, to reduce inhomogeneities due to gradient fields, phase-encoding should be assigned to the lowest dimension (and therefore the frequency to the largest one).

- Finally, inhomogeneous artefacts due to problems in RF coils may influence the intensity across the image. This type of artefact may arise due to failure in the RF coil, non-uniform B1 field or non-uniform sensitivity of the receiver coil, [Pusey et al., 1986].

The use of prospective methods for inhomogeneity correction is not easily reliable. Some retrospective methods have been developed to try to reduce intensity inhomogeneities such as by low pass filtering the image [Tomazevic et al., 2002], surface fitting [Styner et al., 2000], statistical modeling [Wells et al., 1996] or use multispectral images [Vovk et al., 2006].

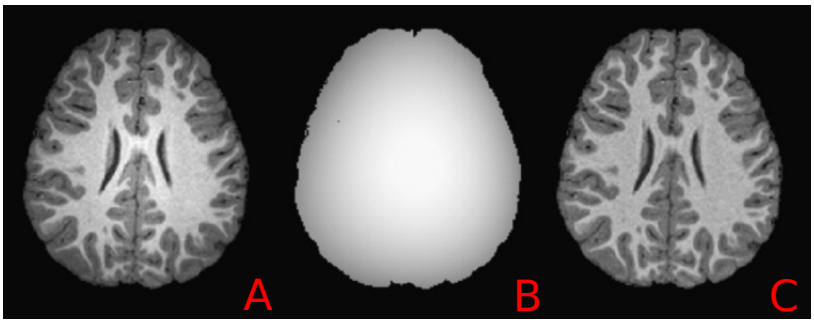

Figure 2.16: A- Brain MR image presenting high intensity inhomogeneities; B- Estimated bias field; C- Corrected MR image for intensity inhomogeneities,[Ji et al., 2011].

2.2.3 MRI hardware

While modern MR instruments vary considerably in design and specifications, all MR scanners include several essential components.

First, a main polarized magnetic field is required. This magnetic field is generally constant in time and space and can be implemented using different types of magnets. The purpose of this magnet is to induce a net nuclear spin magnetization to the volume of interest.

Second, secondary magnets with specific time and spatial dependencies are required. These magnets, usually called gradient field magnets, are needed to induce spatial changes in the polarized magnetic field.

These spatial changes allow manipulating the net nuclear spin magnetization, so that it is dependent on the spatial localization in the volume.

Finally, radio-frequency (RF) coils, both transmitter and receiver coils, are required to first transmit RF waves to the volume and second to detect the resulting NMR signal. The transmitter coil allows creating the B1 field necessary to excite the nuclear spins and the receiver coil to detect the weak signal emitted by the spins as they precess in the B0 field.

2.2.3.1 Magnet

The function of an MR scanner main magnet is to generate a strong, stable and spatial uniform magnetic field for the volume of interest. This leads to four major specifications of the magnet: field strength, stability, spatial homogeneity and dimensions of the magnet. Different types of magnets have been proposed to maximize some of the specifications and are divided into permanent, resistive, and superconducting magnets.

Due to the ability of superconducting electromagnets to achieve high and stable magnetic fields and negligible power consumption this type of magnets has been largely preferred over other types for clinical use. However, the critical temperature for a certain material to become superconductive is very low and cooling systems based in liquid helium are required.

2.2.3.2 Gradient Coils

Gradient coils have the main function to generate a linear, stable and reproducible B0 field gradient along specific directions within short times. Nonetheless, gradient coils can be used also for flow compensation, spoiling or pre-saturation. The need for rapid switching of gradients makes the construction of such devices complicated. Four parameters must be accounted when developing a gradient coil: the gradient strength, linearity, stability and switch time.

2.2.3.2.1 Gradient orientation For position encoding 3 pairs of gradient coils are used. These gradient coils should be able to generate linear magnetic fields in X, Y and Z directions. The orientation of each gradient coil is easily explained by Figure 2.17. Induced currents with different directions are used to generate the desired magnetic field gradient. For Z-gradient coils Maxwell Pair coils are used.

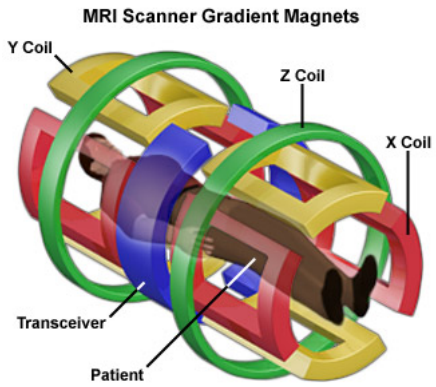

Figure 2.17: Illustration showing the position and orientation of the MR gradient coils. Obtained from: www.ovaltech.ca/philyexp.html.

2.2.3.3 RF Coils

RF coils are used for both transmission and reception of signals in MRI. In all clinical MRI systems a large integrated RF body coil is present. It is mostly used for excitation of the spins. The signal reception quality is strongly dependent on the distance between the spins and the coil, using the body coil. The coil should be as close as possible to the object for optimization. Therefore, different RF coils are used in MRI. Specific coils exist for the brain, head and neck, chest, spine, knee, etc. The closer they are to the body, the better is the signal quality. Some of these coils also have the possibility to transmit RF waves. Currently, most coils used in clinical practice are multi-channel coils, which speed up the acquisition process.

2.3 Positron Emission Tomography

2.3.1 Traces physical principles

PET is an imaging technique, being actually the golden technique (standard technique) in oncology applications in medicine as diagnostic, staging and therapy monitoring [Townsend, 2004].

The principles of functional imagiology in vivo with PET relate to the selection and production of a radiotracer (radioisotope), specifically, a pharmaceutical marked with a positron emission nuclide, administration of the radioisotope in the patient and monitoring its distribution in the patient.

According to the current atomic model the stability of the nucleus is dependent of the neutron-proton ratio. Theoretically nuclei that do

not lie in the stability region tend to decay in a way that approximate the nucleus to the stability region. Three types of decay may occur: α decay, β decay or γ decay. For PET only the β decay is of interest. In β decay three different decay types may occur: β- , β+ and electron capture (K-capture) [Jadvar and Parker, 2005].

In the case of β- decay the nucleus is unstable due to a high neutron-proton ratio and needs to transform a neutron into a proton to approximate the stability region. For this to happen, an electron is emitted along with an electron antineutrino (Equation 2.13).

$$\mathrm{n} \rightarrow \mathrm{p}^{+} + \beta^{-} + \bar{\nu}_{\mathrm{e}} \tag{2.13}$$

In the case of β+ decay the nucleus is unstable due to a low neutron-proton ratio and needs to convert a proton into a neutron to approximate the stability region. The nuclear transmutation of the proton into a neutron involves the emission of a positron and an electron neutrino, Equation 2.14. The energy released from the reaction is passed to the positron and the neutrino as kinetic energy.

$$\mathrm{p}^{+} \rightarrow \mathrm{n} + \beta^{+} + \nu \tag{2.14}$$

In the cases where the nucleus has a low neutron-proton ratio the electron capture is also possible. Moreover, when the energy of the daughter atom is lower than that of the parent atom by at least 1.022 MeV the β+ decay is not possible and the only decay that may occur is given by Equation 2.15.

$$\mathrm{p}^{+} + \mathrm{e}^{-} \rightarrow \mathrm{n} + \nu_{e} \tag{2.15}$$

As the β- decay and the electron capture processes do not release positron in the reaction, they are not significant to PET technique. For this reason only the β+ decay is further explained.

During the β+ decay the energy of the positron emitted depends on the isotope, being the energies varying from 0.6 MeV for 18F to 3.4 MeV for 82Rb [Townsend, 2004]. After the release, the positron loses its kinetic energy in the surrounding tissues and annihilates with a proximal electron originating two gamma photons of 511 keV, corresponding to the transformation of the positron and electron mass into energy in accordance to the conservation of mass-energy. The two photons are also emitted approximately into opposite directions (roughly collinear) in accordance to the conservation of linear moment, due to nearly full absence of kinetic energy. These both characteristics are the fundamental point for the identification of coincidence events in the PET modality.

However, the emitted positron loses kinetic energy by travelling and therefore it does not annihilate at the position where the positron was emitted but elsewhere (Figure 2.18). The range of the positron is dependent on the emission energy and can be determined empirically [Ziegler, 2005]. Also, as the positron-electron system can contain residuals of moment, a perfect collinearity of the two photons may not happen (+/- 5°). Inevitably this leads to a decrease of the spatial resolution of the PET system [Shibuya et al., 2007]. The contribution of the non-collinearity of the photons increases with the increase of detectors distance, i.e. with the detector ring diameter of the scanner and it is maximum in the centre of the transverse field of view (FOV) (Figure 2.18) [Townsend, 2004].

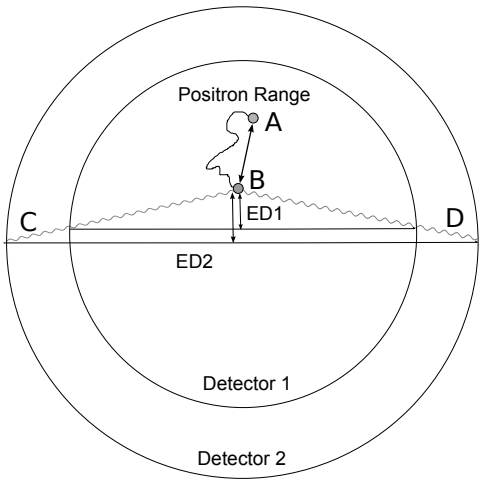

Figure 2.18: The intrinsic resolution of PET. After the emission of the positron by the radionuclide (A), the positron travels until it loses almost all of its kinetic energy (B). After annihilation, as the system positron-electron may contain remaining momentum the photons emitted are not completely collinear (C and D). Note that the true annihilation position and the estimated annihilation position associated to detector ring 2 are farther than those associated to detector ring 1, i.e, the error for detector ring 2 (ED2) is higher than for detector ring 1 (ED1).

Once a photon pair from an annihilation process is detected by the PET detectors timed pulses are produced in these detectors. A coincidence processing unit is used to filter events that are received within a time window (e.g. 12 ns in [Judenhofer et al., 2007]) from other events, and assigning the former as a true coincident event and the rest as false events. The true coincidence events are assigned to a line of response (LOR), the ideal line connecting both affected detectors that contain information about the annihilation position. The LOR's are used by reconstruction algorithms to obtain a PET image [Rong, 2009].

2.3.2 Imaging principles

2.3.2.1 Image degrading effects

As other types of imagiology PET suffers from different image degrading effects. The most important and therefore covered here are: noise, normalization, dead time, partial volume, photon attenuation, scatter and randoms as well as motion artefacts.

2.3.2.1.1 Noise One of the main problems in PET images is noise. Noise is nothing more than random variation of the count rate due to statistical fluctuations. In PET, noise can be modeled as a Poison distribution and can be reduced with $1/\sqrt{(N)}$ by increasing the number (N) of detected scintillation photons. To reduce noise the measurement time or the activity given to the patient should be increased. However, both of these approaches have their disadvantages: an increased scan time is not always desirable or practicable; an increased injected activity raises the radiation dose of the patient. Techniques that post-process the acquired images to increase the signal to noise ratio have long been applied (e.g. [Hofheinz et al., 2011]). Yet with the development of new hybrid techniques (PET/MR) the focus on new methods, [Caldeira et al., 2011] has been carried out.

2.3.2.1.2 Dead Time In PET systems the processing of a certain event by a detector takes a significant time, during which no other events can be processed. Therefore, if the detector receives two photons within this period of time the second photon will be neglected. This time interval is called dead time. Dead time is high at higher count rates, when more photons arrive per unit of time and consequently more photons will be neglected. In the same sense at lower count rates the dead time is negligible and the measured activity is linearly correlated to the actual activity in FOV.

The conditions mentioned above make it possible to correct for dead time by measuring the activity for several half-lives starting with high activity concentrations. The low counts rates are then linearly interpolated up to the higher count rates yielding dead time correction factors. Other types of corrections are possible and were studied extensively in [German and Hoffman, 1990, Tanaka et al., 2002].

2.3.2.1.3 Normalization In current PET systems a high number of scintillation crystals are used for the detection of the gamma rays emitted in the process of annihilation of a positron with an electron. Ideally, these scintillation crystals should have the same sensibility. However, in a real

system this is not achievable and a normalization map must be used for correction.

The concept of normalization is simple. In an ideal system if there is a homogeneous activity concentration in the FOV of the scanner, all the scintillation crystals should measure the same counts. In a real system the variation in the number of counts for each crystal can be used to derive a normalization factor map.

Specifically in the BrainPET (system that was used for the development of this work) a normalization scan is performed by placing a homogeneous plane source in the FOV of the PET scanner. This plane source is rotated a certain number of times, during a certain period of time. Depending on the orientation of the plane source in respect to time, only the LORs that are perpendicular to the plane source are used for reconstruction and generation of the normalization factors. By calculating the ratio between the measured and the expected number of counts the normalization factors for each LOR can be calculated, [Lohmann, 2012].

2.3.2.1.4 Partial Volume Effect In quantitative PET the reconstructed image must map the radiotracer concentration in a uniform and precise way within the FOV. However, due to the partial volume effect (PVE), the image values are biased, dependent on the scanner resolution as well as on the structure size and the radiotracer concentration of that structure relatively to the surrounding structures. The PVE smooth PET images so that some of the radioactivity from regions of higher concentration is mis-attributed to adjacent regions of lower activity.

Two distinct phenomena causing PVE can be distinguished: 3D image blurring introduced by the finite spatial resolution of the imaging system, and data sampling, as the contours of the voxels do not match the actual contours of the tracer distribution, thus including different types of tissues [Soret et al., 2007].

Different methods have been developed to try to correct the PVE such as [Meltzer et al., 1990, Müller-Görtner et al., 1992, Rousset et al., 1998]. In these methods techniques based on anatomical information as MR images are included [Kusano and Caldwell, 2005]. Further information regarding PVE correction are reported in [da Silva, 2012, Rousset et al., 2007].

2.3.2.1.5 Scatter and Randoms In PET as well as in other medical imaging modalities some events are majorly related to the background noise.

In the case of scattered events (Figure 2.19 B), one or both photons can suffer scattering, being the Compton scattering the most relevant

interaction at 511 keV. If detected in coincidence, a wrong line joint is attributed to the detectors in consideration. These events could be corrected by a simple energy threshold, in which only the photons that do not lose energy were accept. Although, the lack of energy resolution of PET detectors limit the use of this type of correction, as it is not possible to distinguish between scattered and non-scattered photons at energies as low as 350 keV [Townsend, 2004]. Therefore, scatter correction algorithms have been developed to reduce the generated background.

The random events (Figure 2.19 C), are originated from different annihilations that reach opposed detectors in the given temporal window. The random coincidence as well as the single photon rate interacting with the detectors increases with the increasing temporal window. The single photons that interact with the detectors may come from annihilations in the FOV of the detector, but also from annihilations in which at least one photon enter the FOV of the detector.

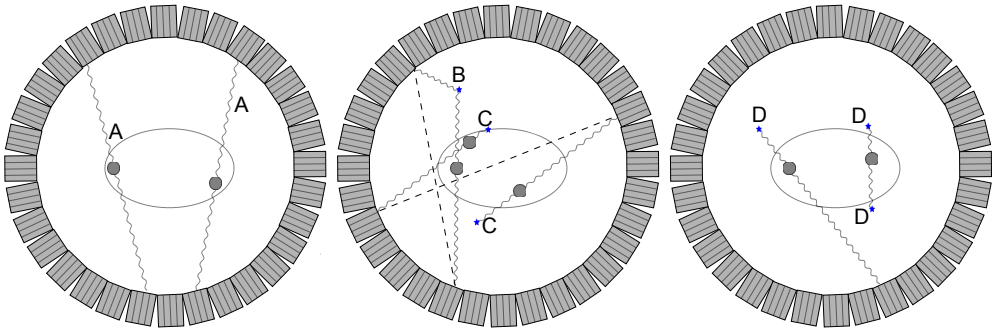

Figure 2.19: The processes that may occur during a PET scan: A) True event; B) Scatter event; C) Random event; D) Attenuated photons (no event detected).

2.3.2.1.6 Attenuation effect Not every photons that are scattered are identified and contribute to incorrect LOR's, Figure 2.19 D. They can be completely absorbed by the tissues or exit the FOV of the detector ring. Attenuation corresponds to the removal of photons and consequently it will contribute to the removal of LORs. The attenuation of photons follows an exponential decay determined by the linear attenuation coefficient μ of the tissue and the energy involved. For a given energy, in our case 511 keV, the attenuated intensity I is diminished from the original (not attenuated) intensity Io by the exponential factor $e(-\mu \times L)$, where L is the considered distance.

A true coincidence requires that both photons, originated from the same annihilation of a positron with an electron, must be detected in a

simultaneous way. If one of these photons is absorbed or scattered along its path, no coincidence line is recognized. So, the probability of detection of a coincidence is dependent on the combined path of the two photons. As both photons have the same energy, the linear attenuation that they are subjected is the same. As both photons have the same energy, the linear attenuation that they are subjected is the same. Furthermore, from Equation 2.16, the probability of both photons to be detected is the product of the single probabilities, and it can be shown that the attenuation probability is also independent from the source position and the problem of attenuation correction of photons is the determination of the attenuation probability for each LOR, Figure 2.20.

$$I = \left(I_0 \mathrm{e}^{-\mu(x,y)\times A1}\right) \times \left(I_0 \mathrm{e}^{-\mu(x,y)\times(At-A1)}\right) = I_0 \mathrm{e}^{-\mu(x,y)\times At} \tag{2.16}$$

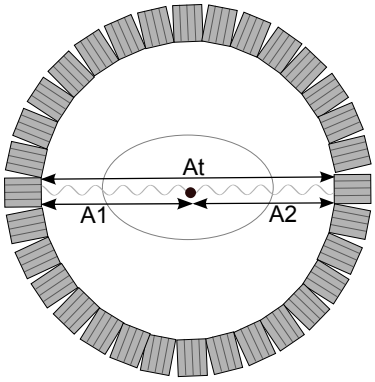

Figure 2.20: Illustration showing the path taken by two annihilation photons. A1 is the distance from the annihilation position to the detector at left; A2 is the distance from the annihilation position to detector at right; At is the total distance, i.e., At=A1+A2.

Different methods for attenuation correction have been developed, being divided in methods with and without a transmission scan, [Townsend, 2003, Zaidi and Hasegawa, 2003]. During a transmission scan rotatory external devices are used containing positron sources (Figure 2.21 A), typically 68Ge-68Ga (two annihilation photons at 511 keV), or gamma-ray sources (Figure 2.21 B), typically 137Cs (one gamma-ray photon at 662 keV), or the use of CT data (Figure 2.21 C) (with energies of 70-80keV X-ray photons in clinical routine) [Kinahan et al., 2003]. In case of absence of transmission devices attenuation maps can be derived from MR data (typically divided into segmented or template-based) [Hofmann et al., 2008, Keereman et al., 2010, Schreibmann et al., 2010] or can even numerically calculated [Bergström et al., 1982].

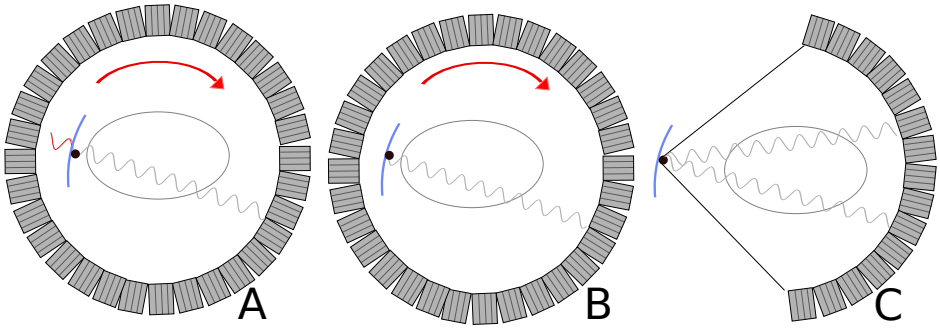

Figure 2.21: Transmission scans employed currently. Transmission scan with positron source rotating around the patient. B) Transmission scan with gamma-ray source rotating around the patient. C) CT scan as transmission scan.

2.3.2.2 Image reconstruction

The goal of image reconstruction is to recover the radiotracer concentration from the measurements. Different methods have been proposed for PET image reconstruction and can be majorly subdivided into two large groups: analytical and iterative methods.

2.3.2.2.1 Deterministic and Stochastic Imaging Models The goal of reconstruction is to use a set of observations (projections) and find the unknown image. One way to represent the imaging system is as follows:

$$p = Hf + n \tag{2.17}$$

where p are the observations, H the system model, f the unknown image, and n the error in the observations. Two approaches proposed to solve this imaging system, were either by assuming that the data is deterministic, containing no statistical noise, and thus n is deterministic; or by assuming that the data are intrinsically stochastic, and thus n represents random noise.

The first approach assumes that n is deterministic and if known the exact solution for the image can be obtained. Analytical reconstruction methods assume deterministic models and use the inverse Radon transform to obtain a mathematical solution to the system model. The deterministic approach has the advantage of simplifying the reconstruction process, making it fairly fast and easy. However, this approach oversimplifies, neglecting the noise presented in the system, leading to reconstruction artefacts.

The second approach assumes that the data is stochastic and derive from diverse physical factors such as, positron decay process, effects of attenuation, scatter and randoms. Iterative reconstruction methods assume stochastic models, and converge to closer solutions at each iteration for a set of constraints. This approach has the advantage of higher accuracy, by not neglecting the influence of noise, although is much more computational demanding than analytical methods.

2.3.2.2.2 Analytical image reconstruction One of the foundation of analytical image reconstruction methods is the central-section theorem. This theorem states that the Fourier transform of a one-dimensional projection is equivalent to a section, or profile at the same angle through the centre of the two-dimensional Fourier transform of the object, [Kak and Slaney, 1988].

Backprojection is one important step in analytical image reconstruction as it is the transformation of the projections into image arrays along the appropriate LOR. It could be though that transforming all the projections to the image space would yield the correct image. However, due to oversampling of the centre of the Fourier transform, the contribution from the centre is higher than that from the edges. In the image space this would be seen as blurring, Figure 2.22.

To correct the problem of oversampling in the backprojection, the data need to be weighted (filtered) in order to have equal contribution. This is accomplished by filtering each projection with a ramp filter. Nonetheless, the inverse problem is ill-posed, meaning that a small perturbation of the data can lead to unpredictable changes in the solution. To regularize this, a simple smoothing is normally performed. The smoothing function used is not defined and should be chosen dependent of the task to be performed.

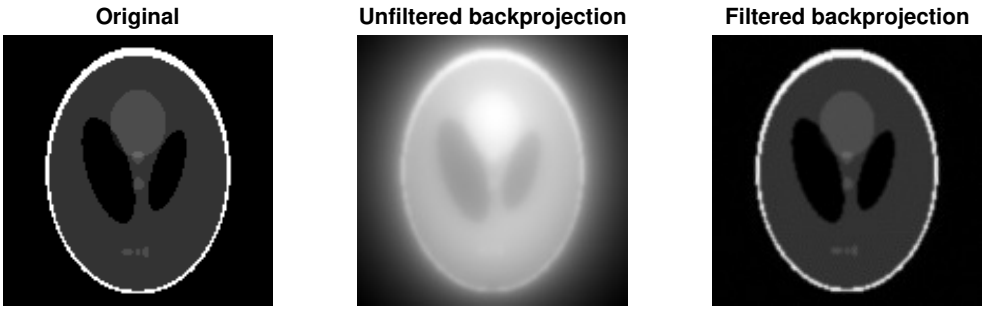

Figure 2.22: Illustration showing an original image with the reconstructed images with an unfiltered backprojection (center) and with a filtered backprojection (right).

2.3.2.2.3 Iterative Image reconstruction Iterative methods, as it was referred before account for the noise present in the observation data. However, these methods are more complex and computational expensive when compared with analytical models.

The iterative algorithm, Figure 2.23, starts with an initial estimated image (can be as simple as a uniform image) and the data acquired from the PET scanner. The estimated projection data are compared with the measured projection data and the error in the projection space is calculated. This error is backprojected to the image space, yielding error maps that are used to update the image estimative. This process is iteratively repeated and improves the image estimative at each iteration. The process stops at pre-defined number of iterations.

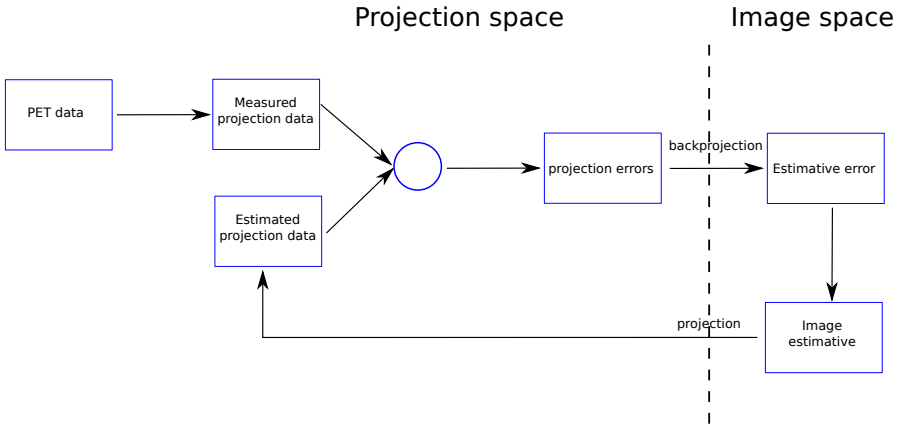

Figure 2.23: Scheme of the iterative reconstruction method.

To solve the above iterative method two major tasks must be accomplished: comparison of measured projection data with estimated projection data and update of the image estimative.

Different methods have been proposed to solve these tasks such as the Maximum Likelihood Expectation Maximization (MLEM), the Ordered Subsets Expectation Maximization (OSEM) and the Bayesian/Penalized Method. As OSEM was used for the reconstruction process used in this project the Bayesian/Penalized Method will not be further explained. However due to the similarity between MLEM and OSEM both will be explained.

Maximum Likelihood Expectation Maximization (MLEM)

The MLEM algorithm consists of two processes. First, it defines a cost/criterion function. The cost function in the MLEM is the maximum-likelihood (ML) criterion. In this approach, the probability relationship is a likelihood function of the object f. Second, the MLEM algorithm tries to find the image estimation that maximizes the likelihood of the object

by Expectation Maximization (EM). Applied to the PET reconstruction problem the MLEM is represented with a simple iterative Equation 2.18.

$$f_j^{n+1} = \frac{f_j^n}{\sum_i H_{i,j}} \sum_i H_{i,j} \frac{p_i}{\sum_k H_{i,k} f_k^n} \tag{2.18}$$

where, f_j^{n+1} is the next estimate of voxel j based on the current estimate f_j^n, H is the system matrix and p_i the i-th measured projection data. p_i can be calculated by the measured data by Equation 2.19.

$$p_i = \sum_j H_{i,j} f_j \tag{2.19}$$

Equation 2.18 and Figure 2.23 relate in the following way. First the PET data is forward projected to yield the measured projection data p_i. Second the measured projection data p_i and the estimated projection data $\sum_k H_{i,k} f_k^n$ are compared by the ratio of one by the other. This gives a multiplicative projecton error for each projection (in projection space). This error is backprojected to the image domain, thus giving an estimative error (in image space). The estimative error is then multiplied by the current image estimate f_j^n and divided by a weighting term based on the system model $\sum_i H_{i,j}$. The new estimation is forward projected yielding new estimated projection data and the algorithm repeats these steps until a certain amount of iterations is reached.

Ordered Subsets Expectation Maximization (OSEM)

OSEM algorithm works similarly to the MLEM algorithm being the major differ- ence the work with subsets instead of with the entire data, Equation 2.20

$$f_j^{n+1} = \frac{f_j^n}{\sum_{i \in Sn} H_{i,j}} \sum_{i \in Sn} H_{i,j} \frac{p_i}{\sum_k H_{i,k} f_k^n} \tag{2.20}$$

where the backprojection steps sum only over the projections in subset Sn of a total of N subsets. If the number of subsets equals 1 the OSEM method falls into the MLEM method. The major advantages of this method over the MLEM method is that the reconstruction time is reduced.

2.3.2.2.4 Compensation for image degradation effects Until now only the basic reconstruction process was introduced, and the compensation for image degrading effects such as attenuation, scatter, randoms or normalization were not yet contemplated.

Once the values for correcting degradation factors have been estimated either analytical or iterative methods can be used for compensation and reconstruction, yet in a different manner. On analytical methods

the prompts are corrected prior to the reconstruction step. This means that the corrections are applied in the projection space with following filtered backprojection to yield a corrected image.

On iterative methods it is recommended to reconstruct directly the prompts data introducing the corrections within the reconstruction algorithm. This is important as MLEM methods assume Poisson distribution and this only holds when no correction was performed to the data.

For the MLEM algorithm Equation 2.18 can be therefore modified to account for degrading effects such as attenuation, normalization, scatter and randoms, Equation 2.21.

$$f_j^{n+1} = \frac{f_j^n}{\sum_i n_i a_i H_{i,j}} \sum_i n_i a_i H_{i,j} \frac{d_i}{\sum_k n_i a_i H_{i,k} f_k^n + s_i + r_i} \tag{2.21}$$

where a_i is the attenuation correction, n_i is the normalization correction, s_i is the scatter correction, r_i is the random correction and d_i the measure projection data corrected for attenuation, normalization scatter and randoms, given by, Equation 2.22.

$$d_i = \sum_j n_i a_i H_{i,j} f_j + s_i + r_i \tag{2.22}$$

2.3.3 PET hardware

Detection systems are a key component to any imaging system, and an understanding of their proprieties is important to establish appropriate operating criteria or designing schemes for obtaining quantitative information.

Scintillation detectors are the most used radiation detectors in PET imaging. A scintillator detector primarily consists of a scintillator that produces scintillation light after interaction with radiation, and a photodetector that converts the scintillation light into electrical signal.

Normally, a PET detector system utilizes a multiple-block-detector arrangement. These detector blocks are finally arranged in a ring structure.

2.3.3.1 Scintillators

Scintillators are used to detect gamma photons, producing scintillation photons with wavelengths ranging from visible to ultraviolet. To detect 511 keV gamma photons only photoelectric absorption and Compton scattering are relevant interaction mechanisms, [Saha, 2005a]. Moreover, photoelectric absorption is preferred to Compton scattering, as the first

release an electron with the entire energy of the photon, while the second transfers a part of the energy to the electron and the rest to a scattered photon. Therefore, scintillators should maximize interactions by photoelectric absorption, while minimizing by Compton scattering.

As the photoelectric cross section depends on the density and effective atomic number of the crystal, and the Compton cross section depends only from the density of the crystal, [Podgorsak, 2006], a scintillator should have a high density for a high absorption probability and a high atomic number for a large fraction of events undergoing photoelectric absorption. Two parameters are normally defined using the statements above: the photofraction and the attenuation length, [Lecomte, 2009]. The photofraction is defined as the probability that a gamma photon will interact by photoelectric effect instead of Compton scattering, and thus it should be maximized. The attenuation length is defined as the distance into a material where the probability has dropped to 1/e that a particle has not been absorbed, and thus it should be minimized.

A scintillator should also have a high light yield and low decay time. The latter is important, as a fast decay time leads to short coincidence windows that will limit the amount of random coincidences. Some of the proposed scintillators for PET are described in Table 2.4.

Table 2.4: Scintillators used in PET detectors (adapted from [Lecomte, 2009]).

Crystal Type	NaI	BGO	GSO	LSO
Density (g/cm^3)	3.67	7.13	6.71	7.35
Effective Z	50	73	58	65
$1/\mu$ (mm)	25.9	11.2	15.0	12.3
PE (%)	18	44	26	34
Light yield	41	9	8	30
Decay time (ns)	230	300/60	60/600	40
Magnetic susceptibility	No	No	Yes	No

2.3.3.2 Photodetectors

The output of the scintillator is a weak light signal and therefore need to be amplified. A photodetector is therefore used to convert the weak light output of the scintillator into a detectable electrical signal. Photomultiplier tubes and solid-state photodetectors have been developed for detecting low light levels. Both work by transferring the photon energy

to an electron by a collision. Some of the proposed photodetectors for PET are described in Table 2.5.

Table 2.5: Photodetectors used in PET (adapted from [Lecomte, 2009]).

Characteristics	PMT	ADP	SiPM
Active area	1-2.000 cm^2	1-100 mm^2	1-10 mm^2
Gain	10^5-10^7	10^2	10^5-10^6
QE at 420 nm (%)	25 %	60-80 %	<40 %
Magnetic susceptibility	Yes	No	No

2.3.3.2.1 Photomultiplier tubes (PMT's) Photomultiplier tubes (PMTs) have had a huge use in PET due to the combination of high gain, stability and low noise. PMTs consist mainly in a light transmitting window, a photocathode, a series of electrodes (dynodes) and an anode, inside a glass envelope, in vacuum. Photons pass the light transmitting window and interact with the photocathode by photoelectric interaction generating photoelectrons. The photoelectrons are accelerated to the first dynode where they interacts releasing low energy electrons. The generated electrons are accelerated from dynode to dynode, where in each dynode more electrons are generated, therefore creating a cascade of electrons. This cascade of electrons is collected by the anode, and a measurable current is produced.

2.3.3.2.2 Solid-state photodetectors Solid-state photodetectors have experienced an increase use in PET due to their advantages over PMTs such as low-cost and their insensitivity to magnetic fields which allows PET/MRI integrated systems.

One well known solid-state photodetector is the avalanche photodiode (APD). APD's consist of a thin layer of P+, a wide drift region (π), and an avalanche region (p and n+). Light passes the P+ layer and interacts in the π region creating electron-hole pairs. An electric field (low at the P+ and π layers and high at the avalanche region) accelerates the electrons through the avalanche region, ionizing Si atoms and creating secondary electrons. These electrons are thus accelerated and contribute to the generation of more electron [Hamamatsu, 2004].

More recently silicon photomultipliers (SiPMs) have been suggested as solid-state photodetectors. SiPMs consist of matrix of small APD cells. The APD cells are connect in parallel and thus contribute to a very high field in the avalanche region. More secondary electrons are

generated in the avalanche region than in APDs, due to the high field generated, thus very high gains are obtained.

2.4 PET/MR

The combination of different image modalities is not new. Different combinations, such as the combination of anatomical imaging through MR or CT and functional imaging through PET or SPECT have been proposed in the last decades. The first approaches to hybrid techniques started with the acquisition of the different modalities in different scanners with following coregistration of one image modality to the other. Later, approaches that combined different techniques in the same scanner were also evidenced. However, these techniques still posed the problem of not being truly simultaneous. The images are acquired in the two scanners in a sequential way. Recently, truly simultaneous hybrid techniques have been proposed, in which the different techniques are acquired at the same time through a fully integrated system.

2.4.1 Advantages of hybrid techniques

Different hybrid techniques have been proposed. The combination of PET/CT and PET/MR are of interest to the presented study, therefore these two techniques will be highlighted here.

Since the introduction of PET/CT with a sequential imaging on the same patient bed, a revolution in medical diagnosis of tumors, staging, detection of local and distant recurrence and assessment of therapy response has taken place. Nowadays, all sold PET systems are combined as a PET/CT system. The major applications of such systems are in the areas of oncology, cardiology and neurology. Some advantages of PET/CT over PET and CT separately can be enumerated:

1. Differentiation of physiological and pathological uptake in PET;
2. Planning radiotherapy;
3. Shorter times in attenuation correction of PET due to the use of CT data;
4. Improvement lesions location due to an almost perfect coregistration of anatomical and functional images;
5. PET/CT shows higher sensitivity and specificity than each of its components individually.

The advantages of MRI over CT and the development of MRI compatible PET inserts have turned the attention to the combination of these two techniques. Although the successful implementation of clinical hybrid PET/CT scanners took place before hybrid PET/MR scanner came outs, the idea of combining MRI with PET is not new. Some advantages of PET/MRI over PET/CT and over MRI and PET separately can also be enumerated:

1. MRI provides much higher contrast of soft tissues that CT does;

2. MRI does not lead to additional radiation dose as CT does;

3. MRI provides other types of imaging than only anatomical imaging, such as MR angiography or functional MRI which can be correlated simultaneously with functional PET;

4. MRI/PET allows simultaneous imaging which reduces the scanning time compared to the time necessary for both techniques separately.

2.4.2 Design difficulties

The possibilities in designing PET/MR scanners can be divided into 3 major points. First, the acquisition of both imagining techniques can be done in different scanners, but on the same bed. Second, the acquisition of both imaging techniques can be performed by the same scanner, in a sequential acquisition, similar to PET/CT scanners. Third, the acquisition of both imaging techniques can be performed by the same scanner as simultaneous acquisition in a fully integrated system.

Many difficulties regarding the combination of these techniques can be pointed out, especially when a fully integrated system is the approach chosen. These difficulties can arise from the interference of the PET components in the MR system or vice-versa from the MR interference in the PET system.

In respect to the interferences of the PET components in the MR system, the major problem is the generation of field intensity inhomogeneities due to metallic components of the PET system. These artefacts can make the interpretation of MR images impossible.

On the other hand, the interference of the MR system in the PET system can be subdivided into two different problems: the high static field and the MR gradients. The first one interferes mainly with the photodetectors such as the PMTs, which are very sensitive to magnetic fields. Thus, other approaches must be found. This will be covered in the next subsection. The second problem is the interference of the MR

gradients with the electronic of PET due to current induction, thus the electronic must be shielded.

2.4.3 Developed systems

Different systems have been proposed to reduce the interference from both the MR into PET system and vice-versa. The first systems were developed for small animal imaging, Figure 2.24, and their successfulness lead to the development of systems for human imaging.

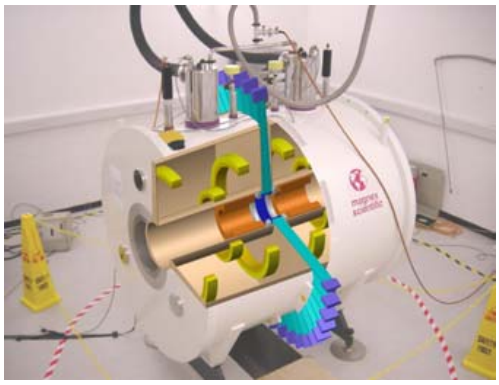

Figure 2.24: Combined PET-MR scanner for pre-clinical research. Obtained from: http://www.neuroscience.cam.ac.uk/directory/profile.php?rea1.

The first system tried to reduce the interferences by taking all the PET electronics away from the centre of the MR scanner. Optical fibres were also coupled to LSO crystals, guiding the scintillation light out of the influence of MR system. This system has the disadvantage of reduction of light output, due to attenuation by the optical fibres.

A further system was developed in which the MR scanner and the PET detector ring were integrated, but worked at different times. When the MR system was acquiring the PET system was paused and vice-versa. This eliminated the problem induced by the MR gradients in the PET system. However, the acquisition time of the exam was increased as the system did not work in a simultaneous way.

New developments in photodetectors lead to use different solid-state photodetectors (no magnetic susceptibility) rather than PMTs (high magnetic susceptibility). This new approach showed interesting results, in which the system was able to work in a fully integrated simultaneous imaging. The most studied solid-state photodetectors for combined PET/MR are the APD-based systems, as e.g. the SiPMT photodetectors which are very recent and still in development. The APD systems

can be located inside the MR bore directly coupled to the scintillation crystals. The amplified signal is conduced outside of the influence of the MR system for posterior processing by PET electronics.

As referred at the beginning of this subsection these first photodetector systems lead to the development of clinical systems to be used with human subjects. The first clinical system was proposed by Philips, Figure 2.25. This system works similar to PET/CT systems (sequential imaging). The PET system is located at 3 meters from the MR system, and uses normal PMT photodetectors with additional shielding. Although not ideal, this system offers the possibility of excellent anatomical soft tissue detail from MR with the functional information from PET in the same system.

Figure 2.25: Ingenuity TF PET/MR scanner produced by Philips [Herzog, 2012].

The developments of APD systems lead to the commercialization of an whole body PET/MR by Siemens (mMR), Figure 2.26. A whole-body ring is inserted into the MR bore for the simultaneous acquisition of PET and MR images.

The new development of SiPMTs will lead to the design of the first simultaneous PET/MR scanners from Philips, and also the first SiPMT-based PET/MR system at all. Yet, this system is still not available commercially.

Lastly, an insert based in APD technology was developed by Siemens for brain studies, although it is only available for research. This system was used for this work and therefore will be further explained.

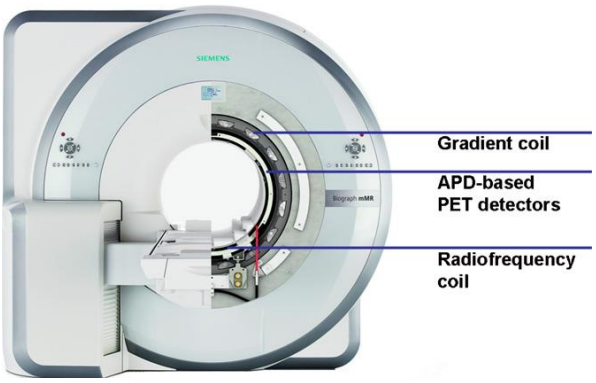

Figure 2.26: Whole-body mMR scanner produced by Siemens [Herzog, 2012].

2.4.3.1 BrainPET

The BrainPET is a MR-compatible 3D-PET system for human brain studies. The BrainPET, developed by Siemens, was installed in Forschungszentrum Juelich in 2008 and since then it is being used for simultaneous acquisition of both PET and MR data. The BrainPET is inserted into the bore of a 3T Magnetom Trio, a Tim System MR scanner, working in a fully integrated environment, Figure 2.27. The system not only allows hybrid imaging, but also the acquisition of PET or MR alone.

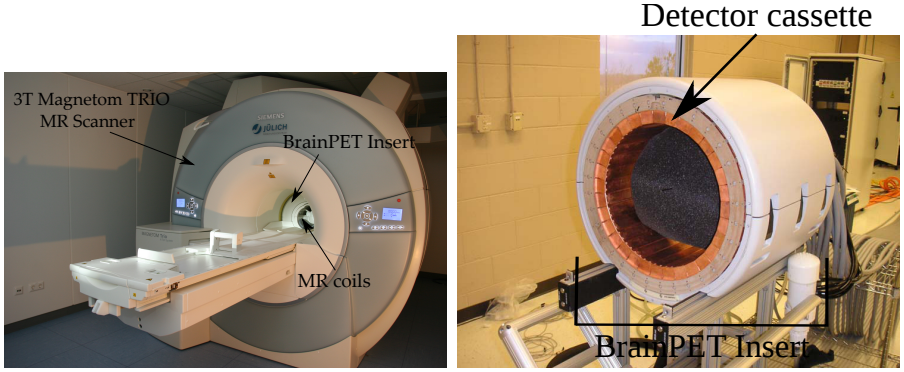

(a) (b)

Figure 2.27: a) Brain PET/MR, a prototype of a PET/MR scanner developed by Siemens; b) BrainPET insert of the Brain PET/MR scanner.

The BrainPET is composed of 32 detector cassettes which form a ring with an outer diameter of 60 cm, inner diameter of 36 cm and a length of 72 cm. Each detector cassette contains six detector blocks made from lutetium oxyorthosilicate (LSO). Each detector block is divided

into a 12 x 12 array of LSO crystals which are read out by a 3 x 3 array of APDs resulting in a total of 27,648 LSO crystals arranged on 192 detector blocks. The size of the individual LSO crystals is 2.5 x 2.5 x 20 mm^3. The axial FOV of the BrainPET is 19.2 cm and the transaxial FOV is 36 cm in diameter. The system makes further use of reflective layers between individual crystals to avoid the passage of incident photons through multiple crystals.

To reduce the problems that the MR scanner induces in the PET system, dedicated RF coils are developed to reduce photon scatter and attenuation in PET. As refereed, APDs are used because of the lower sensibility to magnetic fields when compared to PMTs. Furthermore, the detector cassettes are shielded from RF fields by a copper housing.

Chapter 3

Attenuation correction: State of the art

3.1 Introduction

The attenuation correction (AC) is the subject of this work and will be described in more detail in this chapter.

In the first section (3.2) the effects of attenuation in the reconstructed PET images will be analysed. In the second section (3.3) it will be explained how the AC maps can be used for correcting the PET images. Finally, in the third section (3.4) the methods for deriving the AC maps will be extensively explained, reporting about the first stand-alone PET scanners, the currently widely used PET/CT scanners, and the novel PET/MR scanners, giving an overview of the state-of-the-art of attenuation correction of PET images.

3.2 Effect of attenuation

AC in PET images should be always applied to ensure an absolute quantification. However, in some clinical situations a reconstruction without AC can be also performed.

The effect of attenuation correction on PET quantification was already recognized in the early development of the PET systems by [Huang et al., 1979]. The authors found serious differences between images reconstructed without and with calculated or measured AC resulting in large errors. In summary, the authors concluded that performing correct attenuation correction is mandatory for quantification in PET.

The effect of attenuation and scatter on a homogeneous cylinder is shown in Figure 3.1. It is visible that before any correction the acquired

image presents lower intensity in the center of the image, increasing towards edges, Figure 3.1. As explained in chapter 2 for every LOR attenuation of photons needs to take into account the path connecting the two invoveld detectors, Equation 2.16. Thus, the more material the photons need to pass, the stronger is the attenuation. After correction for attenuation, the intensities of the image redistributed within the cylinder, Figure 3.1 b and e. However, a further processing step (scatter correction) needs to be carried out to effectively homogenize the image, Figure 3.1 c and f.

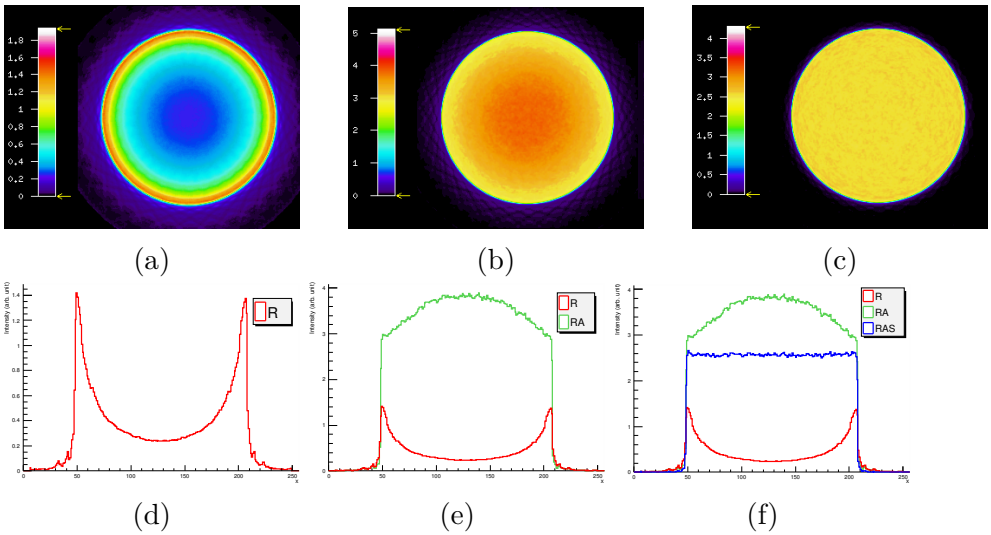

Figure 3.1: Effect of attenuation in a simulated homogeneous cylinder. Top: images before any correction (a), with attenuation correction (b), with attenuation and scatter correction (c). Bottom: profiles of the respective images at top (The images were kindly provided by J. Matos Monteiro).

There has been a less extensive discussion on the attenuation correction of PET images in the clinical environment. In [Bai et al., 2003] attenuation correction of whole-body PET in oncology imaging was studied. The authors reported that all studies should at least be reconstructed with attenuation correction to avoid missing regions of elevated tracer uptake. In [Wong et al., 2000] the purpose of the study was to evaluate the difference between attenuation corrected and non-corrected images in case of lesion detection. The authors showed 3 discordant findings (in 61 patients) with abnormalities on the attenuated corrected images but not on the non-attenuated corrected images. However, in general, a number of studies have shown that an improvement of clinical accuracy is reached when attenuation correction is applied.

3.3 Attenuation correction

Photon attenuation (μ/cm) affects the number of counts in PET scanners directly by reducing some photon from reaching PET detectors. It was already shown in chapter 2 how the beam intensity is reduced by adding the attenuation of photons along line segments A1 and A2, according to Equation 2.16.

Using the geometry represented in Figure 3.2 the acquired emission projection data $P(x', \phi)$ can be represented by Equation 3.1, where the exponential term represents the attenuation along the LOR at detector position s and projection angle ϕ , and where $g(x, y)$ represents the distribution of the radiotracer in the patient.

$$P(x', \phi) = e^{-\int \mu(x,y)dy'} \int g(x, y)dy' \tag{3.1}$$

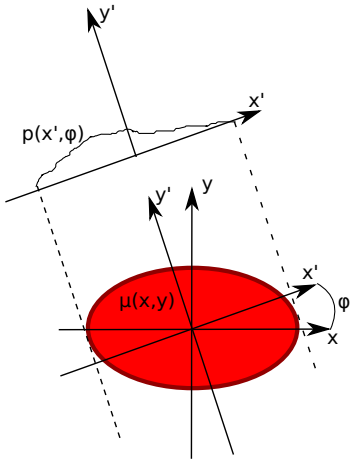

Figure 3.2: Geometry used for projections of the attenuation object (adapted from [Kinahan et al., 2003]).

Attenuation correction attempts to determine g(x,y) by multiplying $P(x, \phi)$ with an attenuation correction factor (ACF), expressed by the inverse of the exponential term in Equation 3.2.

$$P_a c(x', \phi) = ACF * e^{-\int \mu(x,y)dy'} \int g(x, y)dy' = \int g(x, y)dy' \tag{3.2}$$

For transmission methods the ACF can be obtained by the ratio of a blank scan (BL), performed without the patient in the FOV (Figure 3.3 B), and the transmission scan (TX) performed with the patient in the FOV (Equation 3.3) (Figure 3.3 C).

$$ACF = e^{\int \mu(x,y)dy'} = \frac{BL(x',\phi)}{TX(x',\phi)} \tag{3.3}$$

For transmission-less methods attenuation coefficients at 511 keV are derived from a corresponding CT image or assigned to an MR image after segmentation into brain tissue, bone, soft tissue, and background. Then, ACF for an individual sinogram element is calculated by numerically integrating 3.3 along the LOR by forward projection.

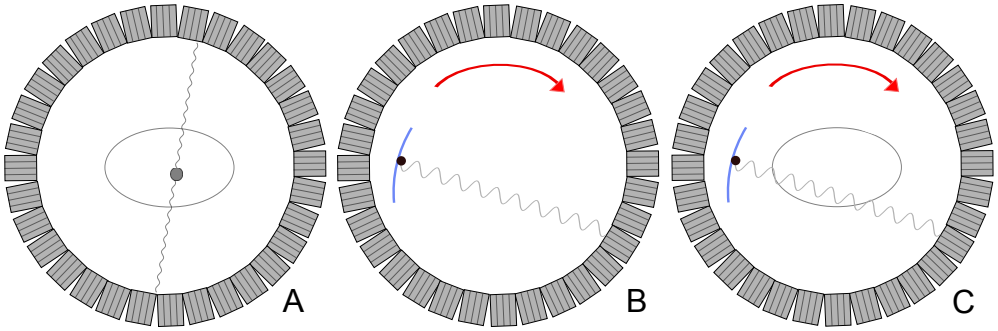

Figure 3.3: Representation of the PET emission scan (A); Blank Scan (B); Transmission Scan (C).

The product of each ACF with the corresponding LOR data yields the corrected projection data which can then be reconstructed to estimate the two-dimensional distribution of radionuclide concentration represented by the function f(x,y). The projection data can be reconstructed by an analytical method such as FBP or an iterative method such as OSEM, [Comtat et al., 1998], with this last one implemented on most commercial PET scanners.

3.4 Methods for deriving AC maps

3.4.1 Attenuation Correction for stand-alone PET

As already reviewed several physical factors can degrade image quality and quantitative accuracy of PET imaging. Among them, attenuation of photons in tissue is one of the most important factors in visual interpretation and quantitative estimation [Zaidi and Hasegawa, 2003].

In former 2D PET attenuation correction factors were usually measured by the use of rod sources rotating around the subject in the FOV. Sources containing high activity concentrations could be used to speed up the process, and scatter could be minimized by a technique called rod

or sinogram windowing, whereby only LORs passing through the rod source were used for transmission measurement [Thompson et al., 1986].

In some studies calculated instead of measured AC [Bergström et al., 1982] was applied mainly to dispense the need of a transmission scan. Also, techniques that segment the attenuation data into regions with proximate linear attenuation coefficients have been implemented, but exclusively for whole body measurements [Xu et al., 1996].

Attenuation correction for standalone PET scanners can therefore be divided into measured, calculated and segmented attenuation correction methods.

3.4.1.1 Measured attenuation correction

Different approaches for measured AC have been tested using coincidence transmission scans and singles transmission scans.

The approach by coincidence transmission data consists in the use of one positron emitter of long half-life as 68Ge-68Ga imbedded in rod sources. The annihilation photons in coincidence are registered as they travel through the body. A transmission scan can take up to 10 minutes and can be performed before or after the radiotracer administration.

In modern PET scanners such as the ECAT Exact HR+ from Siemens 3 rotating rod sources are used, an improvement relatively to older techniques which used only one rod source [Rota Kops et al., 1990] or even older using a ring source. Furthermore, the rotating sources offer the possibility to use the sinogram windowing. During sinogram windowing the detectors are masked electronically to differentiate between collinear LOR with the rod source from those that are not. The registered events by non-collinear LOR with the rod source are rejected, as they correspond principally to scatter and random. Using sinogram windowing allows acquiring the transmission and emission data at the same time reducing the PET examination time [Thompson et al., 1991].

In PET scanners with 2D and 3D scan modes (as the ECAT Exact HR+) the attenuation correction can be made as refereed above, but the transmission scan acquired in 2D. However, there is a PET scanner (HRRT) which allows the acquisition only in 3D [Townsend, 2003] and the use of coincidence transmission scan cannot be applied, because the near-side detectors would suffer a too high flux of single photons. On the other hand source activity cannot be reduced without affecting the transmission data acquired at the far-side detectors.

Alternatives such as the use of singles transmission data have been applied. The transmission measurement is then made along with a point source, where the near-side detectors are shielded from the source and

the data are gathered by the far-side detectors as single photons, instead as coincidence photons.

The use of singles transmission data has the advantage of a higher count rate since only one photon has to be registered and the shielding of the near-side detector allows the increase of the source activity without jeopardize the detector dead time. This method has however disadvantages, namely the impossibility of the use of sinogram windowing because of the missing coincidence to determine the associated LOR.

3.4.1.2 Calculated Attenuation Correction

In the different techniques refereed before for standalone PET the transmission scan is a significant part of the clinical scan time. Also, it is responsible for an additional radiation dose to the patient. Therefore, AC techniques without the necessity of a transmission scan were studied.

One method that does not need a transmission scan is the calculated attenuation correction. This method assumes a regular geometric contour of the body (or uses some kind of contour finding) and a uniform density of the tissue within the contour, [Bergström et al., 1982, Rota Kops et al., 2007]. It was mainly developed for the brain, where the bone and soft tissues can be taken into account. Note that it was already shown [Catana et al., 2009] that an accurate identification of the bone is necessary and a method to precisely identify the bone is essential.

Although the calculated attenuation correction avoids a transmission scan the results are biased, leading e.g. to an underestimation of the attenuation in the lateral and parietal lobes up to 20% [Townsend, 2003].

3.4.1.3 Segmented Attenuation Correction

Attenuation correction factors are usually computed by taking the ratio of a blank scan over the measured attenuated distribution of photons transmitted through the patient, Equation 3.3. Normally two-dimensional smoothing is applied to transmission sinograms before dividing by the blank scan to determine attenuation correction factors (ACF). However, this leads to resolution mismatch and noise propagation [Townsend, 2003]. Furthermore, noise from the transmission scan can contributes significantly to the statistical quality of the final emission image [Huang et al., 1979].

Alternatives such as segmented-based attenuation correction approaches have been suggested to reduce noise propagation from transmission scans. These consist of a delineation of anatomical regions

with different attenuation properties either by manually defined, semi-automatic, or fully-automatic methods. Finally assignment of known tissue-dependent attenuation coefficients using weighted averaging in the attenuation images is performed [Zaidi et al., 2007]. The segmented attenuation maps are then forward projected to generate ACFs to be used in PET-AC with reduced noise [Zaidi et al., 2007]. Examples can be found in [Huang et al., 1981] which used boundary methods, in [Yu and Nahmias, 1996] with artificial neural networks, or in [Bilger et al., 2001] with histogram-fitting.

3.4.2 Attenuation correction for PET/CT

The developments in dual-modality PET/CT have revolutionize imagiology techniques as the possibility to acquire anatomical plus functional imaging in the same scanner and in the same position yielded better possibilities to detect and to stage diseases, to monitory and to plan treatments. PET/CT modality sees its wide applications in clinical oncology, neurology, and cardiology by improving lesions localization and possibility of accurate quantitative analysis.

Clinical diagnosis is supported by different types of imagiology with complementary information such as MRI and CT for anatomical information or Single-Photon Emission Computed Tomography (SPECT) and PET for functional information. This need for different modalities derives from the fact that some diseases cannot be characterized with only one technique. As an example, MR or CT are widely applied to the diagnoses and staging of cancer and treatment plan, yet cannot characterize the tumor (benign or malign, slow or rapid proliferation).

The development of PET/CT scanners was a breakthrough in imagiology techniques in comparison to stand-alone PET, as it offers numerous advantages such as better anatomical detail derived from the CT, improving accuracy in lesion localization and treatment planning. Furthermore, the CT-based attenuation maps can be acquired in some seconds instead of the typical 10 minutes in conventional brain studies for stand-alone PET or up to a total of 1 minute instead of the 3 minutes per bed position in conventional whole-body scans. On one hand this reduces the scan time needed for the patient and health-care professionals, on the other hand the high anatomical details provided by the CT increases the differentiation between high activities derived from normal physiology such as brain or bladder, and lesion location [Townsend, 2003].

However, as any other imaging technique, the imagiology of PET-CT has its disadvantages, namely: any type of metal such as implants cannot be scanned, resulting in streak artefacts, [Ay and Sarkar, 2007]; the arms

of the patient may not accommodate correctly in the CT scanner leading to truncation artifacts in the reconstructed PET-CT image [Kinahan et al., 2003]; incompatibility between PET and CT images, derived from uncoordinated respiratory motion, can be observed if appropriate protocols are not taken; Hounsfield (CT units) values are linear related to the linear attenuation coefficients up to zero (for air), but they show different values for bone structures due to the polychromatism of the CT spectrum. This means, the relation between the Hounsfield values and the linear attenuation coefficients are dependent on the X-ray tube voltage [Ay and Sarkar, 2007].

Concluding, the advantages of using CT data instead of external radionuclide sources can be enumerated as following: the CT provides an attenuation map faster and with lower statistical noise than the conventional methods of stand-alone PET; it does not need regular replacement of the transmission source (as the 68Ge-68Ga source); it can acquire attenuation data after injection of the radiotracer. However, as referred before, the data acquired by the CT scanner do not correspond exactly to the linear attenuation coefficients at 511 keV, so different methods have been studied to convert Hounsfield values into linear attenuation coefficients at 511 keV for PET correction such as scaling, segmentation, hybrid, bilinear scaling and dual-energy decomposition.

3.4.2.1 Segmentation algorithms

The CT data are reconstructed in Hounsfield Units (HU) and cannot be converted directly to an attenuation map for PET correction. One possible method segments the CT image into different tissues and assigns known linear attenuation coefficients at 511 keV to each of these regions [Kinahan et al., 2003]. It follows the advantage of reducing the noise presented in the image. Furthermore, in contrast enhanced CT images it is known that attenuation factors generated from non-segmented images may show artefacts derived from overlap of the high intensity bone pixels and contrast-enhanced soft tissue pixels. Moreover, same tissues can present continuously varying densities that may not be accurately represented by a discrete set of segmented values. Thus, discrete attenuation coefficients may not always be sufficient, and a continuous range is needed as e.g. in case of the lung density which changes as much as 30% [Kinahan et al., 1998].

3.4.2.2 Scaling algorithms

Theoretically if the values obtained by CT were linearly related to the attenuation coefficients at 511 keV, it could be possible to obtain an

attenuation map by the multiplication of the CT values with the ratio of attenuation coefficients of water at PET energies μ_w^{PET} and at CT energies μ_w^{CT}. This approach is supported by the fact that the ratio of the attenuation coefficients at 511 keV and 70 keV is constant for all tissue types except bone [Kinahan et al., 1998, Rong, 2009].

Studies were carried to investigate different techniques for scaling attenuation coefficients from CT energies to 140 keV SPECT, being shown that although linear scaling was reliable for low-Z materials, it was a poor approximation for bone [LaCroix et al., 1994, Shreve and Townsend, 2011].

3.4.2.3 Hybrid and bilinear algorithms

To account with the problems arising in both methods refereed before, new algorithms based on both techniques, called hybrid techniques were developed [Kinahan et al., 2003]. They consist primarily in separating the bone from the non-bone tissues with a threshold applied to the CT values and then applying different scaling equations to the bone and the non-bone tissues (Figure 3.4 blue) (Equation 3.4).

$$\begin{cases} \mu^{PET} = 0.096cm^{-1} \times (1 + \frac{HU}{1000}), HU < 300 \\ \mu^{PET} = 0.081cm^{-1} \times (1 + \frac{HU}{1000}), HU > 300 \end{cases} \tag{3.4}$$

Another method that tried to solve the problem of non-linearity between the bone and non-bone tissues is the bilinear algorithm [Burger et al., 2002]. This method considers that regions with Hounsfield Units (HU) between -1000 and 0 are represented by mixtures of soft tissue and lungs while above 0 by mixtures of soft tissue and bone. Thus, a threshold separating both mixtures is first applied and then different scaling equations to both mixtures are considered (Figure 3.4 red) (Equation 3.5) with $\mu_{water}^{PET} = 0.096cm^{-1}$, $\mu_{bone}^{PET} = 0.172cm^{-1}$, $\mu_{water}^{CT} = 0.184cm^{-1}$ and $\mu_{bone}^{CT} = 0.428cm^{-1}$

$$\begin{cases} \mu^{PET} = \mu_{water}^{PET} cm^{-1} \times (1 + \frac{HU}{1000}), HU < 0 \\ \mu^{PET} = \mu_{water}^{PET} + \mu_{water}^{CT} \times \frac{HU}{1000} \times \frac{\mu_{bone}^{PET} - \mu_{bone}^{CT}}{\mu_{bone}^{CT} - \mu_{water}^{CT}}, HU > 0 \end{cases} \tag{3.5}$$

Although some differences between the hybrid and bilinear algorithms exist, both methods had shown to give similar and reasonable results. However, they do not account for different kVp (tube voltage) values and make assumptions about the locations of thresholds and breaking points.

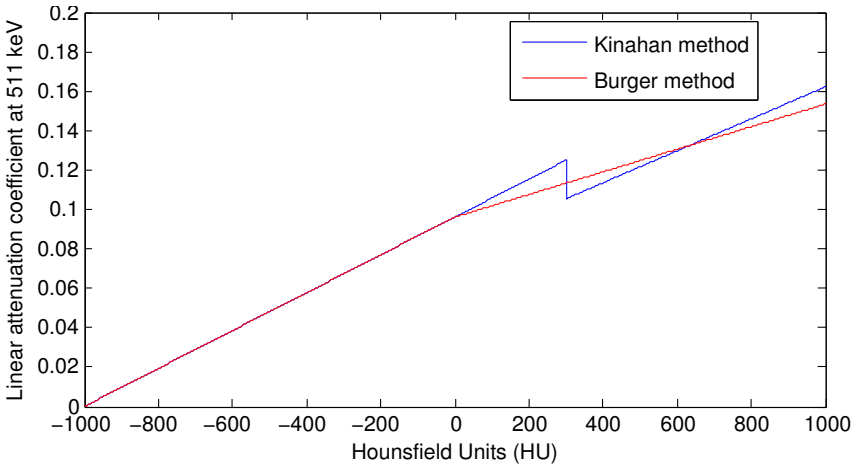

Figure 3.4: Comparison between μ^{511keV} for CT values ranging from -1000 HU to 1000 HU for both Kinahan and Burger methods.

To overcome this problem [Carney et al., 2006] proposed a method that takes into account the different kVp values in the transformation of the HU values to 511 keV linear attenuation coefficients. Table 3.1shows The kVp-dependent values a, b, and the break point (BP) defining the transformation, given in Equation 3.6. The kVp-dependent values were estimated by a detailed calibration measurement at each kVp, for which the measured HUs were associated with known linear attenuation values at 511 keV for a variety of reference tissues. A bilinear transformation was then defined by fitting to the reference tissue measurements.

$$\begin{cases} \mu^{PET} = 0.096cm^{-1} \times (HU + 1000), HU < BP \\ \mu^{PET} = a \times (HU + 1000) + b, HU > BP \end{cases} \tag{3.6}$$

Table 3.1: kVp-dependent values a, b, and break point (BP) defining the transformation, given in Equation 3.6, from HU to 511 keV linear attenuation values [Carney et al., 2006].

kVp	$a(\times 10^{-5} cm^{-1})$	$b(\times 10^{-2} cm^{-1})$	Break point (BP) (HU+1000)
80	3.64	6.26	1050
100	4.43	5.44	1062
110	4.92	4.88	1043
120	5.10	4.71	1047
130	5.51	4.24	1037
140	5.64	4.08	1030

3.4.2.4 Dual energy decomposition algorithms

Attempts in obtaining directly the attenuation coefficients from the CT images were further studied, [Guy et al., 1998]. The problem regarding non-linearity between CT values and attenuation coefficients comes from the fact that both Compton scattering and photoelectric absorption are the most important processes in CT imagiology (Compton scattering for non-bone tissues and a mixture of Compton scattering and photoelectric absorption for bone). Thus, the problem can be seen as estimating the attenuation derived from both Compton scattering and photoelectric absorption, which is a two variable problem. One method is based on dual energy CT images, i.e., two CT scans were obtained for each patient with different tube voltages [Ay and Sarkar, 2007]. In this way, it was possible to decompose both interactions and to obtain an improved attenuation map. Summarizing, dual energy decomposition method is not recommended for attenuation correction due to its complexity both in clinical practice and calculation [Beyer et al., 1995].

3.4.3 Attenuation correction for PET/MR

Possible ways to estimate AC maps in a PET/MR scanner can be derived from attenuation correction methods for standalone PET devices and PET/CT scanners. One possibility is the use of emission data such as in a stand-alone PET system, [Censor et al., 1979, Salomon et al., 2011, Tai et al., 1996]. Otherwise, information from the MR can be used to improve AC map estimation.

The attenuation map needed in PET should reflect the tissue-density distribution across the image volume as given in a CT image. Yet, in MRI the voxels of the images correlate with the hydrogen nuclei density

in tissues and with the relaxation properties of tissues instead of with the mass attenuation coefficients.

One possible and straight way to overcome this problem is first to segment the relevant regions and then assign the different attenuation coefficients to the corresponding tissues. Several methods have been investigated based on different MR sequences. However, one of the major problems of such approach is the assumption of a single constant attenuation value within each of the segmented tissues, which of course does not correspond to the reality.

Approaches that do not segment the MR images were also investigated, mostly aided by template or atlas images. On contrary to the segmentation-based approaches, these methods are not dependent on the number of segmented structures and therefore may account for different attenuation values even within the same tissue. Nevertheless, as these methods assume that inter-subjects anatomy is similar, estimation of attenuation coefficients in regions with high anatomy variability tends to present high errors.

3.4.3.1 Segmentation-based MR-AC

In the segmentation-based methods the MR image is first segmented into different classes. Second, to each voxel belonging of a region class the corresponding linear attenuation coefficient is assigned, Figure 3.5. As previously referred, the non-existence of a one-to-one relationship between the MR signal and the electronic density can cause some problems in the direct mapping of MR intensities to linear attenuation coefficients. For example, in conventional MR sequences air and compact bone produce the same very low signal, but the attenuation coefficients of these two regions are largely different [Hofmann et al., 2008, Schreibmann et al., 2010].

The MR-AC by segmentation approaches was proposed by [Le Goff-Rougetet et al., 1994] in the 1990s,whereby the MR image was first registered to the PET transmission image, then it was segmented into three tissue classes and to which finally different attenuation coefficients were assigned. Segmentation approaches for MR-AC were also developed by [Zaidi et al., 2003] who adapted an ellipse to the PET emission image for a rough attenuation map and then segmented the MR image by fuzzy logic assigning specific attenuation coefficients to the different tissues.

More improvements were made to increase the accuracy of the segmentation- based methods using anatomical background knowledge to better distinguish particular brain regions. A method proposed by [Wagenknecht et al., 2009] uses a new knowledge-based segmentation approach applied on T1-weighted MR images. It examines the position and

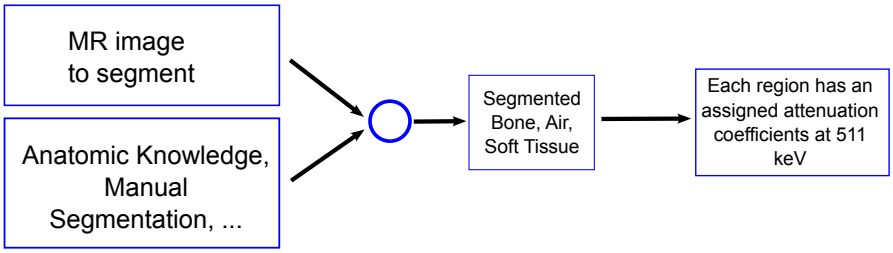

Figure 3.5: Scheme showing how a segmentation-based MR-AC map for AC of PET data is obtained. First, the MR image is segmented into, e.g., 3 region classes: soft tissue, air, and bone using general anatomical information, manual segmentation by the physician, or others. Next, to each segmented class a specific attenuation coefficient is assigned.

the tissue membership of each voxel and segments the head volume into attenuation-differing regions: brain tissue, extracerebral soft tissue, skull, air-filled nasal and paranasal cavities as well as the mastoid process.

The low signal intensity from the cortical bone in conventional sequences derives from the short T2 and the low content of water. As the relaxation of the protons in this tissue occurs rapidly, MRI signal fades before it is registered. Therefore, other methods based on different MR sequences than conventional ones are used to image tissues with short T2. In [Robson et al., 2003] a MR sequence called Ultrashort Echo Time (UTE) is proposed to image cortical bone. In theory, the bone tissue could be identified if data were acquired at 2 echo times such that the signal from the bone is present in the first echo (UTE1), but not in the second echo (UTE2) dataset, whereas the signals from other tissues, i.e. soft tissue and air, are similar in both cases.

UTE sequences were further explored in [Catana et al., 2010, Keereman et al., 2010] where an UTE pulse sequence is used to segment MR images into air, soft tissue and bone.

In Catana's method bone and air are segmented by a combination of both UTE1 and UTE2 MR images. For bone tissue, the original UTE1 and UTE2 volumes are first divided by the corresponding smoothed volumes obtained after applying a 3-dimensional Gaussian low-pass filter with a 20-mm-radius kernel (for reducing RF coil artefacts). The resulting datasets are combined by the transformation $(UTE1 - UTE2)/UTE2^2$ to enhance the bone tissue voxels. A segmentation of bone tissue is performed by thresholding this final volume. For air cavities the low-pass filtered data are combined using the calculation $(UTE1 + UTE2)/UTE1^2$. Again a segmentation of air cavities is performed by thresholding the resulting volume. For soft tissue, a mask is first derived from the UTE2 volume and all voxels that are not bone or

air inside the mask are assigned as soft tissue.

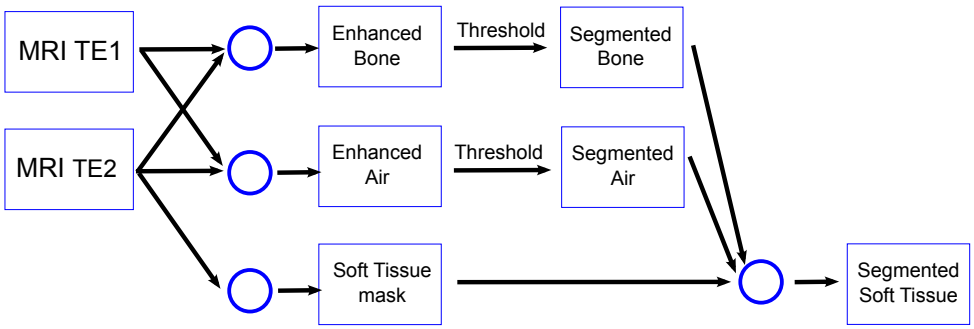

Figure 3.6: Scheme showing the workflow to obtain the segmentation-based MR-AC map for AC of PET data proposed by Catana. First, enhancement of bone and air are performed based on operations with both UTE MR images at different echo times. Second, a threshold is applied to segment bone and air from the enhanced bone and air images, respectively. A soft tissue mask is derived from the second echo MR image and a segmented image of the soft tissue is calculated including all voxels in the mask that are not bone or air

In Keereman's method bone enhancement is obtained by the estimation of a R2 map (inverse of spin-spin relaxation time T2) from the UTE1 and UTE2 volumes, Equation 3.7. Then, an air mask is generated from the first echo MR image by thresholding and region growing to correct the R2 map. This corrected R2 map is multiplied by the air mask and then segmented in bone, air and soft tissue by thresholding.

$$R2 = \frac{ln\,(UTE1) - ln\,(UTE2)}{TE_2 - TE_1} \tag{3.7}$$

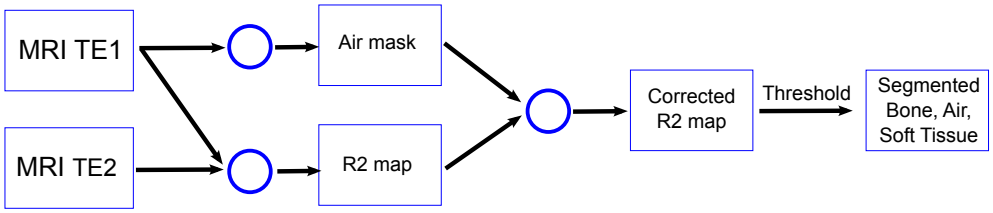

Figure 3.7: Scheme showing the workflow to obtain the segmentation-based MR-AC map for AC of PET data proposed by Keereman. First, a R2 map is calculated from both MR images at different echo times. Second, an air mask is generated from the first echo MR image by thresholding and region growing. Multiplication of the air mask with the R2 map is performed to correct the R2 map. Finally segmentation of bone, air and soft tissue is calculated by thresholding.

3.4.3.2 Template/Atlas-based MR-AC

As a first step of Template/Atlas-based MR-AC methods an MRI template together with an attenuation template or an MR/CT atlas must be build. Template based MR-AC and Atlas-based MR-AC follow almost the same methodology, although some differences must be noted. In the former method an average of the MR and attenuation images of several normal subjects after adaption to a standard reference space is performed, Figure 3.8 A, [Rota Kops and Herzog, 2008]. In the latter method a match (coregistration) between MR and CT from several normal subjects is performed yielding a MR/CT atlas database, Figure 3.8 B, [Hofmann et al., 2008]. This last method differs from the first one as the CT images cannot be averaged so that the high resolution of the images is maintained.

The template-based approach starts with an MRI template and an attenuation template. The MR template is firstly registered Figure 3.9 A, to the patient MR image with a non-rigid transformation (mostly a rigid or semi-rigid transformation followed by a non-linear deformation), then the transformations are applied to the attenuation template Figure 3.9 B. The attenuation image generated in this way is specific for the patient. The attenuation map generated in this way is specific for the patient. The MR and transmission templates were obtained from the average of MR and transmission images of 8 patients represented in the same space. The method shows to be a promising alternative to the segmented-based MR-AC methods which are still in development with segmentation's accuracy still arguable.

The Atlas-based starts with a MR/CT atlas database of 17 image pairs, Figure 3.10. The MR images from the database are registered to a

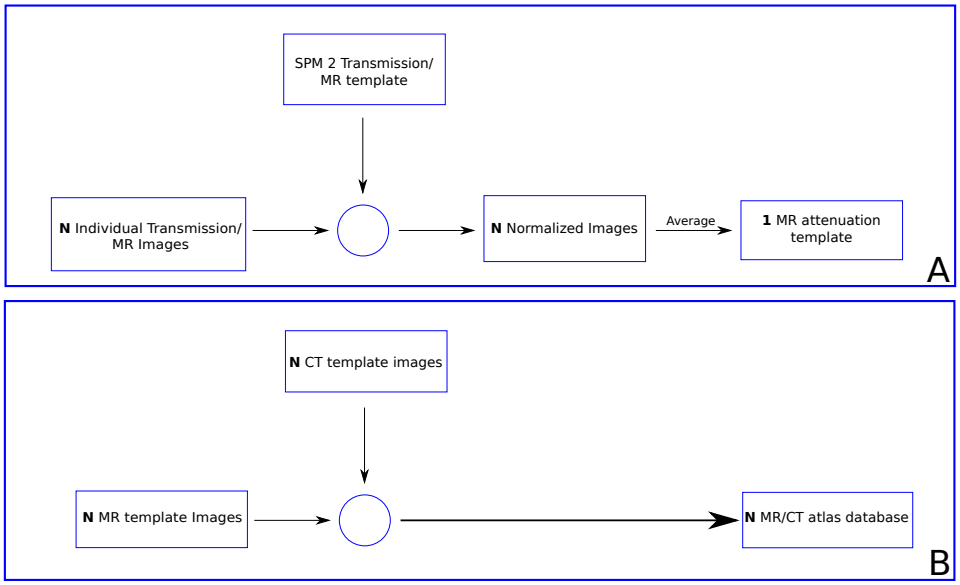

Figure 3.8: A- Generation of a template image to be used in [Rota Kops and Herzog, 2008] AC method; B- Generation of an MR-CT Atlas database to be used in [Hofmann et al., 2008] AC method.

patient MR image with a non-rigid transformation, then the transformations are applied to the respective CT image of the atlas database. The 17 spatially transformed MR and CT images are then used to generate a pseudo-CT image with the help of a pattern recognition approach. The pseudo-CT image is then scaled to attenuation coefficients at PET energies and used for attenuation correction. The main goal of the study was to develop a method that not only uses the registration between subjects as an input signal, but also generate correct predictions in the case of local registration errors. The method tries to obtain attenuation values indirectly by generating pseudo-CT values in a continuous scale obtained from the MR image of the patient. The method showed to be applicable not only for the brain AC, but also for the whole-body AC,

The approach is not as direct as the template-based method, and has three major drawbacks: First, the coregistration of MR and CT images is not trivial (e.g. automatic methods may lead to suboptimal parameters); Second: the complexity and the high computational time comsuming of the generation of the pseudoCT; third: as the method generates pseudo-CT images the problems in transforming CT values to attenuation coefficients at 511 keV applies to this method as well.

Template-based and Atlas-based MR-AC were first presented first in 2008 and developments regarding these kind of approaches are being carried on. Although the use of these last presented methods show to

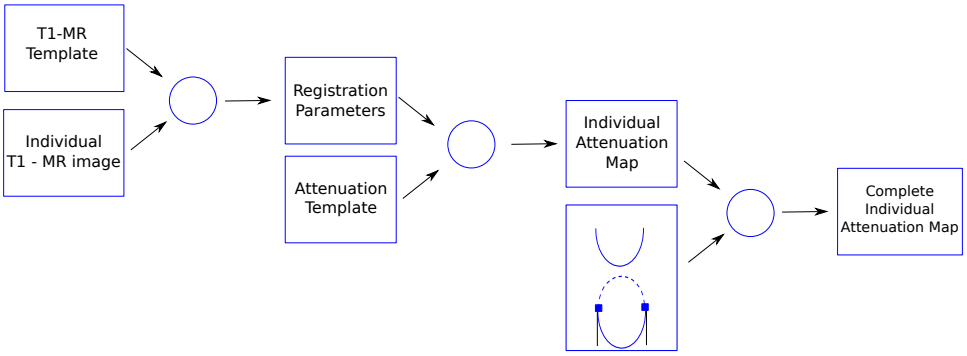

Figure 3.9: Scheme showing the workflow to obtain the template-based MR-AC map for AC of PET data proposed by Rota Kops. The MR template is normalized to the patient's MR and the transformations applied to the attenuation template to generate a specific attenuation image for the subject. Finally the coils are added to the attenuation image to generate a complete attenuation map to be used in PET correction (adapted from [Rota Kops and Herzog, 2008]).

be easier than the segmentation-based methods the accuracy is strongly dependent on the spatial normalization procedure used. Some methods have been developed to get a better normalization of the MR image of the patient with the MR template, when some anatomical differences or noise in the MR are present [Schreibmann et al., 2010].

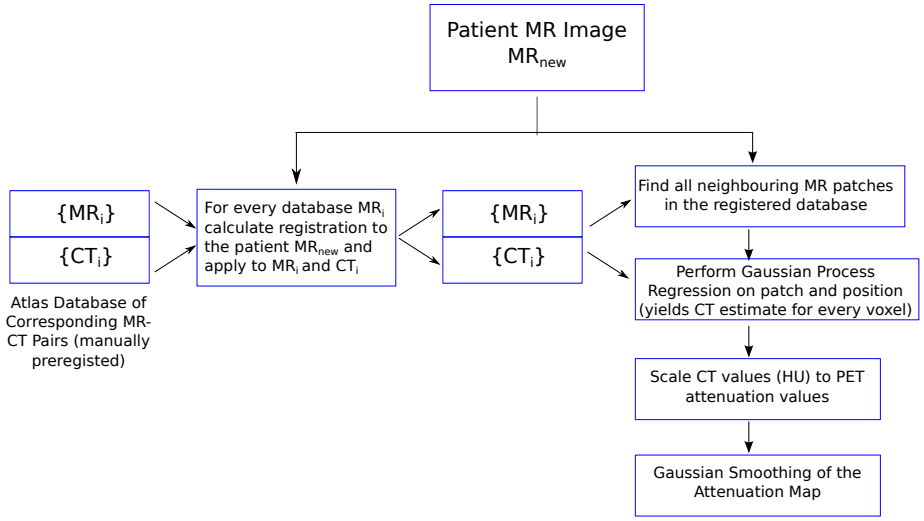

Figure 3.10: Scheme showing the workflow to obtain the atlas-based MR-AC map for AC of PET data proposed by Hoffmann et al.: (i) Registration of all MR images in the atlas database to the one patient's MR, (ii) application of the transformations to both MRs and corresponding CTs, (iii) combination of Local Pattern Recognition with Atlas Registration, (iv) scaling of the CT values of the generated pseudo-CT to PET attenuation values and (v) smoothing of the resulting attenuation map to match the resolution of the PET emission scan (adapted from [Hofmann et al., 2008])

Chapter 4

MR/CT artefacts analysis

4.1 Introduction

As it was introduced MR artefacts may induce several problems in both clinical analysis and automatic image processing such as co-registration or segmentation. In the present study, 3 types of artefacts were identified as problems for learning and/or classification of the proposed methods and are metal, motion and intensity inhomogeneity (IH) artefacts. Therefore analyse of these artefacts was carried and possible corrections suggested.

4.2 Material and Methods

MR data were acquired in 9 subjects. The MR UTE sequence installed at the 3T MR/BrainPET scanner in the Forschungszentrum Juelich Lab was acquired with flip angle = 10° , TR = 200 ms, and TE1=0.07 ms and TE2=2.46 ms, resulting in 192 sagittal 192×192 images with a voxel size of 1.67 mm^3.

All subjects underwent also a CT scan which was used for comparison. They were acquired on different scanners with different standard parameters.

The CT data were converted to attenuation values at 511 keV using [Carney et al., 2006] method. This method was chosen as it takes into account different kVp values.

Next, the CT data were co-registered to the corresponding MR data. The statistical parametric mapping tool SPM8 was used for the coregistration. It uses normalized mutual information as objective function and trilinear interpolation.

CT and MR data were visually analyzed for co-registration, metal, motion, and IH artefacts.

Moreover, a water-filled cylindrical phantom was used to measure the spatial influence of IH in a homogenous structure. The cylindrical phantom was placed in the 3T hybrid MR-BrainPET and an UTE-MR sequence was acquired. The MR-UTE sequence was performed with the same parameters as used for the human subjects.

The water-filled cylindrical phantom should provide a homogeneous image inside the field of view (FOV); possible homogeneities would be then related directly with the noise and IH acquired by the scanner. The model that defines the relation between the ideal image and the measured image can be described by Equation 4.1, where u_k is the measured image, v_k the ideal image, s_k the multiplicative bias field, n_k random noise and the index k in all variables indicate each image channel.

$$u_k(x) = v_k(x)s_k(x) + n_k(x) \tag{4.1}$$

Now, neglecting the noise n acquired by the scanner and assuming homogeneity of the phantom, the bias field for each position in FOV can be determined directly from the cylindrical phantom image, Equation 4.2.

$$s_k(x) = \frac{u_k(x)}{v_k(x)} = \frac{u_k(x)}{C} = u_k(x) \times C \tag{4.2}$$

,where C is a constant factor.

To verify if the assumption that a simple water phantom can estimate bias inhomogeneities, a subject underwent an UTE-MR scan in the same week and a comparison with the water phantom data was performed. **A ratio between the measured phantom MR and subject MR images was performed to estimate a bias-free image.**

4.3 Results

4.3.1 Co-registration artefacts

The coregistration between the MR and the corresponding CT-based attenuation map for all subjects showed to be acceptable, although some mismatch could still be observed. In Figure 4.1 the coregistration between CT and MR data for 3 subjects is shown. The subject in the top row exhibits mismatches in the facial area similar to those on the head's top of the subject in the middle row. The reasons for that can be several: the coregistration algorithm failed or the MR images exhibit some artefacts. For this second subject the mismatch in the neck area is clearly due to different head holders in the different scanners. The same reason is valid for the mismatches for the subject in the bottom row.

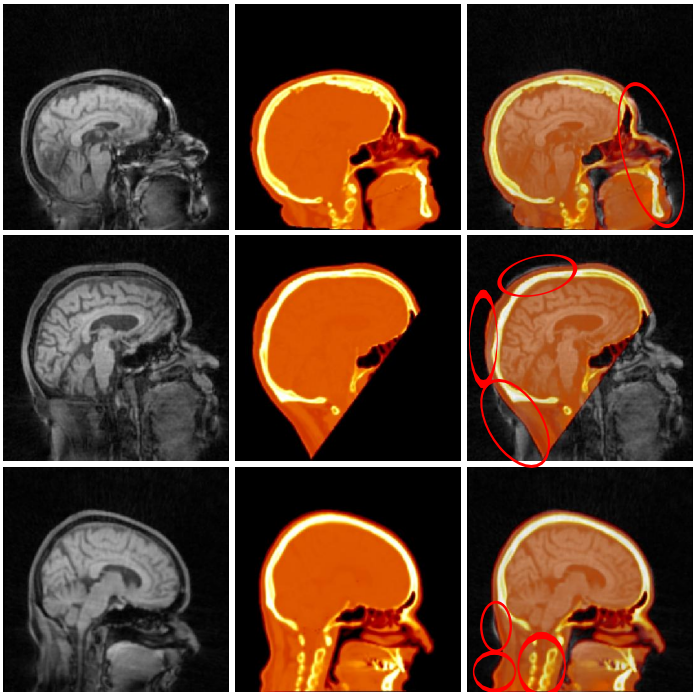

Figure 4.1: Coregistration problems for 3 different subjects. At left: MR images; at the center: CT images; and at right: fusion of CT and MR images. Ellipsoids point out mismatches between the CT and MR images.

4.3.2 Metal artefacts

Although metal artefacts are clearly a problem to typical MR sequences as it was presented in chapter 2, it was also shown to have less impact on UTE sequence, Figure 2.14. The acquired data were observed for metal artefacts and 3 of the 8 subjects were inspected for metal dental implants. The subjects having metal implants are given in Figure 4.2 showing both UTE images with TE1 and TE2, respectively, and the co-registered CT images. Metal artefacts have few impact on both UTE images, yet streak artifacts can be seen in the CT images for all subjects.

4.3.3 Motion artefacts

On contrary to metal artefacts, motion artefacts are a problem in any image modality. Similar to metal artefacts, the acquired data were inspected for motion artefacts and effectively 5 of the 8 subjects showed strong motion artefacts in the facial region, but only in the UTE2 images. The results for the 3 subjects that presented the strongest motion artefacts are shown in Figure 4.3 for both UTE images and co-registered

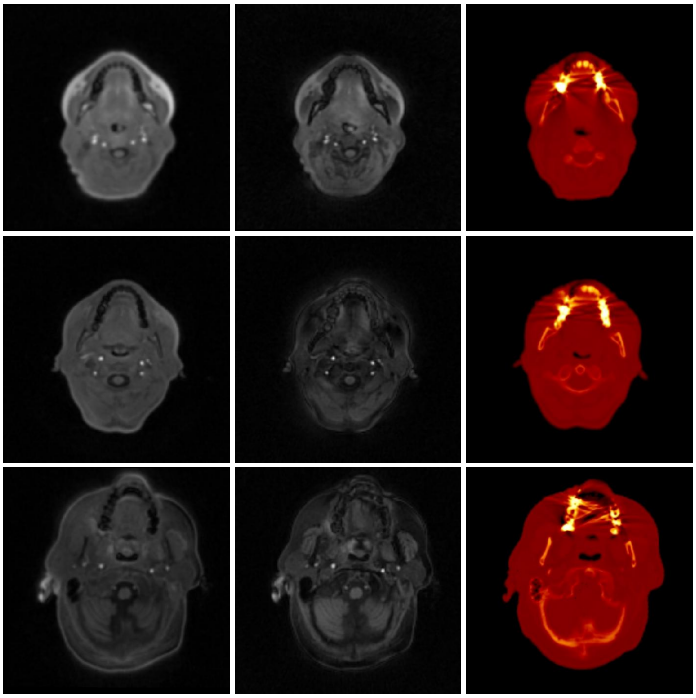

Figure 4.2: Metal artefacts for 3 different subjects. At left: UTE1 images; at the center: UTE2 images; and at right: CT images. Streak artefacts can be seen in the CT images.

CT images. Air cavities cannot be correctly distinguish in all 3 subjects, and additionally also facial and neck bone suffered deformations. The sequence at the second echo with TE2=2.46 ms is clearly much more sensible to slight movements than at the first echo with TE1=0.07 ms, as can be seen in the left column of Figure 4.3.

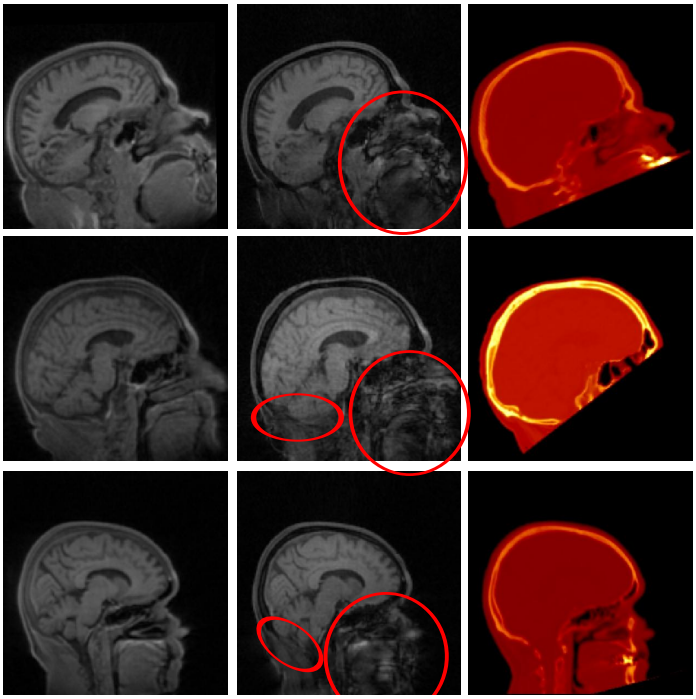

Figure 4.3: Motion artefacts for 3 different subjects. At left: UTE1 images; at the center: UTE2 images; and at right: CT images. Ellipsoids represent regions of strong motion artefacts in the UTE2 images.

4.3.4 Intensity inhomogeneity artefacts

Regarding IH all subjects showed visually regions of moderate up to high artefacts. The results for 3 subjects that presented IH artefacts are shown in Figure 4.4. Here the colour scale was chosen such that the inhomogeneities can be better seen.

The UTE1 images (Figure 4.4, first column) of all subjects showed lower intensities, in the first transaxial slices. Additionally, higher intensities can be seen at the nose of subject A, near the frontal sinus of subject B and at the occipital region of subject C.

The UTE2 images (Figure 4.4, second column) are more difficult to analyze due to the motion in the facial area. Yet some region of moderate to high intensities can be identified: at the parietal region of subject A, near the frontal sinus of subject B and at the occipital region of subject C.

The difference images (Figure 4.4, third column) between UTE1 and UTE2 clearly visualize the effects of IH. For all subjects they occur near the frontal sinus and the occipital region. Moreover, for subjects A and B IH occur at the parietal region while for subject C at the neck region.

In Figure 4.5 the phantom data and the UTE1 MR images (top and

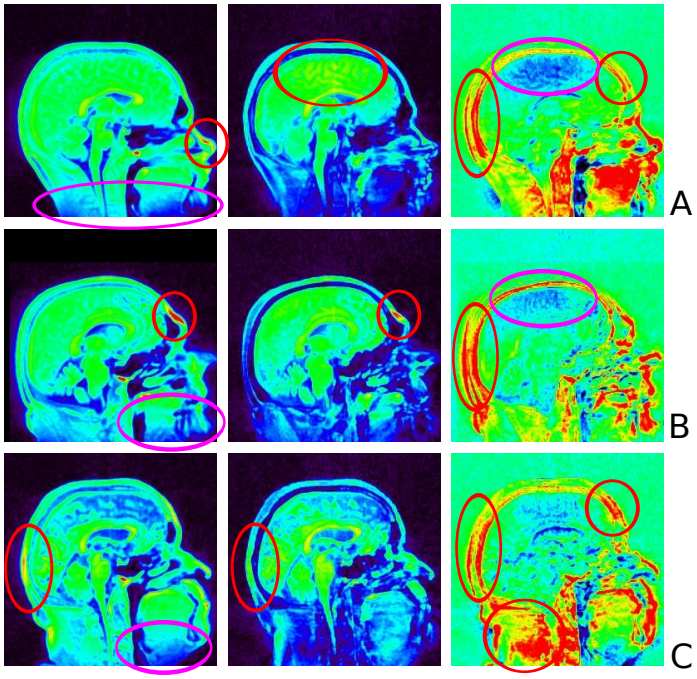

Figure 4.4: IH artefacts for 3 different subjects. At left it is presented the UTE1, at the center the UTE2 and at right difference between UTE1 and UTE2. Red ellipsoids represent regions where high bias was verified. Red ellipsoids represent regions where very high MR intensities are visible; Violet ellipsoids represent regions where very low MR intensities are visible.

middle row, respectively) of the subject as explained in Chapter 4.2 are presented. As can be seen both images present a decrease in intensity from top to the bottom of the sagittal view (i.e., along the z axis of the scanner). Additionally, in the transaxial view as the phantom touches the head coils the image intensities increase heavily. In Figure 4.6 the phantom data and the UTE2 MR images (top and middle row, respectively) are presented. As in UTE1 a decrease in intensity from top to the bottom along the z axis of the scanner is observed as well as the intensity increase when the phantom touches the head coils. To verify if the phantom image experiences the IH observed in the subject data a simple division of the subject MR image with the phantom MR image was performed. The bottom row in Figure 4.5 and 4.6 shows these ratios. Where phantom and subject presented signal it is verified an increase in homogeneity in every view, for both images.

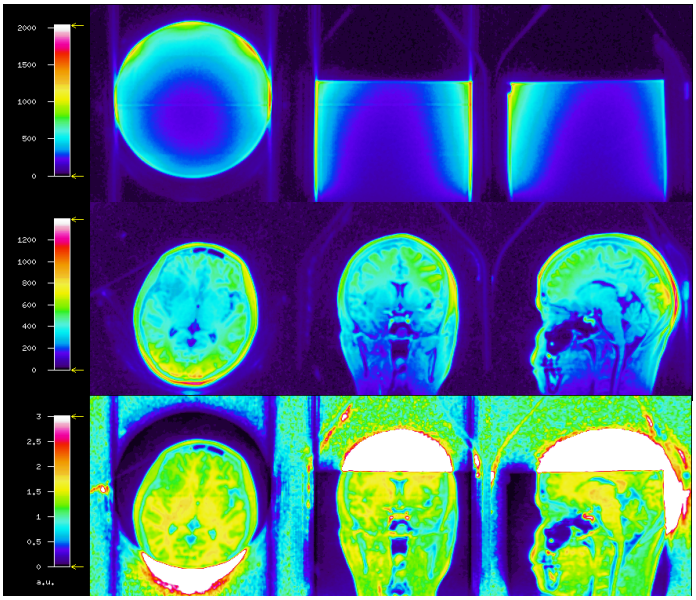

Figure 4.5: Phantom image (top row) and subject UTE1 (middle row). Both images were acquired separately, but within the same week. In the bottom row the division of the middle row by the top row is represented.

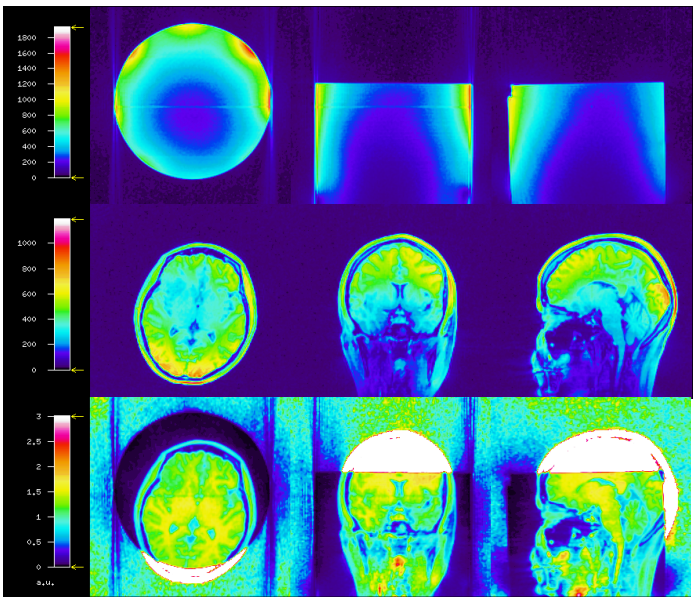

Figure 4.6: Phantom image (top row) and subject UTE2 (middle row). Both images were acquired separately, but within the same week. In the bottom row the division of the middle row by the top row is represented.

4.4 Discussion

4.4.1 Co-registration artefacts

Perfect coregistration between CT and MR data was not straightforward as the two modalities were acquired at different scanners. Slight mismatches were observed between the CT and MR data, Figure 4.1. Moreover, in some cases the position of the head in the CT scanner is very different from the orientation of the head in the MR scanner, resulting in high differences between the CT image and the MR image, Figure 4.1 (2^{nd} row). In the specific example the CT data was acquired with the head bend to the chest so that the eyes were not imaged (this was done to avoid the dose in the eyes) and the soft tissue in the neck was stretched. In the MR scanner in opposite the head was relaxed and the soft tissue in the neck was not stretched. In the MR scanner in opposite the head was relaxed and the soft tissue in the neck was not stretched.

These mismatches can influence AC methods in two ways. First, AC methods that optimize their parameters without user-interaction (autonomous methods) generally use a reference image such as a CT image co-registered to the subject MR images. If the CT image is not perfect co-registered, the autonomous methods will not converge to the best parameters, and the derived AC map will not be optimized. Second, interpretation of AC methods by comparison of the generated AC map with the CT-derived AC map will not be completely correct. As a voxel in an AC map influence all LOR that pass through it the influence of the mismatch in the reconstructed PET image is not only local but also global. For better co-registration it is therefore suggested to acquire CT and MR images with the same head position. This can be accomplished using some head immobilization device in both CT and MR scanners.

4.4.2 Metal artefacts

Although metal artefacts are a problem to typical MR sequences as it was presented in chapter 2, it was however shown to have less impact on the UTE sequence, Figure 2.14. In fact, it was observed in Figure 4.2 that metal implants do not introduce relevant artefacts in the acquired UTE images. Nonetheless, CT images present streak artefacts near the metal implants, Figure 4.2.

The first observation is important for the derivation of an attenuation map. If the local MR intensities of the UTE images were affected by metal implants a segmentation method based only on the MR intensities would possibly fail in the classification of the surrounding tissues of the metal implants, introducing artefacts in the AC map and consequently

it would affect the reconstructed PET image.

The second observation however is indirectly also important for the derivation of an attenuation map. The AC methods that optimize their parameters based on a reference image (in this case the CT) will not converge to the best parameters if this reference image is incorrect; consequently the AC map will not be optimized. In the specific case if the CT image present streak artefacts, tissues surrounding the metal implant will present wrong CT units and therefore wrong attenuation values. In this case as this influence only the optimization of the parameters of autonomous methods one possible solution would be to discard the region where streak artefacts occur and use the remain image for parameter optimization.

4.4.3 Motion artefacts

On the contrary to metal artefacts, motion artefacts affected the MR images, Figure 4.3. It was observed that the data available were largely affected by motion artefacts (5 of 8 subjects). This poses a huge problem in the derivation of an AC map for any method that uses MR intensities of the corrupted image. As the image is distorted, the spatial relation between both UTE images is lost for the region where motion occurred. One possible solution to this problem would be to sedate the subject or immobilize his/her head during the exam.

One additional observation is that the UTE2 was the image that presented the most artefacts. Therefore one possible solution that should be explored is to image with a different TE for the UTE2 [Keereman et al., 2010]), or use additional echoes [Berker et al., 2012].

4.4.4 Intensity inhomogeneity artefacts

As it was shown IH are also present in the UTE images, Figure 4.4. Depending on the their magnitude, this can pose a problem to the derivation of an AC map. Analytical methods such as the ones proposed by [Catana et al., 2010, Keereman et al., 2010] assume that only bone intensity increases from the UTE1 to the UTE2. Therefore, a subtraction between UTE1 and UTE2 is normally the core of bone classification in both methods, Equation 3.7. As can be seen in Figure 4.4 3^{rd} column near the frontal sinus and occipital region, soft tissue presents similar intensities as bone and therefore analytical methods such as [Catana et al., 2010, Keereman et al., 2010] are prone to errors if IH artefacts are not corrected. One possible solution to this problem would be to inspect the MR scanner for IH artefacts with a homogeneous phantom (as it

was presented in Figure 4.6 and 4.5) that covers the FOV of the 3T MR/BrainPET scanner and deriving a calibration factor to be used in the subjects' images. Note, however, that due to problems as, e.g., when the volume inside the MR scanner is too large or too small this may give strange artefacts. Also, this solution does not account for subjects' dependent IH. Moreover, regular calibrations need to be performed as the scanner inhomogeneities change over time. Another solution would be to post-processing the MR images to correct for IH before being used in the generation of AC maps. Some methods have been developed and were reported in chapter 2 section 2.2.4. However, most of these methods focus on IH correction of brain tissue and are therefore not useful for correcting MR images for AC map estimation when bone has to be considered as an important tissue.

4.5 Conclusion

In this chapter the major problems to AC map estimation and analysis were identified being CT/MR co-registration, metal, motion and IH artefacts.

In AC map estimation CT/MR co-registration artefacts and metal artefacts majority affect autonomous methods that use a reference image for parameter optimization. One possible solution would be to remove these artefacts from the parameter optimization step. Motion artefacts, however, cannot be ignored as they influence the MR data and will consequently influence the AC map estimation and finally the PET reconstructed image. Solutions were presented such as sedation or immobilization of the subject during the exam. IH artefacts also influence the MR data and depending on the magnitude of the inhomogeneities can influence the AC map estimation and the PET reconstructed data. Methods that try to correct the hardware-dependent IH are useful, however they have some limitations: bias field is not only dependent from the hardware but also from the subjects and therefore methods that are based solely on hardware-dependent correction may fail to accurately estimate the bias for different subjects. Post-processing methods have the advantage of correcting not only the scanner-dependent inhomogeneities but also the subject-dependent inhomogeneities. However most methods are focused on brain tissues and ignore some important tissues for AC map estimation such as bone.

In AC map analysis CT/MR co-registration artefacts and metal artefacts will wrongly estimate local and global errors in the generated AC map. One possible solution would be to use head immobilization device in both CT and MR scanners.

Chapter 5

Bias field correction

5.1 Introduction

In the last chapter the main artefacts that influence the AC map estimation were analyzed. A simple solution was given to both CT/MR co-registration and metal artefact. Additionally, motion artefacts were analyzed and their influence in AC map estimation was discussed. An immediate solution was not possible and this error was bypassed. Moreover, the influence of IH in AC map estimation was discussed and some suggestions were given to reduce these artefacts.

The use of prospective methods for IH correction can be difficult as IH in MRI can appear due to different factors such as imperfections in RF coils, problems in the acquisition sequence or subject's anatomy [Belaroussi et al., 2006].

Some retrospective methods try to correct inhomogeneities by joint segmentation with bias field estimation [Gispert et al., 2004], requiring some initializations that may not be easy to handled. Multispectral images have also been used, although most of them require the use of specific hardware [Lai and Fang, 2003] or subjective masks [Vovk et al., 2006].

In this work a method that corrects multiple images simultaneously without requiring any kind of specific hardware or masks is presented based on the minimization of the variation of information (VI). This work is an extension of the work presented by [Vovk et al., 2006].

5.2 Material and Methods

5.2.1 Data acquisition

Simulated data (T1-weighted, T2-weigthed and proton density (PD)) of a digital phantom obtained from the Brain-Web-MRI Simulator [Cocosco

et al., 1997] were acquired. The simulated images were obtained with 3% and 0% (unbiased image), 20% and 40% IH, Figure 5.1 (In annex B the full parameters used for simulation are shown). Noise is generated using a pseudo-random Gaussian noise field which is added to both the real and imaginary components before the final magnitude value of the simulated image is computed. The bias fields are estimated from real MRI scans, they are not linear and slowly-varying fields.

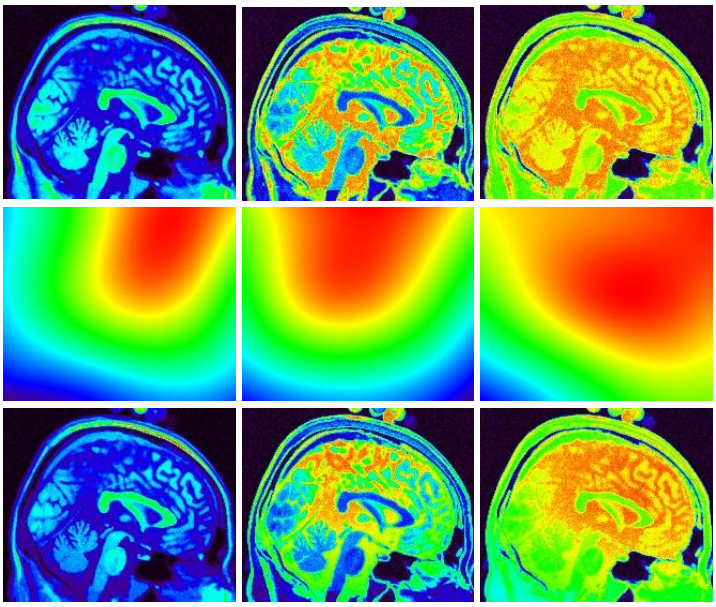

Figure 5.1: Illustration of the simulated data. In the first row T1 (left), T2 (middle) and Proton Density (PD) (right) images are shown corrupted with 3% noise. In the second row the bias field profile used is presented for each image of the first row. In the third row the same images as in the first row but additionally corrupted with 20% IH are presented.

These datasets were used to test and evaluate the proposed method. Additionally, the MR data acquired and described in previous chapters were bias corrected and the results analyzed.

5.2.2 Data processing

For the development of the bias correction method two conditions must be assumed: The corruption of multispectral MR images by IH is described by a multiplicative model, and by considering two images of the same dataset IH increase the amount of information contained in one image in respect with the amount of information in the second image.

The first condition states that IH are described by a multiplicative model, therefore the problem of IH correction is concerned with finding

the inverse of v_k, neglecting n_k, and therefore restoring the ideal image, Equation 4.1. The information needed for finding the inverse of v_k can be obtained from the image and can be improved if more than one image from the same subject is used for correction.

The second condition states that when two images are corrupted with IH the amount of information is lost or gained in changing from one image to the other one, Figure 5.2.Therefore, it is possible to estimate this bias field if the VI of both images can be calculated and minimized.

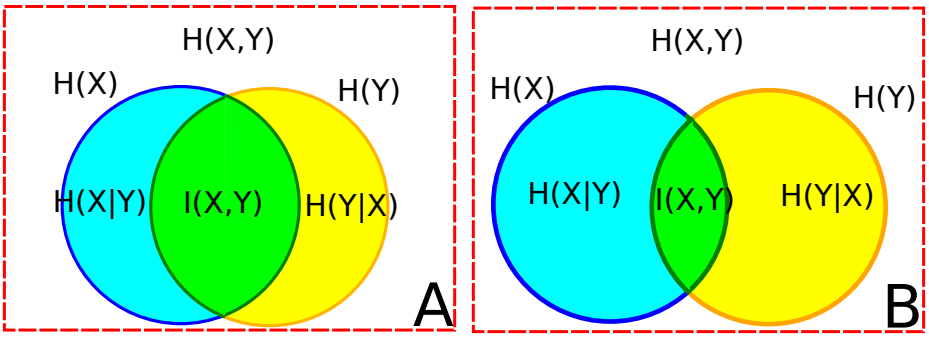

Figure 5.2: Influence of IH on a pair of images from the same subject. From A to B the mutual information of both images ($I(X,Y)$) decrease due to IH. Additionally the conditional entropies ($H(X \mid Y)$ and $H(Y \mid X)$) and the joint entropy ($H(X,Y)$) increase.

The proposed method reduces IH iteratively by minimizing the VI between two images.

Initially, a joint histogram (p(x,y)) of both images is performed, generating a feature space of both images. This histogram has, however, some particularity. Typical joint histograms are determined by first calculating the range of intensities of each image and dividing this range into N equal bins. Then an algorithm searches on the two images and count the number of voxels that fall into one of the NxN combinations. The proposed joint histogram instead of dividing the image range intensities into N equal bins, it divides the intensity range of each image into bins with inequal sizes maximizing tissue differentiation, Figure 5.3.

Then VI for each entrance in the feature space is calculated, based on the Joint Entropy (JE) and Mutual Information (MI) determined from the joint histogram, by Equation 5.4, Figure 5.4.

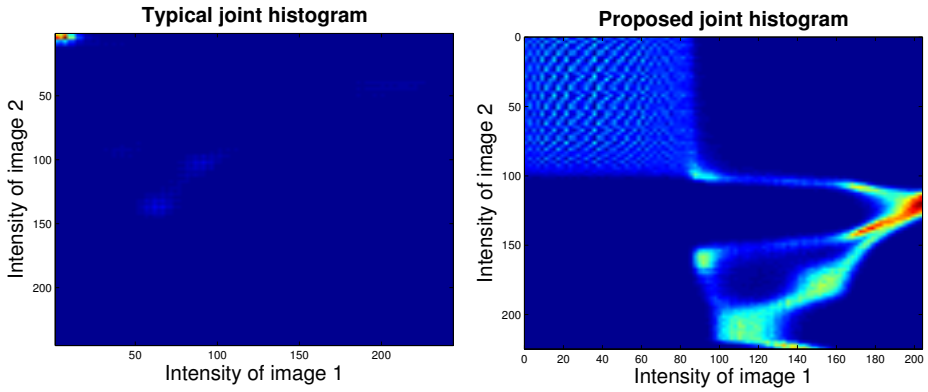

Figure 5.3: A typical joint histogram (left) between a T1 and T2 weighted image pair and the proposed joint histogram (right). Due to the presence of a large background a typical joint histogram shows a high intensity peak for the low intensities resulting in a low resolution for the rest of the matrix.

$$\begin{aligned} VI(x,y) &= JE(x,y) - MI(x,y) \\ &= -p(x,y) \times log(p(x,y)) - p(x,y) \times log\left(\frac{p(x,y)}{p(x) \times p(y)}\right) \\ &= -p(x,y) \times log\left(\frac{p(x,y)^2}{p(x) \times p(y)}\right) \end{aligned} \tag{5.1}$$

Next, the forces that minimize VI for each image are computed by the derivative of VI, Figure 5.5. The partial derivatives of VI were calculated with the Scharr operator which performs image convolution with a specific kernel, Table 5.1.

Table 5.1: Sharr operator (kernel) for calculation of partial derivatives.

(a) x derivative kernel.

-3	0	3
-10	0	10
-3	0	3

(b) y derivative kernel.

-3	-10	-3
0	0	0
-3	-10	-3

The calculated forces are mapped from the feature space to the image space, so that a bias field can be calculated, Figure 5.6 ($1^{st}row$). Such forces are, however, very noisy and therefore need to be smoothed to generate proper bias field estimation, Figure 5.6 ($2^{nd}row$). A Gaussian filter with 60mm radius was used for that propose. At this point one bias

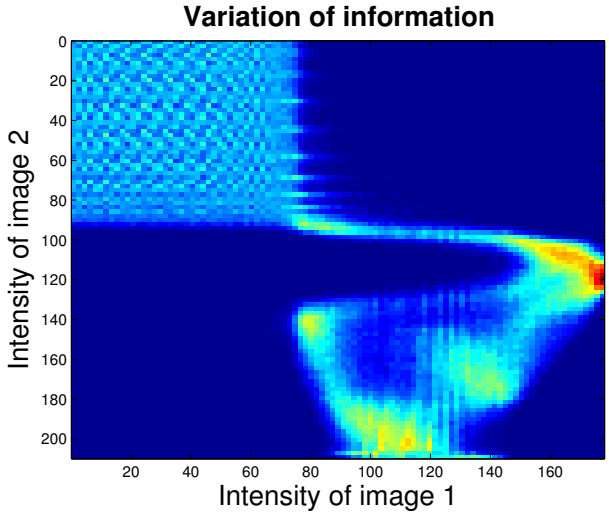

Figure 5.4: The derived variation of information from the proposed joint histogram between a T1 and a T2 weighted images.

field for each input image is generated and can be used for IH correction of the respective image.

Correction of IH is performed by the division of the measured image with the estimated bias field, $u_k = v_k/s_k$. The whole process is repeated a certain number of iterations, to obtain a better estimation of the bias field.

Summarizing the workflow of the full algorithm is as follows, Figure 5.7:

1. The original images (biased images) are used to derive the modified joint histogram;
2. The VI is calculated, Equation 5.4;
3. The forces that minimize VI are computed by the derivative of VI and mapped to each image;
4. The forces are smoothed to generate an incremental bias field estimation;
5. The total bias field estimation is updated;
6. Each image is corrected for IH and the modified joint histogram calculated;
7. Go from 2. to 6. until VI reached a minimum or the number of iterations is reached.

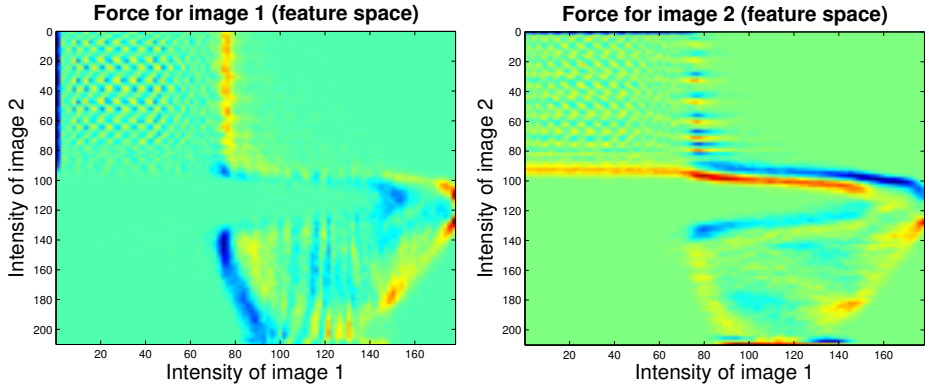

Figure 5.5: Representation the forces in the feature space that minimize VI for a T1 and T2 image pair.

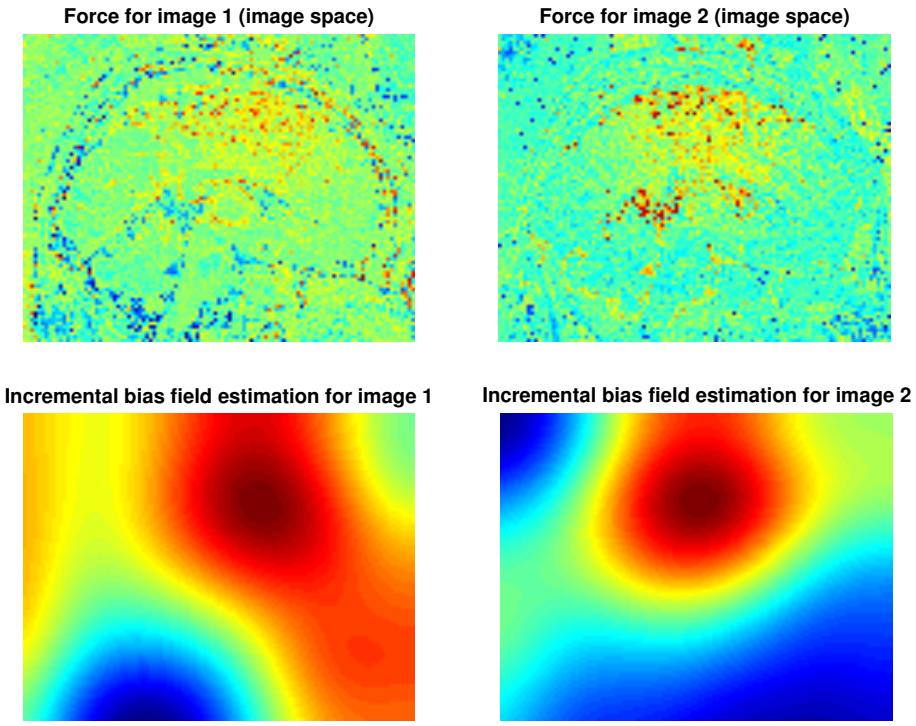

Figure 5.6: Representation of the forces in the image space that minimize VI for a T1 and T2 image pair (top) and the incremental bias field estimation derived by smoothing the forces for each image (bottom).

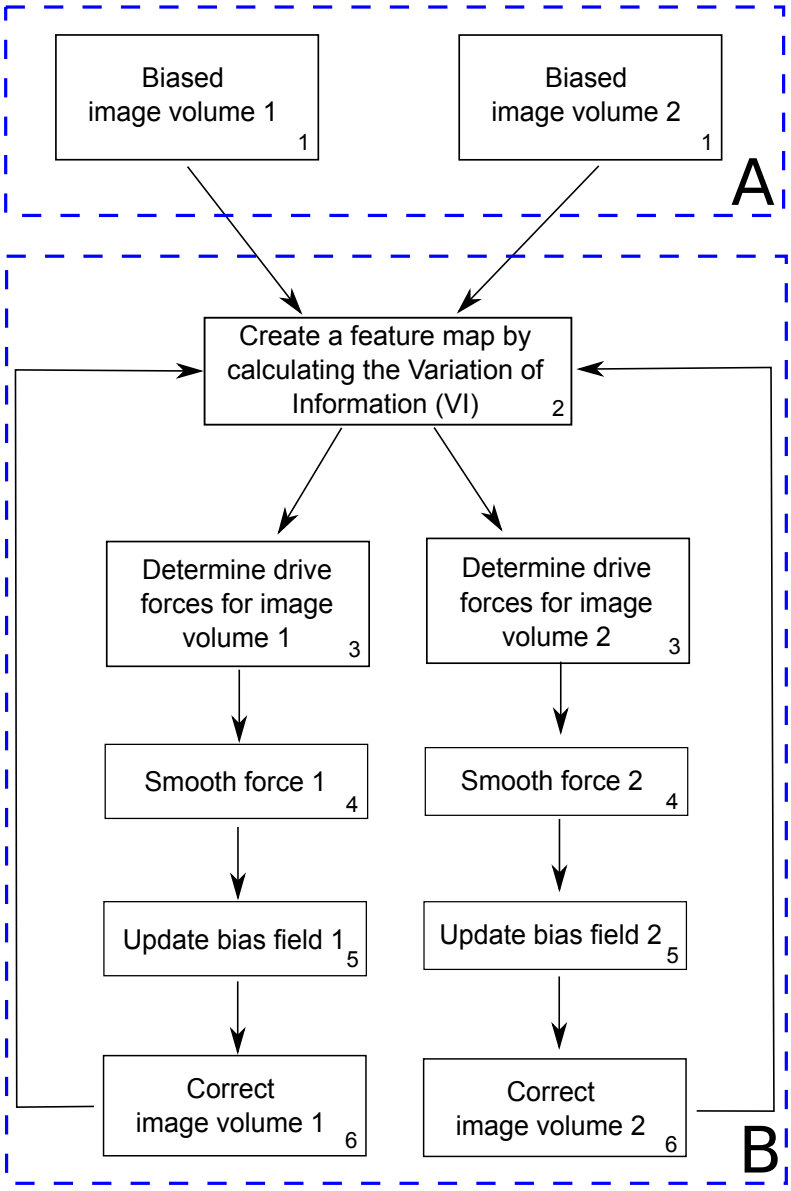

Figure 5.7: Workflow of the full methodology for bias correction of multiple images.

5.2.3 Data analysis

For the simulated images, pairs of images were used for correction of IH. The normalized coefficients of joint variation (nCJV), Equation 5.2 and 5.3, [Likar et al., 2001] were calculated between white mattter (WM) and gray matter (GM) and compared with the results for the same dataset presented in [Vovk et al., 2006]. This analysis has been applied largely in bias field evaluation [Gispert et al., 2004, Hou et al., 2006, Likar et al., 2001, Luo et al., 2005]

$$CJV = \frac{\sigma(T_1) + \sigma(T_2)}{|\mu(T_1) - \mu(T_2)|} \tag{5.2}$$

$$nCJV = \frac{CJV(real) - CJV(ideal)}{CJV(ideal)} \tag{5.3}$$

, where T_1 and T_2 are tissue 1 and tissue 2 respectively, and CJV(ideal) is the CJV calculated for the bias-free image and CJV(real) the CJV calculate before and after bias correction.

For the acquired MR data, as the final goal is improve the difference between the tissues of interest in AC map estimation, analysis of the resultant corrected data was performed in two ways: First a co-registered CT image was segmented into 3 tissues: air, bone and soft tissue, and each region used to calculate the Coefficient of Variation (CV), Equation 5.4, of each class: air, soft tissue and bone.

$$CV = \frac{\sigma(T)}{\mu(T)} \tag{5.4}$$

, where T is a single tissue class.

This analysis was chosen because real data are far away to be ideal data, thus making the calculation of nCJV unreliable. Additionally CJV is majorly used to evaluate IH correction methods in brain tissue (calculated from known white and gray matter classes) and not tissues such as bone. Moreover, CV for white and gray matter are also common analysis in bias field correction methods [Boyes et al., 2008, Dawant et al., 1993, Hou et al., 2006, Luo et al., 2005], while for bone is not. Second a simple segmentation method, Equation 5.5, was performed and optimized (TH1 and TH2 parameters optimization) for the MR data before and after bias correction.

$$\begin{cases} Air = UTE1 + UTE2 < TH1 \\ Bone = (UTE1 - UTE2 >= TH2) \wedge (\sim Air) \\ ST = (\sim Air) \wedge (\sim Bone) \end{cases} \tag{5.5}$$

, where TH1 and TH2 are two different intensity thesholds, $\sim$ refers to the operation NOT. For each subject the co-classification of voxels, Equation 5.6:

$$C_{class} = \sum(VOX_{CT} \bigcap VOX_{classified}) \tag{5.6}$$

and the dice coefficient values, Equation 5.7:

$$D_{value} = \frac{2 \times \sum(VOX_{CT} \bigcap VOX_{classified})}{\sum(VOX_{CT}) + \sum(VOX_{classified})} \tag{5.7}$$

between the generated image before and after bias correction with the respective CT image were obtained.

5.3 Results

5.3.1 Digital brain phantom analysis

The nCJVs of the simulated images for 150 iterations for all combinations of images are presented in Table 5.2.A decrease of the nCJVs values can be observed when going from unbiased (0%) to biased images (40%). Additionally, the results obtained by [Vovk et al., 2006] for the same dataset. Our method performs better in 6 of 12 comparisons, equals in 4 of 12 comparisons and worses in 2 of 12 comparisons.

Table 5.2: nCJV values for the simulated data. In parenthesis the nCJV values published by [Vovk et al., 2006] for the same datasets.

x	$T1_0\%$	$T1_{20}\%$	$T1_{40}\%$	$T2_0\%$	$T2_{20}\%$	$T2_{40}\%$	$PD_0\%$	$PD_{20}\%$	$PD_{40}\%$
$T1_0\%$	-	-	-	0 (1)	0	0	0 (1)	0	1
$T1_{20}\%$	-	-	-	0	0	0	0	0	0
$T1_{40}\%$	-	-	-	0	0	0 (0)	0	0	0 (-1)
$T2_0\%$	-1 (0)	-1	-2	-	-	-	-1 (0)	0	0
$T2_{20}\%$	-1	-1	-2	-	-	-	0	0	0
$T2_{40}\%$	0	-1	0 (-1)	-	-	-	-1	-1	0 (0)
$PD_0\%$	0 (1)	-2	-1	0 (2)	-1	-3	-	-	-
$PD_{20}\%$	0	-2	-3	1	-1	-3	-	-	-
$PD_{40}\%$	0	-2	-3 (-3)	1	-1	-2 (-2)	-	-	-

Furthermore, Figure 5.8 presents the bias estimation (2nd row) and correction (3rd row) of a $T1_{40}$ (1rst row)- $T2_{40}$ image pair) performed with the proposed method (left column) and obtained from simulated data (right column). By a visually comparison it seems that the method corrects most of the bias and the corrected image with the estimated bias field is visually close to the ideal simulated image. Despite the high visual similarity between the estimated and the simulated bias fields some differences can still be noted.

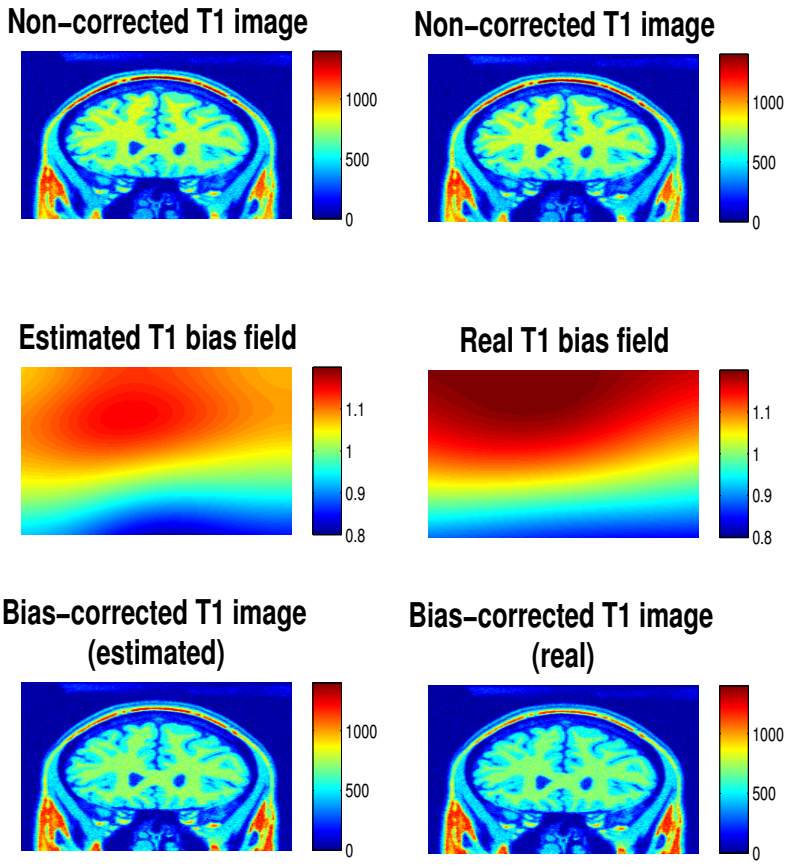

Figure 5.8: Estimation and correction of bias field in simulated images. On the left estimation and correction with the proposed method. On the right the original simulated bias field and with the respective correction.

5.3.2 Real data analysis

Table 5.3 shows the relative differences between the CV (rCV) before and after bias correction for all subjects. As can be seen the CV decreases after bias correction for all tissues and all subjects. Moreover,

the mean relative difference and standard deviation between the CV before and after bias correction was verified to be statistically significant with p=0.05.

Table 5.3: rCV before and after bias correction for 9 subjects for 3 different tissues: air, soft tissue (st) and bone.

subject	rCV_{air}	rCV_{st}	rCV_{bone}
1	0.02	0.06	0.08
2	0.04	0.04	0.04
3	0.09	0.13	0.15
4	0.06	0.01	0.03
5	0.04	0.04	0.03
6	0.08	0.07	0.06
7	0.05	0.04	0.05
8	0.06	0.07	0.07
9	0.15	0.09	0.06
mean±std	0.07±0.04	0.06±0.03	0.06±0.04

In Table 5.4 the optimized total dice coefficients (TH1 and TH2 were optimized to obtain the maximum total dice coefficients) for both biased and bias-corrected segmented images are shown. Additionally, the mean and standard deviation is presented. As one can see for all subjects the dice coefficients of the bias-corrected images are than those of the biased images when global TH1 and TH2 were applied to all subjects (fix. thres) and when TH1 and TH2 were adapted to each subject (adapt. thres.). Additionally, the resulting means dice coefficient of the bias-corrected images were verified to be statistically higher than those of the biased images with a significance value of 5%.

Figure 5.9 shows the classification of the optimized total dice coefficients (fix. thres.) for both the biased and bias-corrected images for 1 subject. As can be seen the biased segmentation presents an over-classification of the bone in the occipital region and near the frontal sinus, which disappears after bias correction.

Table 5.4: Total dice coefficients obtained for a biased (Biased D_{coef}) and bias-corrected ($Bias_{corr}$ D_{coef}) images when fixed thresholds (fix. thres.) or adapted threshold (adapt. thres.) for each subject were used.

subject	Biased D_{coef} (adapt. thres.)	$Bias_{corr}$ D_{coef} (adapt. thres.)	Biased D_{coef} (fix. thres.)	$Bias_{corr}$ D_{coef} (fix. thres.)
1	0.7767	0.8083	0.7752	0.8070
2	0.7620	0.7987	0.7613	0.7987
3	0.7724	0.7885	0.7577	0.7693
4	0.7743	0.8020	0.7498	0.7840
5	0.7834	0.8261	0.7827	0.8261
6	0.7593	0.7593	0.7317	0.7339
7	0.8091	0.8277	0.8072	0.8269
8	0.7378	0.7685	0.7364	0.7685
9	0.7580	0.8023	0.7571	0.7874
Mean	0.7703	0.7979	0.7621	0.7891

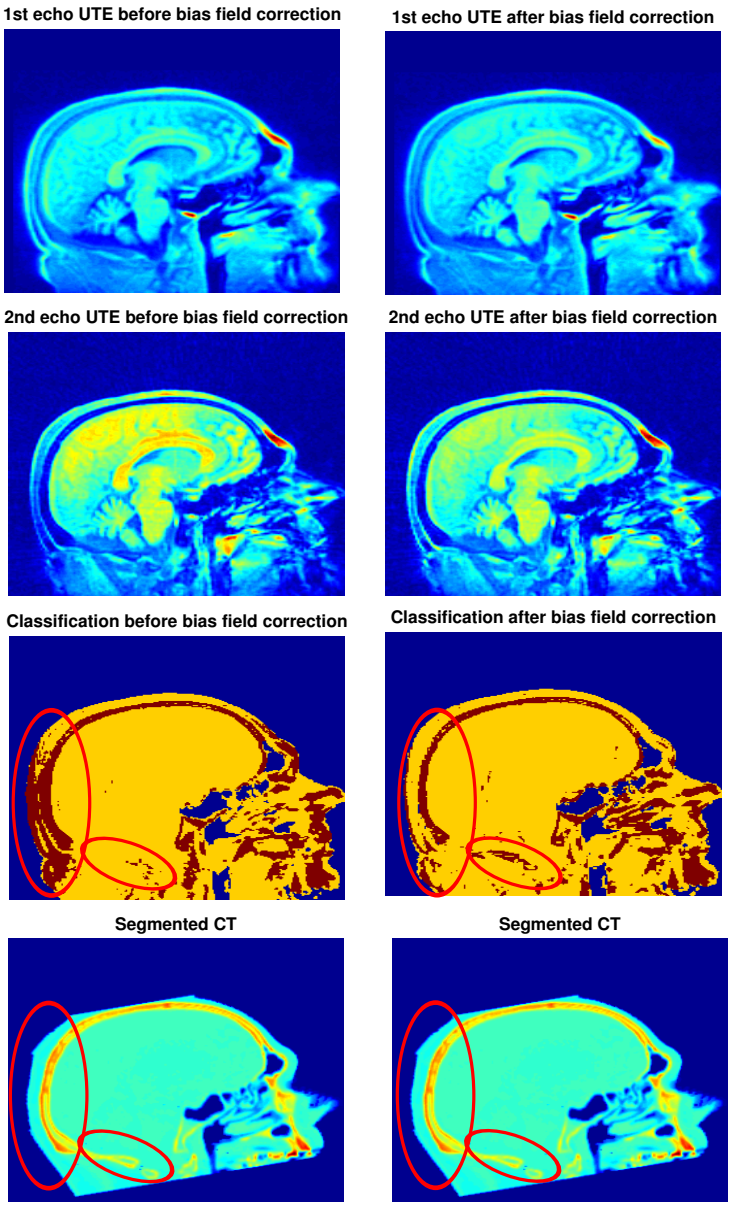

Figure 5.9: Classification of the optimized total dice coefficients for both biased (left) and bias-corrected (right) images for 1 subject. First row: UTE1 image; Second row: UTE2 image; Third row: Classification in three tissues by the proposed method; Fourth row: CT image coregistered to subject MR. Red ellipses represent regions where a large improvement in the bias-corrected segmented image with regard to bone and soft tissue is visible relatively to the biased segmented image.

5.4 Discussion

5.4.1 Digital brain phantom analysis

From Table 5.2 it can be seen that the proposed method reduces IH in corrupted images, while maintaining (until a certain degree) the non-corrupted images. The reduction was drastic and approaches values near 0 (bias-free images). The method however tend to over-compensates bias field effects and a stop condition not based on the number of iterations must be used to avoid severe artefacts.

Moreover, Table 5.2 compares the method proposed to the ones published in [Vovk et al., 2006] for the same database and analysis. It can be seen that in overall the proposed method improves accuracy relatively to [Vovk et al., 2006] without the definition of a background mask. This is an important point as a definition of a background image for different subjects is not always possible.

Nevertheless, the method showed differences to the simulated bias field, Figure 5.8. One of the major problems is that background is mainly random noise having few to no information regarding bias field without contributing to the bias field estimation. Therefore, the estimation of the bias field outside of the phantom would result highly complex and it will indirectly lead to global failures in the estimation of the bias field.

5.4.2 Real data analysis

In Table 5.3 the relative differences between the CV of biased and bias-corrected images are shown. The CV values decrease after bias correction for all subjects indicating higher homogeneity for the relevant tissues. This is important as the methods developed in this work are based on the voxel intensities of both UTE images, and higher homogeneity tends to improve tissue classification.

In Table 5.4 the best dice coefficient for each subject with adapted TH1 and TH2 values and with a general TH1-TH2 pair was shown. For both cases the values for the bias-corrected image showed to be significantly higher than those for the biased image. Thus the bias-corrected images should be preferred to be used for AC map estimation with more complex classification methods.

In Figure 5.9 the classification of MR data into the three tissues air, soft tissue and bone before and after bias correction of the MR data was compared. When the MR data were not corrected an over-classification of bone tissue in the occipital region as well as in the frontal sinus was observed. A bias correction showed to improve bone to soft tissue classification. This is mainly due to the huge bias field that affects both

UTE images in both regions. In fact it was already showed in Figure 4.4 that bias inhomogeneities in these regions could affect the classification as being the intensities of soft tissue and bone on the UTE difference image similar.

5.5 Conclusion

Our results on both simulated and real data suggest that the proposed bias correction method reduces IH without the use of specific hardware or subjective masks.

Additionally, higher homogeneities and better classified images were obtained when bias correction was performed. The results therefore suggest that bias field correction should be regularly applied to MR UTE images to improve tissues homogeneity and consequently tissue classification and AC map estimation.

Nevertheless, the results also showed that the proposed bias field algorithm tend to overcompensate bias field effect. One possible solution to explore would be to use a stop condition other than the number of iteration, to stop the algorithm before it over-compensates bias field effect.

Additionally, if a correction of a biased and an unbiased image pair (such as a $T1_0$ - $T2_{40}$ pair) is performed and it is known that one of the images is bias free (or with very low IH), the method should be changed to only perform bias field correction to the biased image, leaving the other image untouched.

Finally, implementation of published bias correction methods and comparison of both simulated and real data with the proposed method should be performed to truly determine if the method offers advantages over current bias correction methods.

Chapter 6

ANN approach for AC map estimation

6.1 Introduction

Artificial neural networks (ANN) are computational methods that try to study and mimic the way that the human brain works. These methods proved to be of extreme importance, being able to execute different tasks that require artificial intelligence, such as, associative memory, diagnostic, pattern recognition, prediction or regression, control, optimizing processes and signal processing. They have applications in medicine, engineering, and economy. Additionally, neural networks have proven to be accurate and general classifiers, without the need of high user interaction and expertise.

Indeed, as it was explained in chapter 3 section 4.3 that the limitations of current AC methods are that anatomical information provided from atlas or template images, or optimization of some parameters that are subjective and hard to define are needed for a good estimation of the attenuation map.

This way, three ANN approaches are studied in this section: a Self-Organizing Map (SOM) network, a feed-forward neural network (FFNN) and a probabilistic neural network (PNN). These three ANNs were chosen due to their specific advantages over other methods.

First, SOM networks are a type of ANN that are trained using unsupervised learning to produce a low-dimensional, discrete representation of the input space of the training samples. SOMs reduce complexity of the system by producing a map of usually 1 or 2 dimensions which plot the similarities of the data by grouping similar data together. Thus, SOM tries to learn the underling pattern from the inputs and output a labelled image without manual intervention. This network, therefore reduces the

problem of defining subjective parameters and creates a relations between the inputs without requiring user interaction. Unsupervised methods have however the disadvantage of clustering data in some ways that may not be intended. Easier optimization from supervised algorithms such as FFNN and PNN make these methods also good candidates for classification purposes.

FFNN such as SOM networks have one important property that is its capacity of learning. This learning is made with a learning algorithm, which updates the connection weights between nodes in accordance with a certain stimulus, changing the internal structure of the network, similar to SOM networks. As result, this will respond in a new way to the stimulus. However in FFNN, supervised learning is used, meaning that the desired outputs and respective inputs are known. The network learns by comparing the desired output with the network's output, calculating the difference and driving the network so that in each iteration this difference is minimized. The learning process ends when the error is lower than a threshold defined by the user or when a maximum number of iterations is reached. FFNN as well as other supervised learning techniques have also their disadvantages. FFNN specifically need large amount of data to classify accurately and generalize to different data. Additionally, FFNN for classification purposes require labelled data for the network to learn, and this may not be easy to obtain.

PNN is as well as FFNN a supervised learning algorithm. However, the learning step of PNN is done in a simple and single step. PNN do not requires large amount of data and classify accurately and generalize easily for different data. Nonetheless, it is the proposed network that requires the most user interaction and is the slowest network implemented.

6.2 Material and Methods

6.2.1 Data acquisition and pre-processing

The data used in AC map estimation was acquired and pre-processed as it was explained in chapter 4.

Before training and classification by the implemented methods, IH correction was applied to the MR-UTE images by the proposed method explained in chapter 5. The corrected images for IH were then used for training and classification of the implemented methods: FFNN, PNN and SOM. Additionally, the methods proposed by Keereman and Catana (segmentation of UTE images), and the method proposed by Rota Kops (using templates) were implemented and compared against the developed methods.

6.2.2 AC map estimation algorithms

6.2.2.1 Feed-Forward Neural Networks

6.2.2.1.1 FFNN architecture Feed-forward networks are characterized by the unidirectionality of its connections and can be convergent or divergent in respect of the connection, or mono layer or multi-layer in respect to the number of layer it has. Mono layer networks present only two layers: one input layer (IL) and one output layer (OL), and multi-layer three or more layers: one IL, one OL, and one or more hidden layers (HL). The multi-layer networks can model more complex functions than the mono layer, yet one of the disadvantages is that the learning time increases exponentially with the number of HL.

The proposed FFNN used in this work consists of a multi-layer network with 3 layers Figure 6.1. Our aim with this network is to define 3 different tissues: air, bone, csf+brain+soft tissues. Thus, the OL contains 3 nodes corresponding to these 3 classes. The HL contains 6 nodes, determined empirically as the minimum number of nodes for a good classification. The IL, representing the input features, feeds the FFNN.

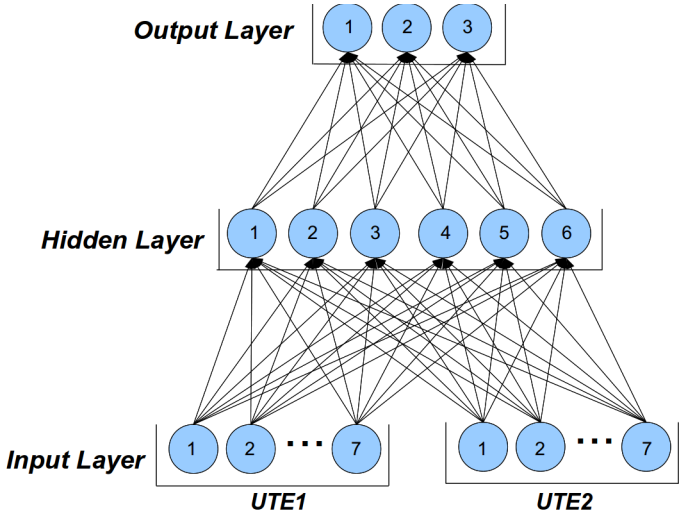

Figure 6.1: Architecture of the proposed FFNN algorithm. FFNN has 3 layers (IL, HL, and OL) with 7 input nodes from UTE1 and 7 input nodes from UTE2 in IL, 6 hidden nodes and 3 output nodes in OL.

6.2.2.1.2 FFNN procedure In this study the input features consist of two patches of MR intensities around a voxel of interest (VxOI) together with the 6 closest neighbours chosen in both the co-registered UTE1 and UTE2 images. The two obtained patches are stored in a vector that will be used in both training and classification steps.

In the training step Ni=10000 training vectors obtained from a training dataset and the corresponding labelled class obtained from the segmentation of a CT image into 3 regions (air, bone, soft tissues) and manual segmentation of the csf from the MR image was created.

In the FFNN an artificial neuron (or node, is the basic unit of processing to the function of an ANN) combines the weights (w), inputs (x) and bias (θ) by a linear combination of these, Equation 6.1, Figure 6.2.

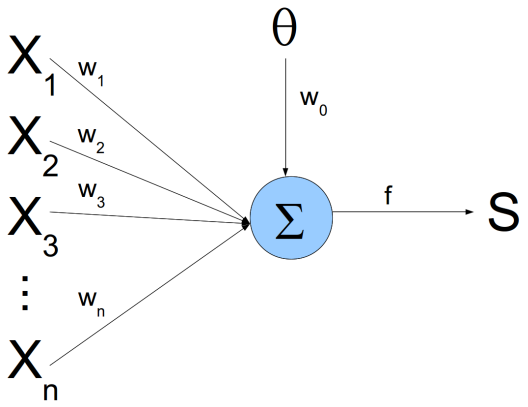

Figure 6.2: Artificial neuron. X_n are inputs to the ANN, w_n are the ANN weights, θ the bias, S the ANN output modelled by the function f.

$$u = \sum_{i=1}^{n} w_i \times x_i + w_0 \times \theta \tag{6.1}$$

If the output of the node was only a linear combination of the inputs, then only linear classification problems could be solved. To make the network capable of classifying non-linear problems the node must be modelled by an activation function such as a sigmoid function, Equation 6.2.

$$S = \frac{1}{1 + e^{-ku}} \tag{6.2}$$

where S is the output of the network.

For the determination of the output of the network in respect to a certain input vector, a forward process is implemented. The network calculates the output of each node by Equation 6.1 and Equation 6.2. The output of the network is compared with the desired output and the resulting error calculated, Equation 6.3.

$$E_{OL} = D_{OL} - O_{OL} \tag{6.3}$$

For the update of the network a backward process is implemented. The error of the FFNN is retro-propagate to the OL, Equation 6.4 and the HL, Equation 6.5 by optimization of the gradient descendent method.

$$E_k = S_k(1 - S_k)(T_k - S_k) \tag{6.4}$$

$$E_h = S_h(1 - S_h) \sum_{h+1=1}^{M} w_{h+1,h} E_{h+1} \tag{6.5}$$

S_k is the output of the node k of the output layer, T_k the desired output, E_k the error of each output node, S_h the output of the hidden layer node h, $w_{h+1,h}$ the weights that connect one hidden layer to the next, E_h the error of each node of the hidden layer h, and E_{h+1} the error of the next hidden layer. The indices M of the sum in the number of nodes of the layer h+1. The outputs of each node are modelled by a sigmoidal activation function.

Finally the weights connecting adjacent layers of the ANN are updated by Equation 6.6.

$$w_{ij}(t + 1) = w_{ij}(t) + \alpha E_i S_i \tag{6.6}$$

where w_{ij} is the connection between nodes i and j of different layers, α is the update factor, E_i the error associated to the weight, S_i the output of node i.

In summary, the method consists in:

- Training step:
    1. Selecting patches from both co-registered UTE images or from both co-registered UTE images and the template image derived by Rota Kops, to be used as training vectors;
    2. The weights are initialized with random values;
    3. The output of the nodes in HL and OL are determined by Equation 6.1 modelled by a sigmoid activation function Equation 6.2);
    4. The desired output calculated and the error of the output layer determined;
    5. The error propagated from the output nodes to the input nodes, backwards (Equation 6.4 and Equation 6.5);
    6. The weights updated by Equation 6.6;
    7. Total error calculated and compared with the threshold defined.

8. Go from 3. to 7. until the total error is lower than the threshold defined. Finish otherwise.

- Classification step:

1. Calculate one segmenting vector from the image to be classified;
2. The output of the nodes in HL and OL are determined by Equation 6.1 modelled by a sigmoid activation function Equation 6.2);
3. Determine the node in OL with the highest probability and assign that class to the central voxel;
4. Go from 1. to 3. until all voxels in the image have been classified. Finish otherwise.

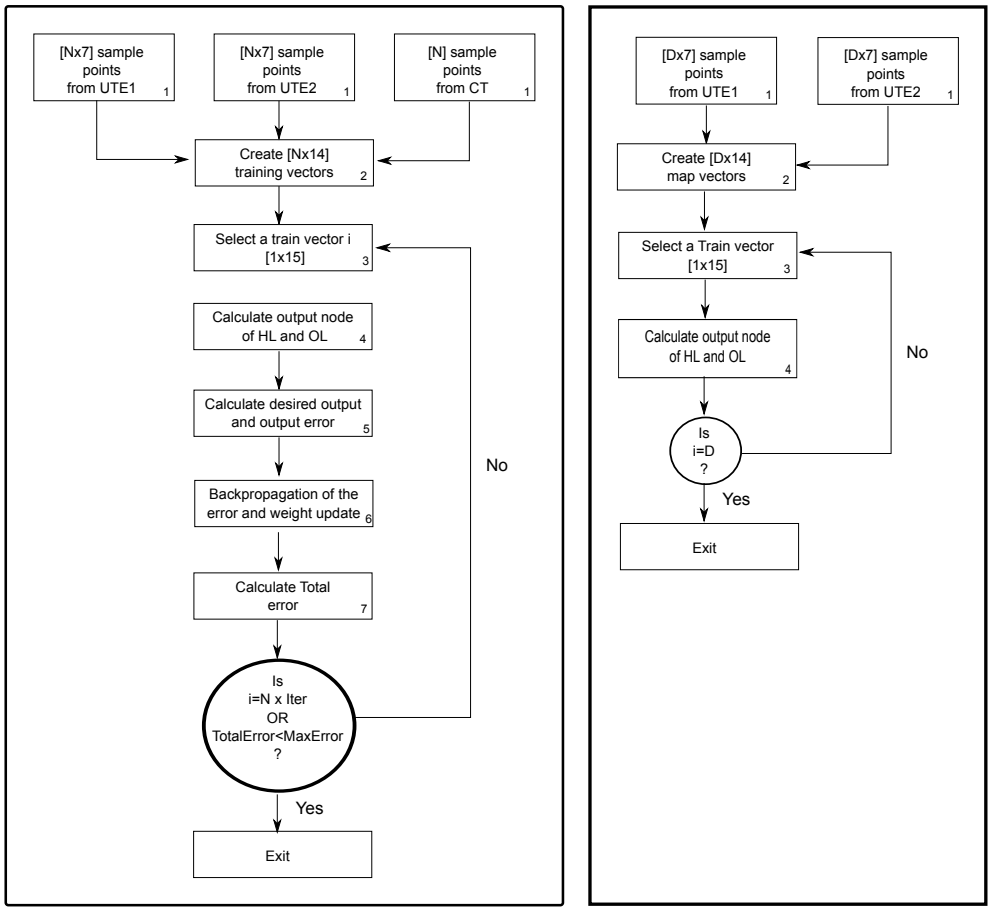

Figure 6.3: Scheme showing the FFNN algorithm implemented. The algorithm consists in 2 phases: a learning step and a classification step. N samples from both UTE images and the CT (1) are used to create a train vector (2). For each element of the training vector (3) the output of the HL and OL are calculated (4). The network output is compared to the desired output and the error calculated (5). This error is used to correct the weights of all nodes by back-propagation. After each element of the training vector has been used to update the net weights the total error of the network is calculated and if less than the minimum accepted the algorithm stops. Otherwise, the algorithm updates the net weights again for all training elements.

6.2.2.2 Probabilistic neural network

6.2.2.2.1 PNN architecture PNN consists of a feed-forward neural network with 3 layers shown in Figure 6.5: an input layer (IL), a pattern layer (PL), and a summation layer (SL). Our aim is to obtain 4 distinct classes: brain+soft tissue, csf, bone, and air. 4 tissues instead of only 3 were chose for the PNN algorithm as it was verified to perform better. Thus, the SL consists of 4 nodes corresponding to these 4 different classes. The PL consists of 4 pools, each corresponding to the 4 nodes of SL and each being built up of previously chosen training data of the corresponding classes to be segmented. The IL, representing the input features, feeds PNN.

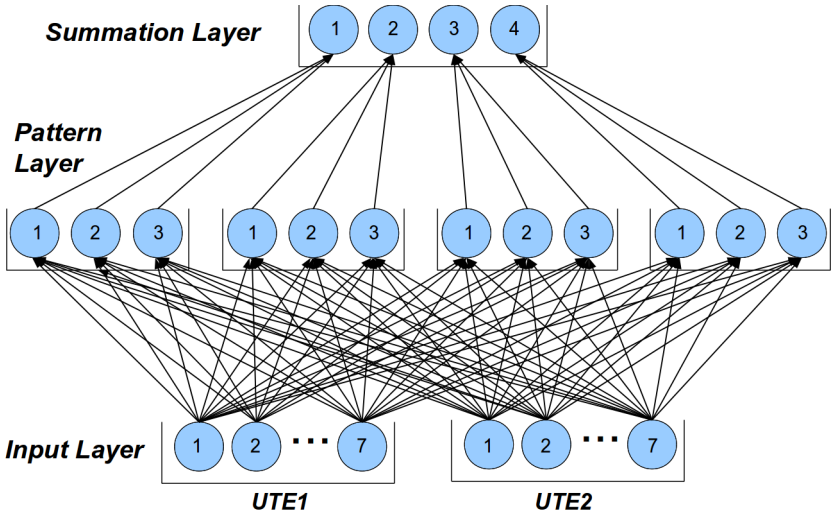

Figure 6.4: Architecture of the proposed PNN algorithm using only UTE1 and UTE2. PNN has 3 layers (SL, PL, and IL) with 7 input nodes from UTE1 and 7 input nodes from UTE2 in IL, 4 poles of 3 pattern nodes in PL, and 4 output nodes in SL.

6.2.2.2.2 PNN procedure In this study the input features consist of two patches of MR intensities around a voxel of interest (VxOI) together with the 6 closest neighbours chosen in both the co-registered UTE1 and UTE2 images. The two obtained patches are stored in a vector that will be used in both training and classification steps.

In the training step $Ni = 3$ example vectors (or training vectors) obtained from a training data set are stored for each class (Ci) to be classified and are given to the corresponding nodes in PL.

In the classification step the vectors to be classified (segmenting vector) is obtained for every voxel (VxOI) and is given to the nodes in IL.

The output of the nodes in PL is calculated based on the combination of a radial basis function (RBF) with a Gaussian activation function and is given by equation 6.7:

$$Oi_{PL} = exp\left(\frac{-|x - Ti|^2}{2\sigma^2}\right) \tag{6.7}$$

where Oi_{PL} is the output of each node in PL, x is the segmenting vector in IL, Ti is the training vector in PL and, sigma (σ) the smoothing factor.

The output of the nodes in SL (segmented classes) calculated by a weighted summation of the nodes in PL that are connect to each of them is thus obtained by equation 6.8:

$$p(x|Ci) = \frac{1}{Ni(2\pi)^{d/2}\sigma^d} \sum_{n=1}^{Ni} Oi_{PL} \tag{6.8}$$

where $p(x|Ci)$ is the probability density function of class Ci and d the dimension of the input vector.

For each input feature in IL, PNN calculates the probability to be a member of one of the 4 different classes and assigns the current VxOI to the class with the highest probability.

In summary, the method consists in:

- Training step:
    1. Selecting patches from both co-registered UTE images or from both co-registered UTE images and the template image derived by Rota Kops by user-expert, to be used as training vectors;
- Classification step:
    1. Calculate one segmenting vector from the image to be classified;
    2. Calculate the output of each one in PL by Equation 6.7;
    3. Calculate the output of the nodes in SL by Equation 6.8;
    4. Determine the node in SL with the highest probability and assign that class to the central voxel;
    5. Go from 1. to 4. until all voxels in the image have been classified. Finish otherwise.

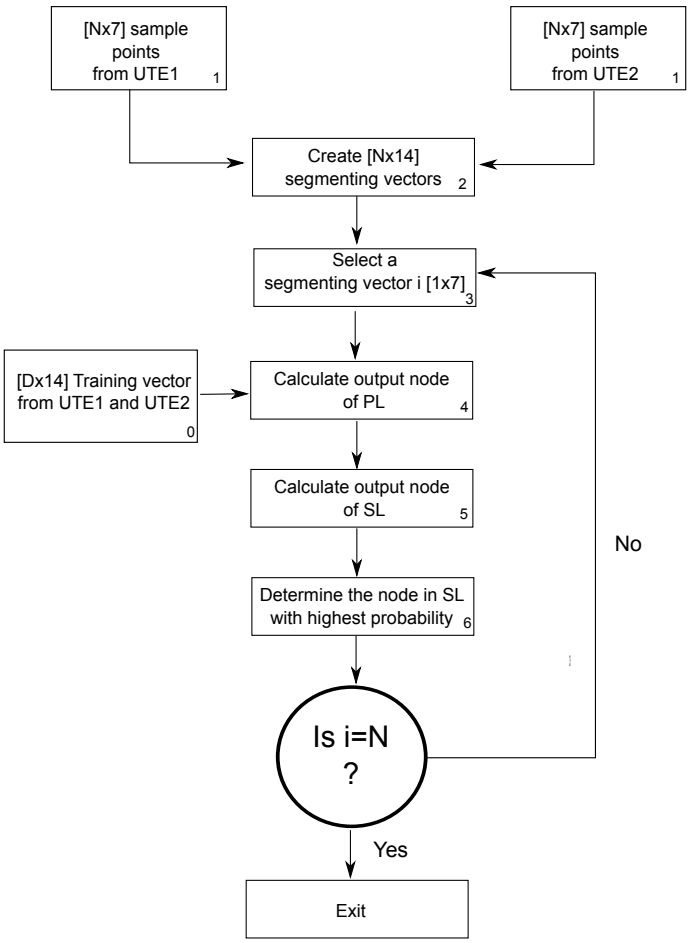

Figure 6.5: Scheme showing the PNN algorithm implemented using only UTE1 and UTE2. As this algorithm does not really have a learning step only the classification step is considered. First N sample vectors obtained from the N voxels to be segmented of UTE1 and UTE2 (1) are used to create a Nx14 segmenting vector (2). A segmenting vector i is chosen (3) and with the training vectors (0) the output of PL (4) and SL (5) calculated. The node in SL that presents the highest probability is chosen and the respective tissue determined (6). When all voxels have been segmented the program end.

6.2.2.3 Self-Organizing Feature Map

6.2.2.3.1 SOM architecture SOM, also called Kohonen map, consists of a 2-D grid of nodes, Figure 6.6. Each node in the 2-D lattice topology is associated with a reference vector corresponding to an input. For this network a 10x10 matrix was defined, therefore the inputs to the network will be clustered into 100 different classes. The characteristic that distinguishes the SOM net from the other classification algorithms is that in SOM similar inputs are associated not only to the same cell, but also neighbourhood cells contain similar information. This way, the nodes in the 2D matrix are connected not only to the input features but also to the neighbour nodes.

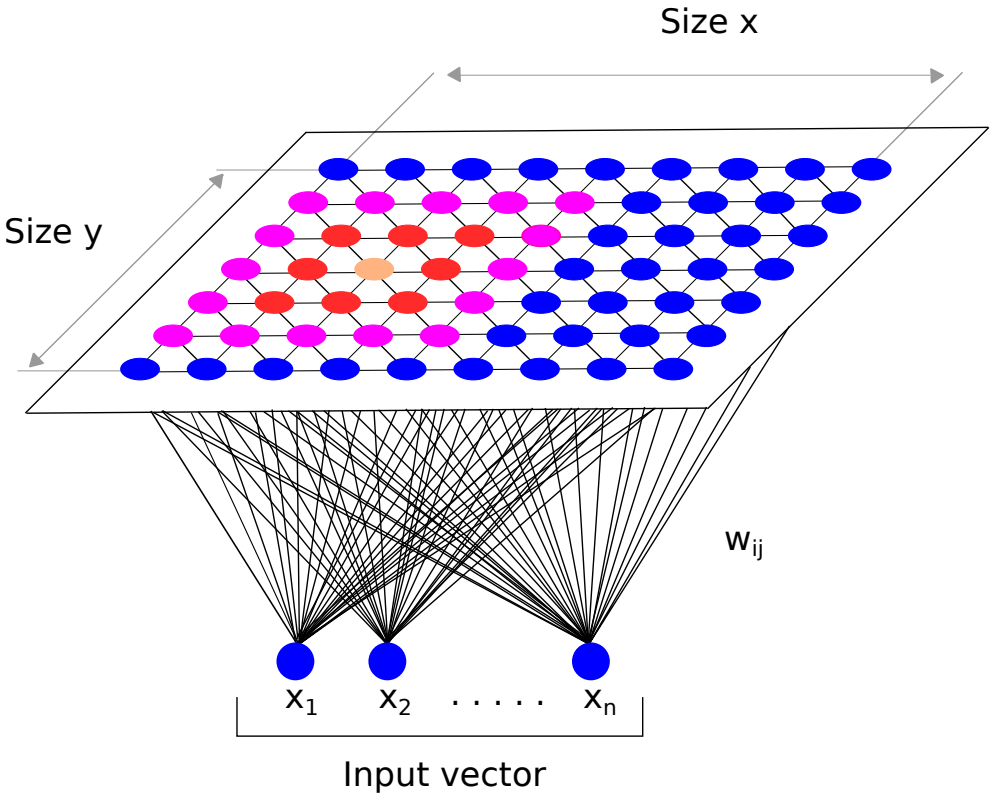

Figure 6.6: Architecture of the proposed SOM algorithm. The SOM has a 10 x 10 matrix of neurons.

6.2.2.3.2 SOM procedure SOM algorithms for segmentation work in two phases: In the first phase SOM adapt its neurons so in each iteration they are closer to the input data, and group similar data together After a number of iterations the SOM is fully trained and can be used to distinguish different inputs (such as different tissues in a MR image).

In the first phase (training phase) corresponding voxels from the two UTE images, the template image derived by Rota Kops and a CT image are given to the algorithm to create a map that is later used for segmentation. In the second phase (mapping phase) the map created in the train phase is applied onto each voxel of the UTE1 and UTE2 images to differentiate between different classes.

In the training phase a matrix containing N train vectors (with N=10000) is first created in which each train vector contains a central voxel of interest and the 6 surrounding neighbours from each UTE image and a respective attenuation value for the central voxel obtained from a CT image (performing a total of 15 samples points for each train vector). Next, each train vector is given to the train algorithm and mapped in a square $M \times M$ matrix (with M=10) of weights. The goal is to train the net so that nearby outputs (from the square $M \times M$ matrix) correspond to nearby inputs, and so to create a topological map. For this, the training phase consists in selecting the reference vector to which the Euclidean distance with the train vector is minimum as the winner node, Equation 6.9.

$$\|x_k(t) - w_c(t)\| \leq \|x_k(t) - w_j(t)\| \qquad \forall\, j \tag{6.9}$$

where x_k is the train vector, w_c the winner node, w_j the reference vector. The winner node and the neighbourhood updated by Equation 6.10.

$$w_j(t+1) = w_j(t) + \alpha(t)\eta_{ci}(t)(x_k(t) - w_j(t)) \tag{6.10}$$

where $\alpha(t)$ is the learning rate (defined by Equation 6.11) and $\eta_{ci}(t)$ the neighbourhood kernel (defined by Equation 6.12).

$$\alpha(t) = \alpha(0)exp(\frac{-t}{n}) \tag{6.11}$$

$$\eta_{ci}(t) = exp(\frac{\|d_{ci}\|^2}{2\sigma^2(t)}) \tag{6.12}$$

In the mapping phase, each central voxel of the UTE1 and UTE2 images as well as the nearest 6 neighbours from each image (named map vectors) are given to the algorithm to be mapped. Mapping means to discover the closest node, Equation 6.9, of the $M \times M$ matrix of weights to each map vector. The attenuation value for the closest node can therefore be obtained by the topological map and used as the attenuation value for the central voxel.

A scheme showing the methodology of the whole algorithm can be seen in Figure 6.7).

In summary, the method consists in:

- Training step:

    1. Selecting patches from both co-registered UTE images, to be used as training vectors;
    2. Map a training vector to the MxM matrix (calculate the winner node) by Equation 6.9;
    3. Update the winner node and the neighbourhood weights by Equation 6.10, Equation 6.11 and Equation 6.12;
    4. Go from 2. to 3. until the number of iteration reach the maximum allowed. Finish otherwise.

- Classification step:

    1. Calculate one segmenting vector from the image to be classified;
    2. Map the segmenting vector to the MxM matrix (calculate the winner node) by Equation 6.9;
    3. Obtain the attenuation value for the closest node and assign to the central voxel;
    4. Go from 1. to 3. until all voxels in the image have been classified. Finish otherwise.

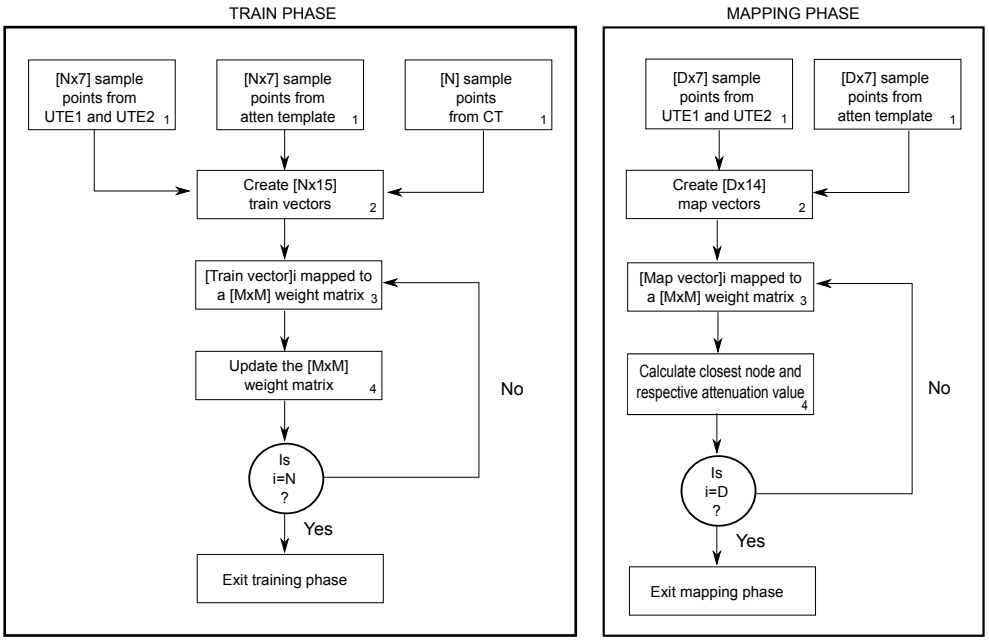

Figure 6.7: Scheme showing the SOM algorithm implemented. The algorithm is divided in two steps: A training phase and a mapping phase. The training phase comes first, where both samples from UTE1, UTE2, atten template and CT images (1) are used to create the train vectors (2). The train vectors are mapped to a [MxM] weight matrix (3) which is updated for each train vector (4). When all train vectors are feed to the algorithm the training phase ends (5). Next the mapping phase starts, where both samples from UTE1, UTE2 and atten template, corresponding to all voxels in the image (1), are used to create map vectors (2). The map vectors are mapped to the [MxM] weight matrix (3) and the closest node to each map vector is calculated (4). Additionally, at this step the attenuation value corresponding to the closest node is determined and assigned to the central voxel. When all map vectors are feed to the algorithm the mapping phase ends (5).

6.2.2.4 Keereman's and Catana's methods

As it was explained in chapter 3 Keereman's algorithm is implemented by obtaining the R2 map from the UTE1 and UTE2 volumes by Equation 3.7. Then, an air mask is generated from UTE1 by first separating the background from the image by region growing. To accomplish this the corners of the image volume are used as seeds to the region growing algorithm and a threshold (TH1) defined to distinguish if neighbour voxels belong as background voxels or image voxels. Additionally, a second threshold (TH2) need to be defined to separate voxels belonging to air that are not connected to the seed voxels. The correction of the R2 map is performed by multiplying the air mask to the obtained R2 map. The corrected R2 map is then segmented in bone and soft tissue by thresholding (TH3).

In Catana's method bone and air are segmented by a combination of both MR images. For bone tissue, the original UTE1 and UTE2 volumes are first divided by the corresponding smoothed volumes. The resulting datasets are combined by the transformation $(UTE1 - UTE2)/UTE2^2$ to enhance the bone tissue voxels. A segmentation of bone tissue is performed by thresholding (TH1) this final volume. For air cavities the low-pass filtered data are combined using the $(UTE1 + UTE2)/UTE1^2$. Again a segmentation of air cavities is performed by thresholding (TH2) the resulting volume. For soft tissue, a mask is first derived from the UTE2 volume and all voxels that are not bone or air inside the mask are assigned as soft tissue. This last step is also defined by thresholding (TH3).

As can be noted both methods need the optimization of 3 thresholds (TH1, TH2 and TH3). This optimization is not easy and to be as less subjective as possible an automatized method was performed. A brute force algorithm was developed to discover the best parameters that minimize the total dice coefficient (calculated by the mean of the dice coefficient for air, soft tissue and bone). This method is simple as it is only needed to define a range for each parameter and the algorithm tries every combination inside that range until a specific depth and the parameters that give the minimum total dice coefficient are returned.

6.2.2.5 Rota Kops method

As the template-based approach developed by Rota Kops can work with the UTE2 this method was also implemented. An autonomous method was implemented to derive the AC map from the template-based approach and can be seen in Figure 6.8. The algorithm showed to have similar accuracy as performed manually by using a combination of SPM2

and mpitool imaging tools and can take as low as 150 seconds to run the entire routine (depending on the machine).

At first the patient UTE image is loaded by the algorithm and the data resliced to match the MR template dimensions. As the template and patient MR volumes do not have the same dimensions the patient MR data need to be estimated (interpolated) for the positions where the template is defined so that the forward calculation work properly. Next, the non-linear registration (from the SPM8 subroutine) of the template MR image to the patient MR image was performed by normalizing the first to the second with a rough affine transformation, followed by a fine affine transformation and finally with a non-linear transformation. For the first two transformations (affine transformations) 12 parameters were optimized, corresponding to rotation (3 parameters), translation (3 parameters), shear (3 parameters) and scale (3 parameters) of the patient MR image. A second affine transformation is applied to better estimate the normalization coefficients. As it was explained, the affine transformation is limited to some operations and as it is known some differences between subjects anatomy exists (inter-subject variability) and such simple operations cannot correctly normalize two images. Thus, a non-linear transformation based in the Discrete Cosine Transform is employed to non-linear register the template MR to the patient MR. After the estimation of the transformation matrix this was applied to the MR template and the Attenuation template so that they were registered to the patient MR. As Dr. Rota Kops found out the application of a second spatial normalization performs better than a single spatial normalization, so the process of registration processed once again, now with the registration of the previous registered MR template to the patient MR. Finally the MR template and the Attenuation template obtained from the first registration were registered using the transformation matrix from the second registration, obtaining the final attenuation image of the patient and the second MR template registration.

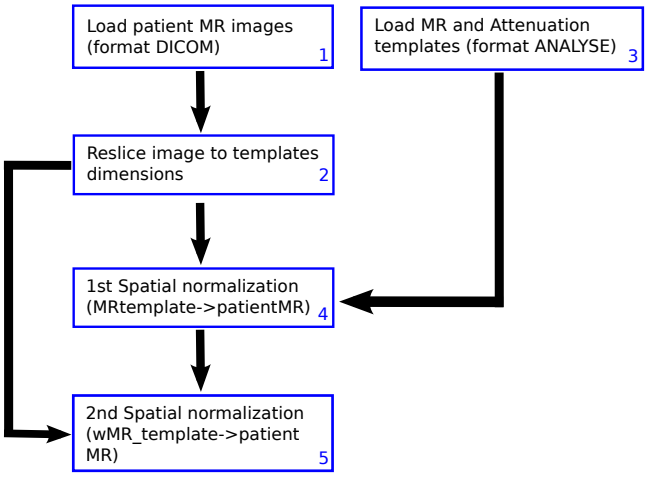

Figure 6.8: Scheme showing the template-based MR-AC algorithm implemented. The MR images from the patient are loaded (1) and resliced (2) to match the MR template (3). The MR template is spatial normalized to the resliced MR from the patient and the transformations applied to both the MR and Attenuation templates (4). The transformed MR template is again spatial normalized to the resliced MR from the patient and the transformations applied to both the transformed MR and transformed Attenuation templates from the first spatial normalization (5).

6.2.3 Post-processing and analysis

6.2.3.1 Post-processing

For all the segmentation-based AC methods adequate attenuation values were assigned to the different segmented classes. The attenuation values for brain tissue ($0.099cm^{-1}$), skull ($0.146cm^{-1}$) and soft tissue ($0.095cm^{-1}$) were determined by the ICRU report 46 that gives the elemental composition of these tissues, and from the NIST XCOM that gives the mass attenuation coefficient at 511keV for the composition. This process for determining simulated attenuation coefficients was suggested by Peng Qin [Peng Qin, "From MR images of the brain to attenuation maps usable for PET attenuation correction", Master Thesis, 2006]. As for the proposed methods brain tissue and the remain soft tissues cannot be distinguished a final attenuation value of ($0.097cm^{-1}$) was assigned to all tissues that where not air or bone.

The generated AC maps were translated and rotated to the same position of the PET emission scan, as there is a difference between the isocenter of the MR scanner and the PET scanner, and finally resliced to the dimensions of PET emission scan.

As the PET emission scan as a lower resolution than both CT and MR images the AC maps were smoothed with a 3mm FWHM Gaussian kernel to match the resolution of PET emission scan. The template-based method is an exception here as the generated AC map is already heavily smoothed.

The attenuation map for use in the reconstruction algorithm is not complete as it is only from the patient, and needs the addition of the attenuation by the coils. Therefore for all methods the attenuation from the coils is added to the attenuation from the patient before reconstruction.

The reconstructed PET image compensated for degrading effects was performed based in the OSEM algorithm as explained in chapter 2 with 2 subsets and 32 iterations.

For evaluation purposes as most of the CT images acquired do not cover the full FOV of the PET scanner a reconstruction with partial CT images would give heavy artefacts. Therefore the CT-AC and MR-AC maps were masked and completed with the template AC approach, Figure 6.9

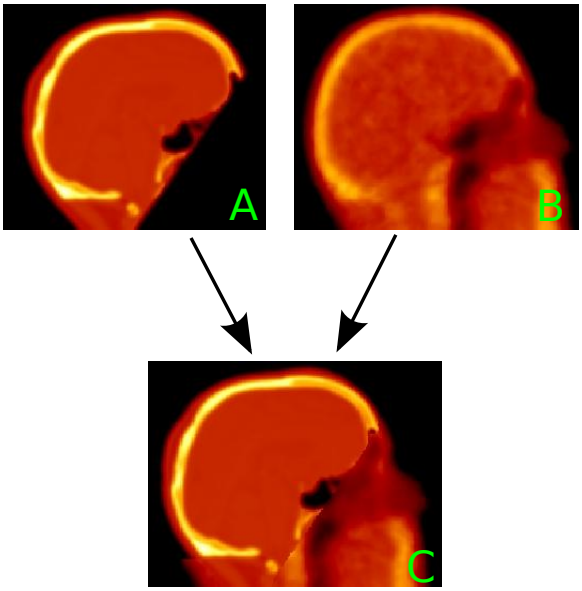

Figure 6.9: Scheme showing the derivation from a partial CT (A) to a hybrid CT (C) by completing the partial CT with template AC information (B).

6.2.3.2 AC map estimation analisys

In this work 6 different proposed methods (d-pnn (ute), d-ffnn (ute), d-pnn (ute+template), d-ffnn (ute+template), s-ffnn and s-som) and the Keereman's (d-keereman), Catana's (d-catana) and Rota Kops's (s-template) methods were implemented. Additionally for comparison the Scalled CT (s-ct) derived by [Carney et al., 2006] method and a Segmenting CT (d-ct) methods were implemented.

The differences between each method are explained below:

- d-pnn (ute) - Derived by giving as inputs to the PNN only the UTE1 and UTE2;
- d-ffnn (ute) - Derived by giving as inputs to the FFNN only the UTE1 and UTE2;
- d-pnn (ute+template) - Derived by giving as inputs to the PNN the UTE1, UTE2 and the template image derived by Rota Kops;
- d-ffnn (ute+template) - Derived by giving as inputs to the FFNN the UTE1, UTE2 and the template image derived by Rota Kops;
- s-ffnn - Derived by giving as inputs to the FFNN the UTE1, UTE2 and the template image derived by Rota Kops;

- s-som - Derived by giving as inputs to the SOM the UTE1, UTE2 and the template image derived by Rota Kops;

Notice that methods that have a prefix d- (discrete) will output a segmented image into 3 tissues:air, soft tissue and bone. Methods with a prefix s- (scaled) will output an AC map with a continuous range. Also, the s-ffnn and the s-som receive the scaled CT image in the training phase, while d-pnn (ute), d-ffnn (ute), d-pnn (ute+template), d-ffnn (ute+template) receive the segmented CT image.

6.2.3.2.1 Evaluation of dice coefficients For each patient dice coefficients (D) values were calculated for the whole head and skull for all patients and all methods, Figure 6.10. Segmentation of the images into 3 tissues: air (air), bone (bone) and soft tissue (st) was performed immediately before adding the attenuation from the coils. This approach was used so that all methods are segmented using the same thresholds and are therefore less dependent of the values choose. As it was previously defined the attenuation coefficient at 511 keV for air, soft tissue and bone are $0cm^{-1}$, $0.097cm^{-1}$ and $0.146cm^{-1}$, respectively. Therefore, two thresholds were defined to segment the different tissues that correspond to approximately the middle between the different attenuation coefficients and are $0.05cm^{-1}$ and $0.12cm^{-1}$.

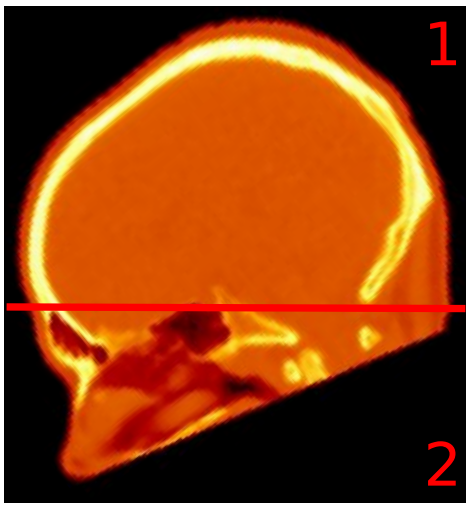

Figure 6.10: Illustration of the 2 regions defined (1 and 2 - whole head, 2 - pure skull without air cavities) for calculation of the Dice coefficients.

6.2.3.2.2 Evaluation by sensitivity correction map Additionally for all patients a sensitivity correction map was calculated to estimate the influence of differences in the AC map in the reconstructed

image (for a 2D PET), Figure 6.11. The sensitivity correction map was calculated as follows. All AC maps were slice-wise Radon-transformed to yield the respective sinograms representing the integrated attenuation coefficient along all in-slice lines of response. Recall that in chapter 2 and 3 it was explained that the attenuation along a line of response is given by $e^{-\int \mu(x,y)dy'}$.

The inverse Radon transform of the attenuation was calculated without filtering to yield a sensitivity map. Note that an unfiltered back-projection, is equivalent to averaging all sinogram entries containing a contribution from a voxel in image space. The reciprocal value of the sensitivity map, a sensitivity correction map, quantifies in-slice attenuation effects, and therefore is supposed to be an estimate of the AC influence on the reconstructed PET radiation intensities, [Berker et al., 2012]. Linear correlation of the sensitivity correction maps derived for every patient for every AC map was finally calculated.

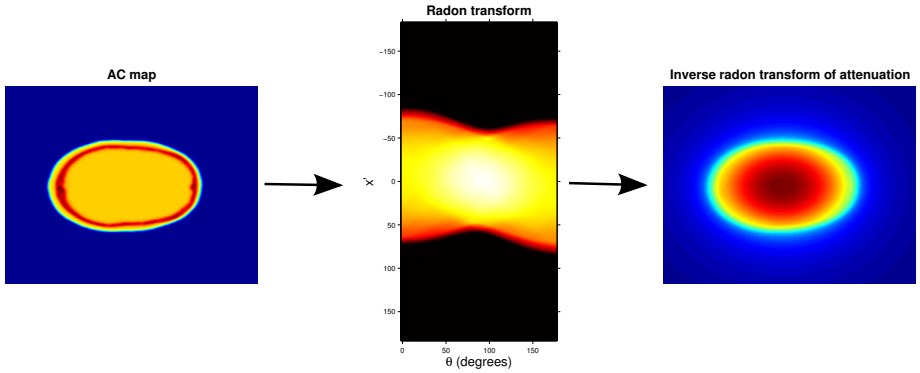

Figure 6.11: Scheme of the sensitivity correction map analysis. The AC map estimation is Radon transformed to obtain the respective sinograms. The attenuation for each LOR is calculated and the inverse Radon transform applied without filtering.

6.2.3.2.3 Evaluation by reconstructed PET images The reconstructed PET images were smoothed with a 2.5mm FWHM Gaussian kernel to reduce noise and improve the SNR (Figure 6.12 B). SPM8 was used to normalize the PET data to a template PET image (Figure 6.12 D). For each patient the normalized reconstructed PET image obtained using the CT-AC map was used to define a brain mask (Figure 6.12 E). A threshold defined as $> 0.3 * max$(reconstructed_ ct_ image) was therefore used to get the brain activity. The generated mask was applied on every normalized PET image for every MR-AC method for that patient.

Linear correlation between the masked PET images for every MR-AC method and the CT-AC method was performed.

Moreover, volumes of interest (VOIs) for all methods were applied to the reconstructed PET images, based in an Atlas image co-registered to the normalized PET image (Figure 6.12 G), and the different MR-AC methods compared in each region with the CT-AC method.

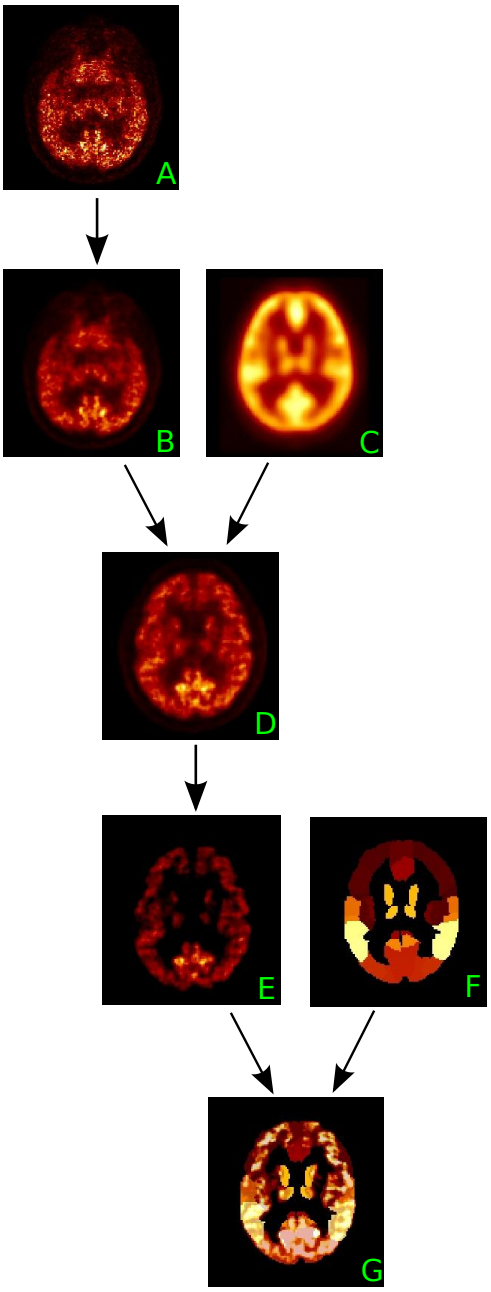

Figure 6.12: Illustration of the different steps in the evaluation of the reconstructed PET images. The reconstructed PET image (A) is first smoothed (B) and then normalized to a PET template (C) to yield an image in the template space (D). The normalized image is masked for brain tissue (E) and an atlas image (F) used for defining ROI in the masked PET image for analysis (G).

6.3 Results

In Figure 6.13 the AC map estimation for each method is presented for one sagittal slice of one patient. It can be seen that continuous methods present attenuation coefficients between air and soft tissue that can represent better air cavities than segmenting methods. Additionally Keereman's method present an over-classification of bone, especially at the occipital bone, and Catana's method presents an under-classification of bone, best seen at the nasal region. Moreover, both s-som and s-ffnn methods present better estimation of attenuation coefficients close to bone than template method.

In Figure 6.14 it is represented the segmented AC map estimation for each implemented method and for the same sagittal slice as represented in Figure 6.13. It can be seen that all method fail at segment bone correctly at the anterior region. Additionally, all segmentation-based methods present much larger air cavities than ideal. From the 9 implemented algorithms s-som shows to give visually the best results.

In Table 6.1 it is shown the mean values of the co-classification of 9 subjects for each method. As can be seen all methods have high co-classification values for air and soft tissue and lower values for bone. Additionally, the s-template method fail to accurately segment bone tissue (as it was also presented in Figure 6.14), presenting the lowest value of 0.3455. The total co-classification is presented in the 4^{th} column and is higher for the s-som followed by the d-pnn (ute), with 0.8991 and 0.8841, respectively. The s-template method presents the lowest total co-classification.

Table 6.1: Mean co-classification values for 9 patients for air (1^{st} column), soft tissue (2^{nd} column) and bone (3^{rd} column). The mean co-classification value for the aggregation of air, soft tissue and bone is also presented (4^{th} column).

	Air co-class.	St co-class.	bone co-class.	Tot. co-class.
d-ct	0.9994	0.9944	0.9632	0.9857
d-pnn (ute)	0.9843	0.9014	0.7668	0.8841
d-ffnn (ute)	0.9893	0.9208	0.6476	0.8526
d-pnn (ute+template)	0.9960	0.9218	0.6797	0.8658
d-ffnn (ute+template)	0.9969	0.9169	0.6753	0.8630
s-ffnn	0.9952	0.9456	0.6797	0.8735
s-som	0.9921	0.9263	0.7788	0.8991
d-catana	0.9727	0.9572	0.5313	0.8204
d-keereman	0.9800	0.8893	0.6449	0.8381
s-template	0.9935	0.9503	0.3455	0.7631

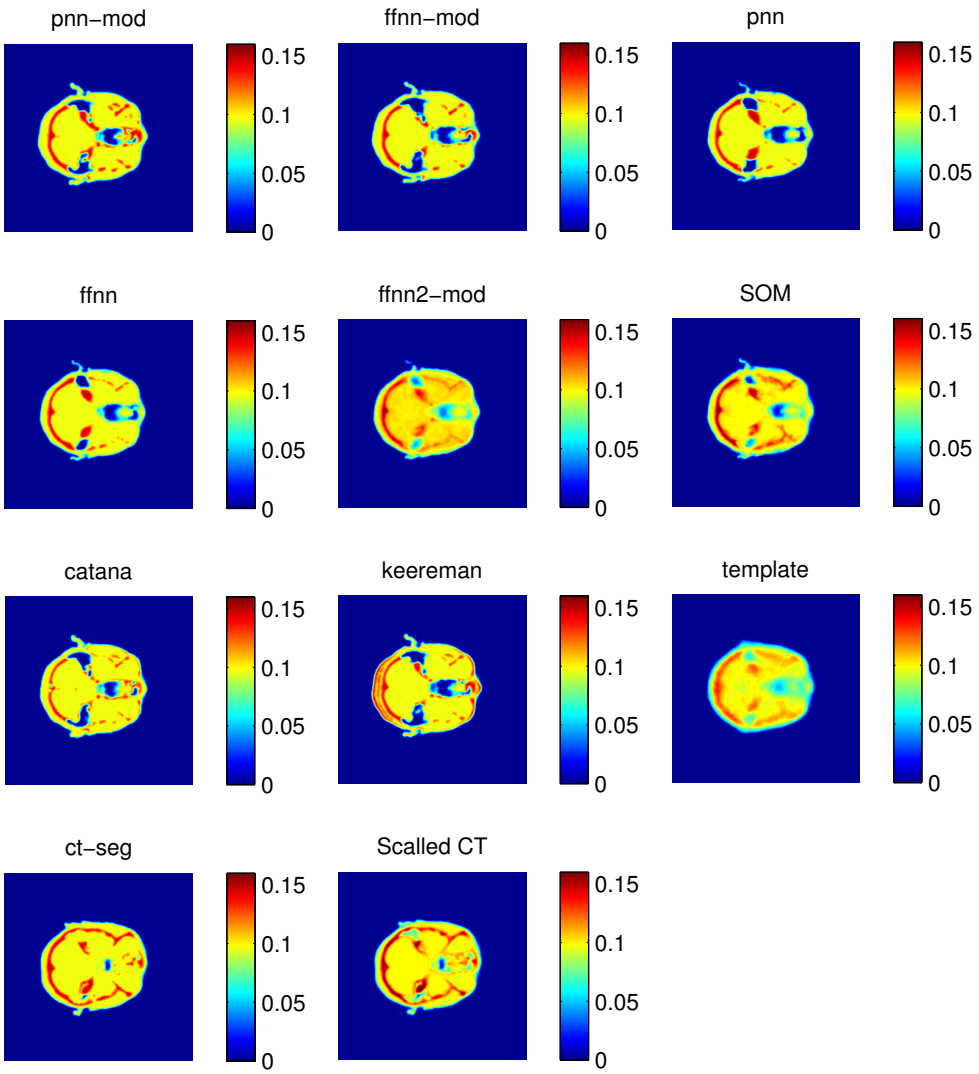

Figure 6.13: AC map estimation for all MR implemented algorithms and CT algorithms.

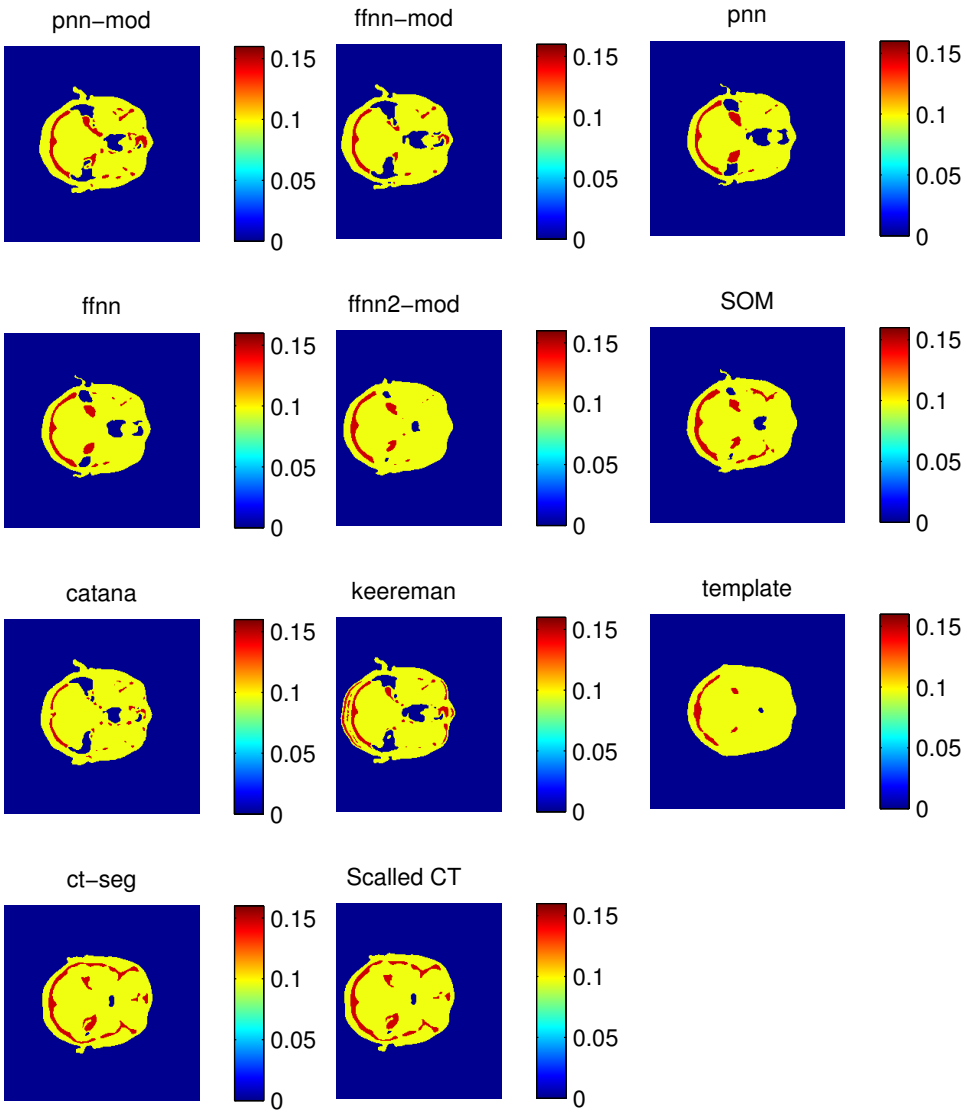

Figure 6.14: Segmented AC map estimation for all MR implemented algorithms and CT algorithms.

6.3.1 Evaluation of dice coefficients

6.3.1.1 Correctly classified tissues

The mean and standard deviation of the dice coefficients, corresponding to correctly classified tissues for the whole head are represented in Figure 6.15.

It can be seen that the air region presents the highest dice coefficients for all methods. Soft tissue also presents high dice coefficients for all methods with the highest for the s-ffnn and the lowest dice coefficient for d-keereman. Bone region presented the lowest dice coefficient of the three correctly classified classes with the highest for the s-som and the lowest for s-template. Bone region also presented the highest standard deviations of the three correctly classified classes for all methods.

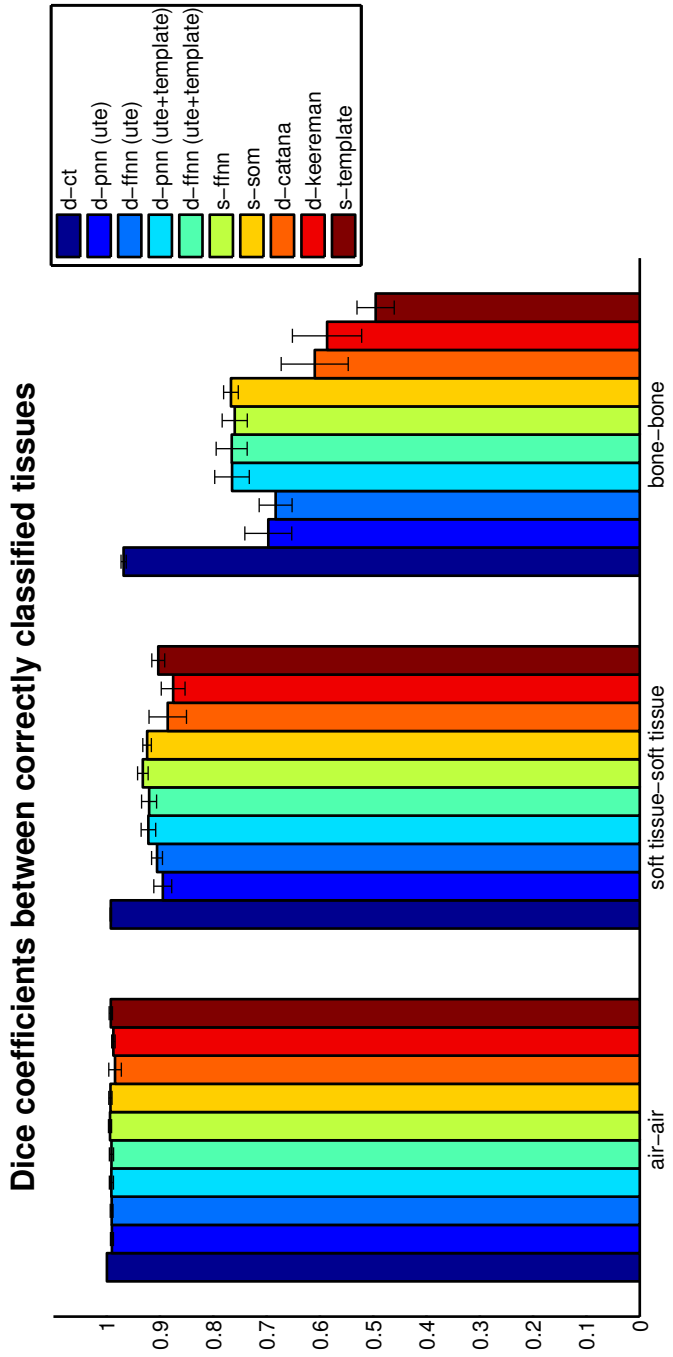

Figure 6.15: Dice coefficients for correctly classified tissues between segmented CT and segmented MR-AC methods.

6.3.1.2 Misclassified tissues

The mean and standard deviation of the dice coefficients, corresponding to misclassified tissues, for the different subjects were obtained and are represented in Figure 6.16.

It can be seen that air-bone and bone-air misclassifications presented the lowest dice coefficients for all methods with a maximum of 0.02. Bone-soft tissue and soft tissue-bone presented the highest dice coefficients. Additionally, it can be seen that d-pnn and d-catana present much higher dice coefficient between soft tissue-bone than bone-soft tissue, meaning that a global over-estimation of bone was obtained. In opposite, it can be seen that s-template presents a much higher dice coefficient between bone-soft tissue than soft tissue-bone and therefore an under-estimation of bone was observed. Moreover, it can be seen that d-catana presented high dice coefficients in both bone-soft tissue and soft tissue-bone, meaning that a wrong classification of bone was obtained.

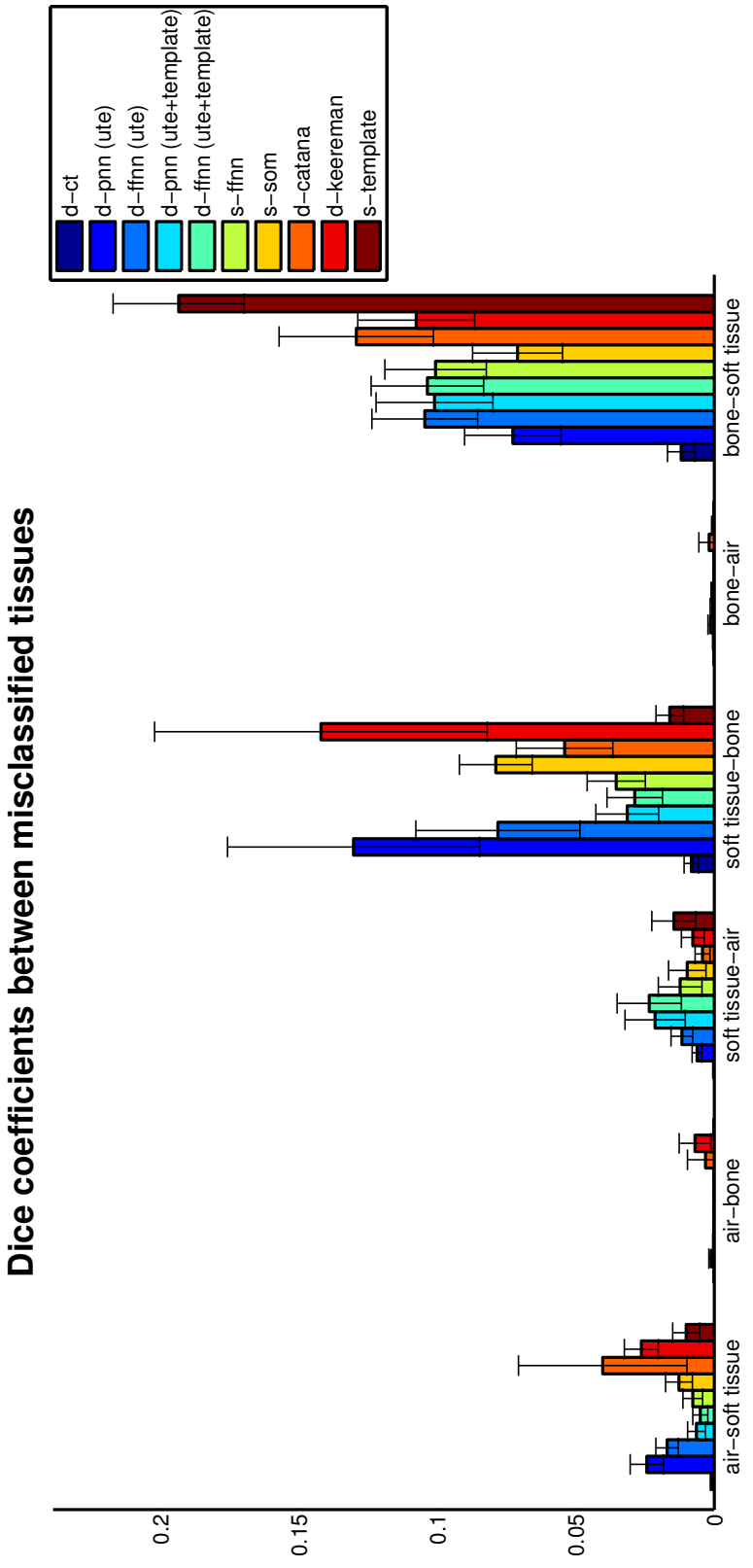

Figure 6.16: Dice coefficients for misclassified tissues between segmented CT and segmented MR-AC methods.

6.3.1.3 Comparison of dice coefficients for bone

To further analysis the bone tissue, the subjects MR images were divided into 2 regions (whole head and skull region) and the dice coefficients for each region calculated and compared. The results are presented in Figure 6.17. It can be seen the all the methods present higher dice coefficients for the skull region than for the whole head. Additionally, a higher increase is seen in the methods that were not aided by a template image.

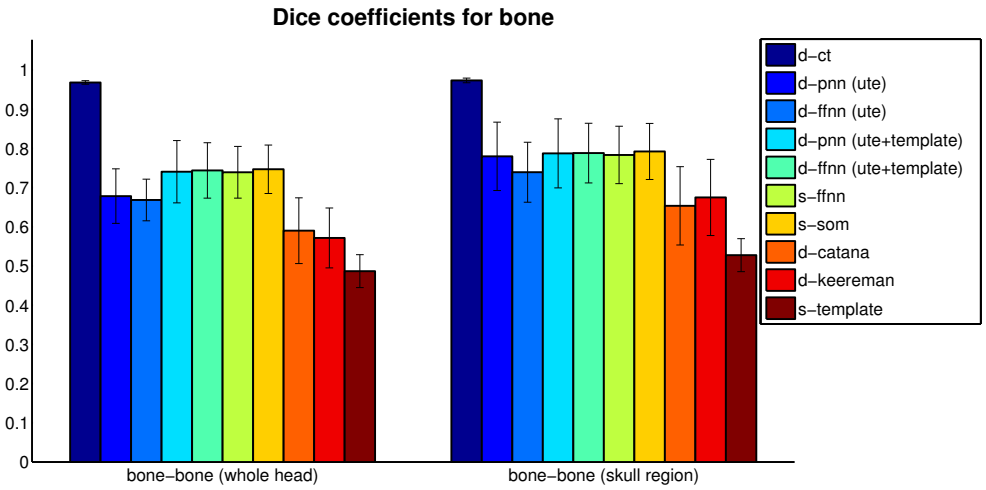

Figure 6.17: Dice coefficients for bone between segmented CT and segmented MR-AC methods. The dice coefficients for the whole head (left) and skull region (right) are presented.

6.3.2 Evaluation of sensitivity correction maps

A sensitivity correction map for all the presented methods MR and CT AC methods was performed and is presented in Figure 6.18. It can be seen that attenuation is higher for the middle of the head and decrease from inside out. Also, visual comparison of the sensitivity map derived from the presented method and from the CT scale map shows that the segmenting methods d-pnn(ute+template) and d-ffnn (ute+template) show the most differences.

A joint histogram between the sensitivity correction map obtained from the presented AC maps and the sensitivity correction map obtained from the CT scaled AC map was performed, and a linear regression between both calculated. The linear coefficients and linear correlation factor obtained for all methods are represented in Figure 6.19. As can be observed the linear correlation factor was near 1 for all methods, so that

a linear relation between the effect of attenuation (for a 2D PET system) with the presented maps and the scaled CT map can be assumed. The method that presented the best slope and intersect factors was the s-ffnn followed by the s-som. The method that presented the worst slope was the d-pnn(ute+template) followed by the d-ffnn (ute+template).

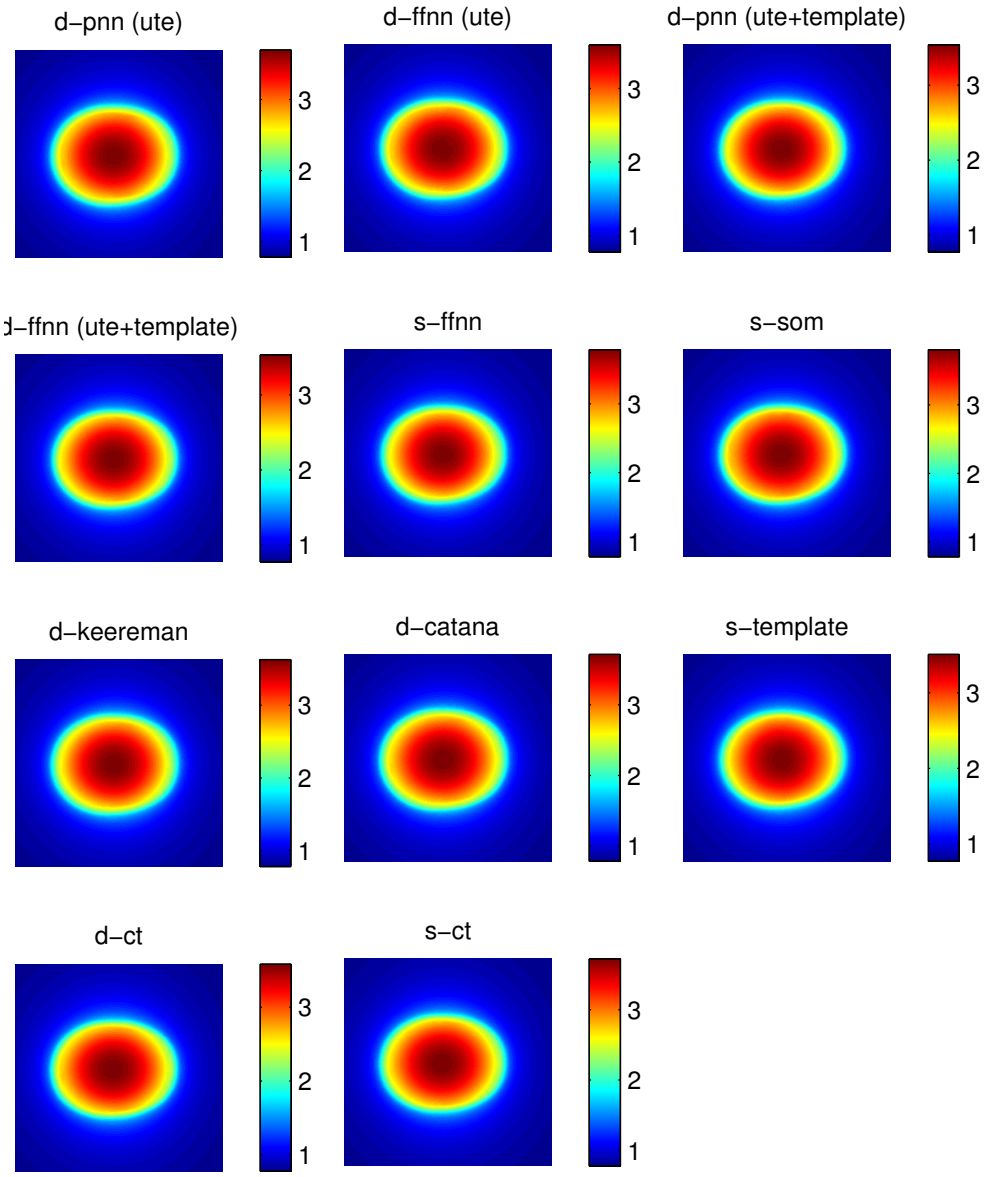

Figure 6.18: Sensitivity correction maps for the different MR-AC and CT-AC methods implemented. An axial slice is presented.

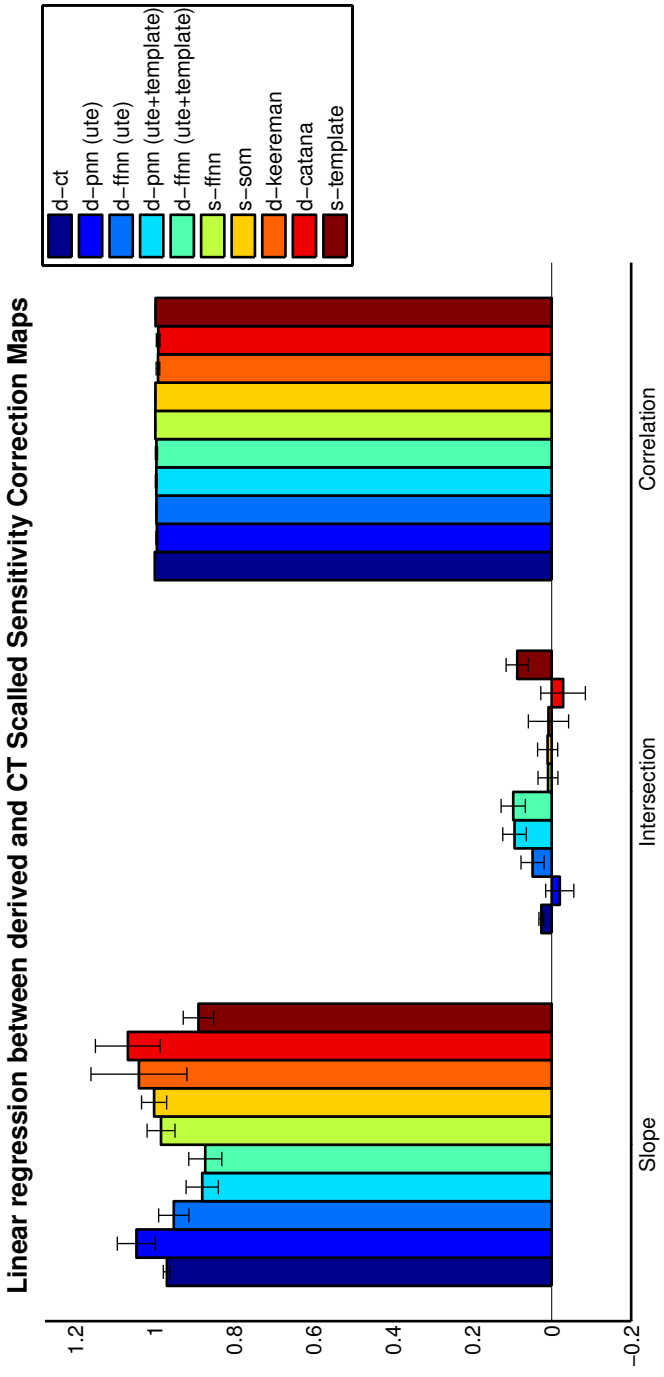

Figure 6.19: Linear regression coefficients (slope and intersect) and regression factor(correlation) between derived and CT scaled sensitivity correction maps.

6.3.3 Evaluation of reconstructed PET images

The reconstruction of the obtained PET images with the presented methods and the CT-AC map was performed and the relative differences between MR-AC and Scaled CT-AC maps was calculated, Figure 6.20 (The reconstructed PET images used to calculate the relative differences can be seen in Annex C). It can be seen that the segmented CT-AC performs close to Scaled CT-AC, with a relative difference of 5% without any positive or negative high error. Additional, all MR-AC methods with the exception of ffnn2 present errors as high as 10% with the highest negative errors presented by d-keereman and s-som algorithm and the highest positive errors for the d-pnn(ute+template), d-ffnn (ute+template) and s-template methods. Moreover, s-ffnn present relative difference errors close to the segmented CT-AT method (d-ct).

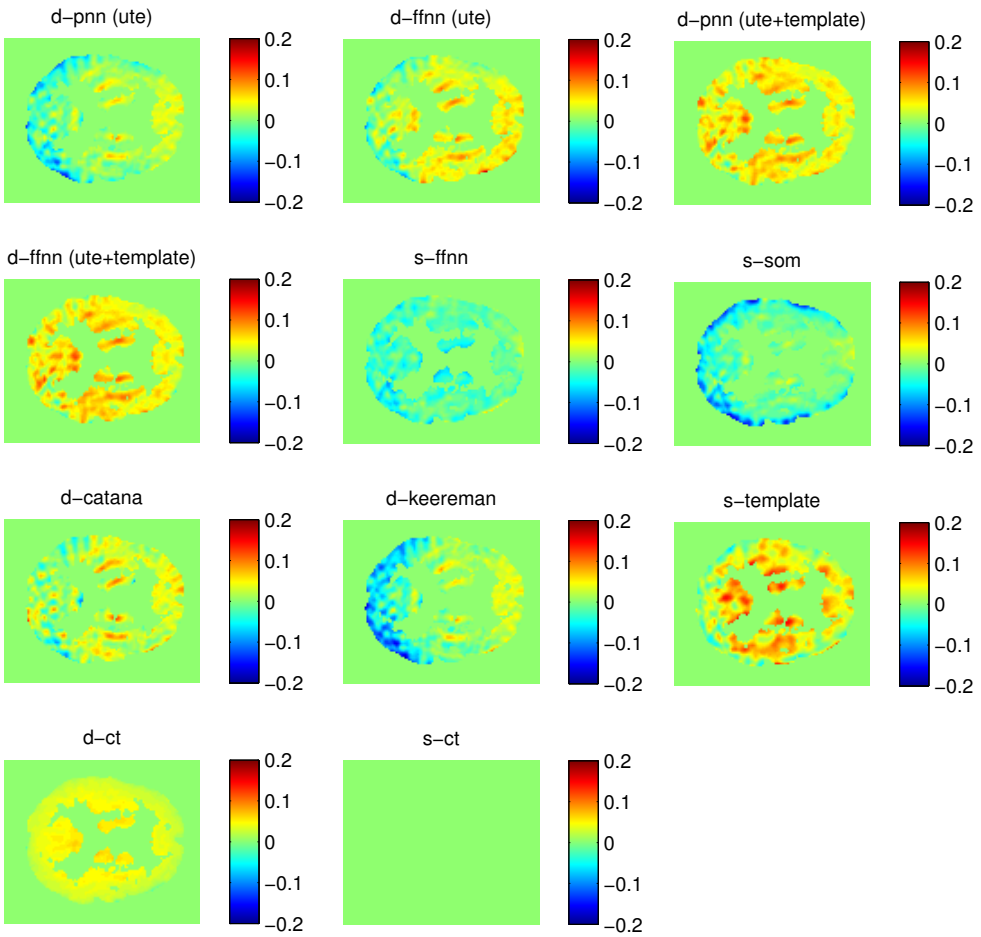

Figure 6.20: Relative differences between the reconstructed PET images corrected with the implemented methods and the CT scaled AC method.

The mean activity of the reconstructed PET images for 6 different regions (frontal, temporal, parietal, occipital, cerebellum, vermis) based in an atlas image co-registered to the reconstructed PET images was obtained. The relative differences between the mean activity of the reconstructed PET images with the MR-AC methods and with the CT-AC method was calculated and is presented in Figure 6.21.

For the whole brain tissue, all methods present mean relative differences between 4% and 5% with the exception of d-keereman with a relative difference of 6%. Additionally, for the whole brain tissue the method that showed the lowest relative difference was d-ffnn (ute) followed by s-ffnn. The regions that should the highest relative differences for the most of the methods were the occipital and the cerebellum regions. For all methods and all regions high standard deviation was observed.

A joint histogram between the reconstructed PET images with the presented attenuation maps and the reconstructed PET image with the CT scaled map was performed and a linear regression between both calculated. The linear coefficients and linear correlation factor obtained for all methods are represented in Figure 6.22.

As can be observed the linear correlation factor was near 1 for all methods, so that a linear relation between the reconstructed PET images with the presented maps and with the scaled CT map can be assumed. The methods that presented the best slope were the d-pnn (ute) and the s-som, and the best intersect were the d-ffnn (ute) and the d-pnn (ute+template).

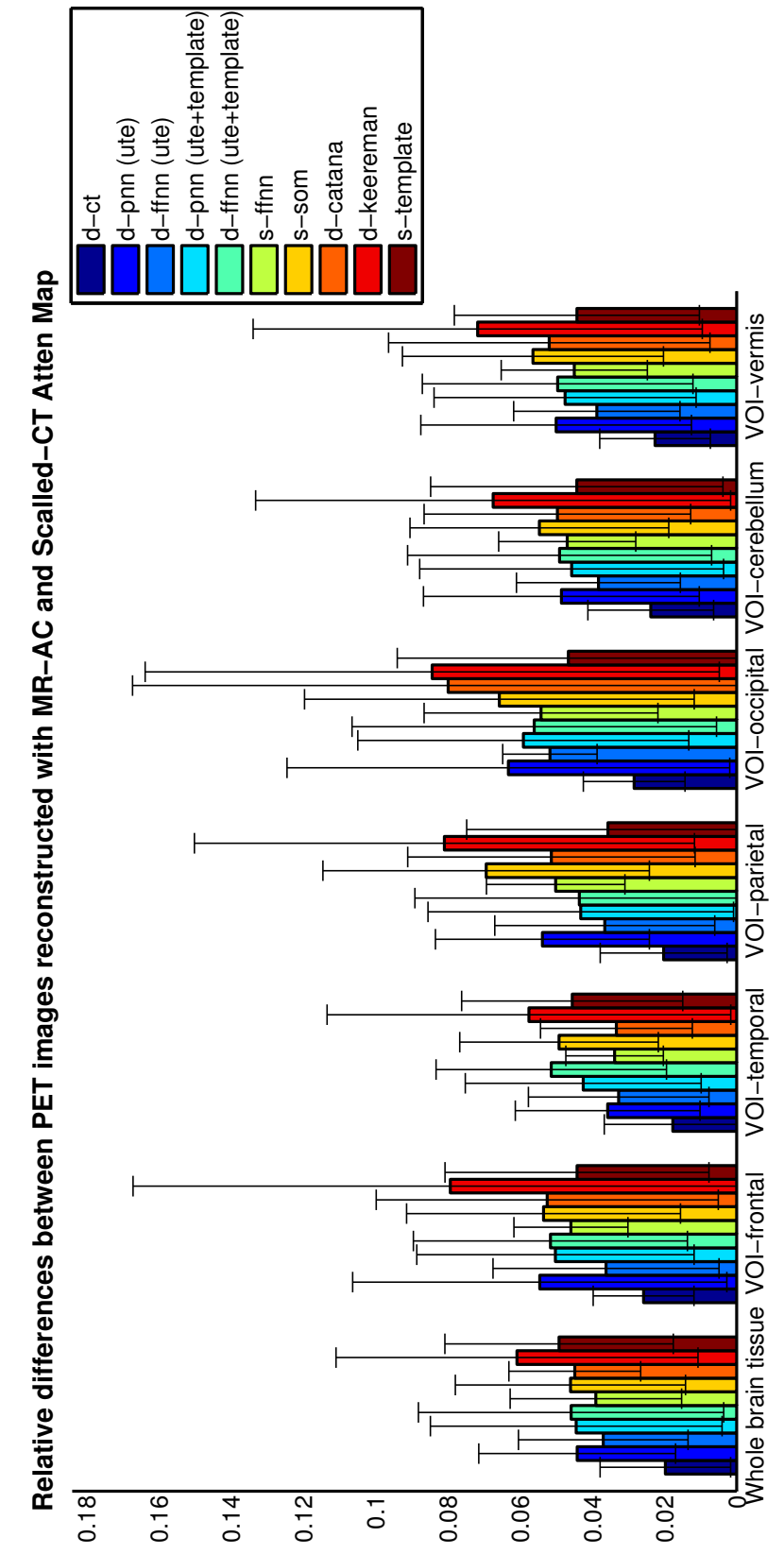

Figure 6.21: Relative differences between reconstructed PET images with MR-AC and CT scaled AC methods. The analysis was performed for each method for 6 VOI and the whole brain tissue.

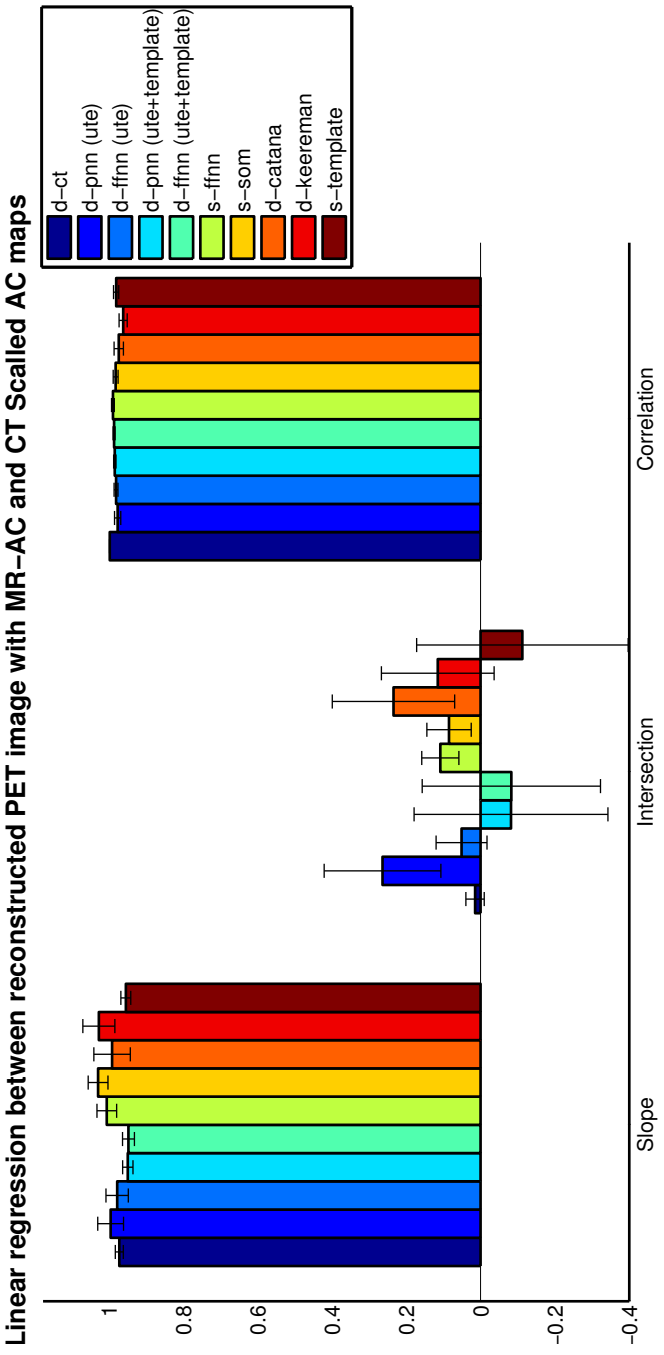

Figure 6.22: Linear regression coefficients (slope and intersect) and regression factor(correlation) between reconstructed PET images with MR-AC and CT scaled AC methods for the whole brain tissue.

6.4 Discussion

In Figure 6.13 it was presented the AC map estimation for all implemented algorithms for one axial slice. This result suggests that continuous methods tend to give better results than segmenting methods by allowing more attenuation coefficient values to be assigned, other than the 3 manually defined in segmenting methods (air -0cm^{-1}; soft tissue - 0.097cm^{-1}; bone - 0.146cm^{-1}). In fact the gold standard for AC map estimation is to transform the HU from a CT image into attenuation coefficients at 511 keV. This approach is used as it can account for the different densities of tissues and therefore give a better AC map estimation.

Additionally, the result suggests that methods that take into account the template image (segmenting or continuous methods) tend to be more specific. This is logical as the template image provides an atlas that guides the segmentation process and excludes points that are too far from the template.

In Figure 6.14 it was presented the segmentation of the AC map estimation into three tissues (air, soft tissue and bone) for all MR implemented algorithms for one axial slice. Additionally, in Table 6.1 the mean co-classification of all patients for each method was presented. Both of these results agree that the s-som method is more similar to the CT-AC map than the remain methods. Also, the s-template method tend to give worse results for bone classification than the remain methods. Regarding this last point, one observation must be made. The AC maps were segmented based in two manually defined thresholds: 0.05cm^{-1} and 0.12cm^{-1} and therefore changes in these thresholds affect the final segmentation and therefore the results obtained. Moreover, co-classification analysis should be taken with care as it can lead to wrong interpretations. As an example an AC method that over-classify a certain tissue will most of the times give better results when analysing the co-classification of that tissue. In the presented work this can be seen in the soft tissue co-classification in both d-catana and s-template methods. Both methods give the best results for soft tissue co-classification due to the over-classification of soft tissue (or otherwise under-classification of bone). Therefore further analysis are needed to be taken to an accurate analysis of the different methods.

6.4.1 Evaluation of dice coefficients

Dice coefficients were therefore calculated and were presented in Figure 6.15, 6.16 and 6.17. In Figure 6.15 it is shown that the s-template method present the lowest dice coefficient for bone, therefore in agree with Table

6.1. Yet the soft tissue dice coefficient was not the highest as it was suggested by Table 6.1. Moreover, it can be seen that the methods aided by the template image (d-pnn (ute+template), d-ffnn (ute+template), s-ffnn and s-som) performed better than the remain MR-AC methods, especially for bone classification. Nonetheless, this difference is attenuated if the dice coefficients for the skull region are calculated 6.17. This is because high motion artefacts at the facial region are presented in most of the MR images acquired leading to incorrect classification of tissues. Therefore, the results suggest that if artefact-free images are obtained, segmenting methods based solely on the intensities of the UTE images may be accurate enough for AC map estimation.

6.4.2 Evaluation of sensitivity correction maps

Sensitivity correction maps as it was explained are a way of estimating how the AC map will influence the PET reconstructed data. If plotted the MR-AC sensitivity correction map against the CT-AC sensitivity correction map the data should fall under a 45 degree line so that the prediction of the AC map is accurate. As it was verified in Figure 6.18 and 6.19 the methods that presented the best results were the s-ffnn and the s-som. The segmenting method that presented the best results was the d-pnn (ute). These results are in agree with the previous evaluation by the dice coefficients, yet d-pnn (ute+template) and d-ffnn (ute+template) presented the worst results in contrast to what was verified in the dice coefficient analysis. It should also be noted that the slope and intersect value obtained for d-pnn (ute+template) and d-ffnn (ute+template) are similar to what was obtained for the s-template method. This last statement suggest that both d-pnn (ute+template) and d-ffnn (ute+template) seems to improve classification of bone tissue relatively to the s-template method, yet are still very close to it.

6.4.3 Evaluation of reconstructed PET images

To measure the real influence of AC map estimation in reconstructed PET images the reconstruction of 4 PET images using the different implemented MR-AC methods was performed. It was verified in Figure 6.20 and 6.21 that s-ffnn performs better than the remain methods, yet in Figure 6.22 the correlation coefficients were not the best. Discrepancies between different analysis in the evaluation of reconstructed PET images can happen due to different factors. First only 4 subject PET images were reconstructed and therefore low statistical information can be acquired. Additional, only 2 from the 4 subjects had performed a full CT and therefore the analysis is compromised.

6.5 Conclusion

The generation of an AC map to correct the PET image data is still a problem to current MR-PET scanners. Methods based on the MR-UTE sequence show to be promising for AC map estimation, however still present some limitations, such as high influence due to MR artefacts such as motion or IH. Artefact-free images are therefore needed for accurate AC map estimation.

Moreover, it was shown that different analysis to study AC map estimation may lead to different outcomes due to limitations from each analysis. Dice coefficients analysis has the advantage of directly compare the AC map obtained from a segmenting method and a standard method such as segmenting CT-AC. Yet, dice coefficients do not account for the relevance of the errors in the AC map. As an example, a misclassification of bone in the middle of the brain tissue would have the same importance as in the facial region or neck. Also, dice coefficients do not take into account the attenuation coefficients assigned to each class.

On the other hand, sensitivity correction maps account for the different attenuation coefficients and take into account where misclassifications appear. Yet, sensitivity correction maps have been implemented using the 2D Radon Transform and therefore do not account with cross-LORs. Moreover, the whole geometry of the PET system was not taken into account.

Reconstruction of PET images by the different MR-AC methods and comparison with CT-AC methods has long been assumed to be the best analysis. Still, this analysis has its own drawbacks. First, along with the MR images for AC map estimation and the CT images for comparison the subject need to performed a PET image as well. Additional, full CT images are normally needed for reconstruction purposes (a hybrid approach have been presented to avoid this limitation).

Due to the different analysis limitations an UTE-MR simulation along with a PET emission scan simulation for the same phantom should be performed as a ground true, artefact free methodology for AC map analysis.

Although some different outcomes from the different analysis were presented some conclusions can still be summarized. First the proposed methods tend to produce better results than current published methods working with UTE. Additionally, continuous methods such as s-ffnn and s-som do not suffer the limitation of segmenting algorithms (accuracy dependent upon the number of classes). This is important in air cavities where assignment of air or soft tissue leads to high errors. Moreover, the methods developed that make use of the template image, showed to

improve the accuracy of segmentation when only the template image was used.

Finally, it should be noted that the proposed continuous methods presented in some cases very high results and with future improvements may lead to the their use for AC map estimation in PET/MR scanners avoiding the acquisition of a CT image and therefore lowering the radiation dose taken by the patient.

Chapter 7

General Conclusions

In this chapter, a general overview of the work presented in this thesis is given. For each chapter, the most important results are summarized together with the conclusions that can be drawn from them. Afterwards, an overall conclusion is presented.

7.1 Summary

In chapter 2, a number of concepts and methods that are used throughout this work were introduced. In the first part, MRI was discussed. First it was explained the principles of MRI, from the most basic, such as spin principles. The imaging principles of MRI, as well as, the most important MRI sequences and the UTE sequence were also presented. Additionally, the image degrading effects important in MR were covered. Finally an overview of the main MRI hardware was introduced. In the second section it was explained the principles of PET from the very basic such as, tracer physical principles, to acquisition of the data and the imaging principles of PET. The image degrading effects in PET were introduced briefly. Image reconstruction techniques were introduced and given special attention to the workflow of iterative algorithms and image degrading compensation as this methodology was used in the present work. Finally as in the previous section an overview of the main PET hardware was introduced. In the last section, it was covered the hybrid technique PET/MR, the advantages and design problems that arise from the combination of PET and MRI. Finally the developed systems for the hybrid PET/MR were overview.

In chapter 3, the state-of-the-art in AC of PET was introduced. In the first section the effects of attenuation was discussed. Distinction between absolute quantification and clinical interpretation were distinguished in this section. It was discussed that attenuation correction

improves accuracy in clinical interpretation and is indispensable in absolute quantification. In the second section attenuation correction was further discussed, from the fundamental equations to derive an corrected image to the generation of ACF from transmission source. In the third section the different methods that have been used historically to derive the attenuation map were discussed. Special attention was given to MRI-based AC methods, as this was the focus of this thesis. The advantages and limitations of each MR-based method were introduced. These techniques still present some drawbacks: the techniques of MR-based AC by segmentation depend on the implemented segmentation algorithm as well as on the number of segmented structures. On the other hand, the MR-based AC techniques by templates cannot be generalized to a whole-body AC, and the atlas technique often has the problem that a one-to-one correspondence between the patient image and the pseudo-CT is not necessarily given.

In chapter 4, the principal artefacts to affect AC map estimation were identified and analysed. Motion and IH artefacts were identified as the principal MR artefacts to directly influence the AC map estimation, as in the first spatial relation between both UTE images is lost for the region where motion occur, and in the second high IH lead to differences between both UTE images and may consequently lead to misclassification of tissues. Regarding metal implants it was verified that they do not introduce relevant artefacts in the acquired UTE images. Nonetheless, CT images presented streak artefacts near the metal implants. This artefact, as well as co-registration mismatch can indirectly influence the AC map estimation by leading to incorrect training data.

In chapter 5 a method for IH correction was suggested. This method is based on the minimization of variation of information of two MR images from the subject. The method was tested with simulated and real data and the results discussed. Regarding simulated data the method proved to achieve good results by drastically reducing the CJV of both given simulated images. The method however tend to overcompensate bias field effect and a stop condition based in the number of iterations must be used to avoid severe artefacts. In respect to real data, as ideal images are not possible the images were analysed regarding homogeneity by the calculation of the CV for air, bone and soft tissue. The results showed that the overall tissues present higher homogeneity after IH correction, leading to easier and better tissue classification. Additionally, a simple segmentation method was proposed to evaluate the influence of bias correction in AC map estimation. This approach showed that without bias correction, simple classification methods tend to over-classify bone in the occipital and near the frontal sinus regions.

In chapter 6 the core of AC map estimation was presented. In this chapter three ANN approaches were proposed to determine an AC map: PNN, FFNN and SOM. The advantage of each method was discussed. The methodology of AC map estimation by the proposed machine learning algorithms was given and the results of AC map estimation were discussed. In sum the different analysis showed slightly different results regarding the methods that perform best. Nevertheless, all the analysis showed that the methods developed work similar to better than the ones currently proposed. All the method showed a quick and an easy parameter optimization. The methods aided by the template image showed to be more robust and with higher specificity than the ones without, although decreasing in sensitivity. Finally, the continuous methods developed showed to be promising as they can estimate different attenuation coefficients within a certain range for the same tissue and therefore account for different densities.

7.2 Future prospects

Several aspects have been reported during this work regarding the feasibility of AC methods.

First, artefacts that may lead to incorrect AC map estimation were analysed.

Motion artefacts from MR images showed to be a severe problem in AC map estimation, and can fatally lead to the impossibility of using MR intensity only methods. Therefore restraint mechanisms such as head holders should be studied to decrease motion artefacts to acceptable values. Other options should be to anesthesiate the patient, although this should not be the best option.

IH artefacts from MR images showed as well as motion artefacts to influence AC map estimation and this way should be kept as low as possible. An IH correction method for UTE images was proposed based on the multiple images acquired using this MR sequence. Although the preliminary results showed that the method developed increase the accuracy of the posterior classification methods for AC map estimation, different methods must be implemented and compared against the developed method both in a simulation as well as in real data.

Coregistration mismatch and metal artefacts showed to be a particular problem in the analyse of different AC methods. Without perfect coregistration and artefact free images, comparison among different methods should be taken with care. Additionally, to lower the dose of the patients, some of the CT scans are performed in such a way that only the brain region is imaged. This is a problem in the analyse of AC

methods as an attenuation image of the full FOV of the PET scan is needed. Therefore, for true comparison between different AC methods, simulation of the acquired MR images and the radiotracer activity in a PET scan should be performed.

Regarding the AC methods analyse it was shown that the developed method perform better than current methods based in UTE images. Nevertheless, the analysis was performed with few subjects and with partial CT images as it was already discussed. In future projects analysis with complete CT must be taken to truly compare AC methods based in the UTE sequence. Moreover, methods based in other MR sequences should be implemented and tested against AC methods based in the UTE sequence. Finally, as it was already suggested an UTE simulation should be performed, as this would give a ground true for all UTE methods.

Some of the conclusions here presented suggest that an UTE simulation and respective PET scan simulation should be performed as a ground true, artefact free methodology for AC map analysis. Therefore this idea will be further discussed. Regarding MR simulation Brainweb simulations have long been used for comparison between artefact correction and segmentation algorithms. Custom simulations are possible yet, very limited. UTE specific sequence is not available, as well as the tissue MR parameters used are not correct for bone tissue. One possible solution would be to use the JEMRIS: MR Simulations Software to develop the UTE sequence and simulate the acquired images for a given phantom. Preliminary tests have already been pursued and the 3D MR sequence implemented. Yet, radial reconstruction algorithms still need to be developed and implemented as the JEMRIS software do not provide any reconstruction algorithms. On the other hand, PET simulation has already been developed and was presented at the MIC by N. da Silva et al. for a brain phantom and can be used for this purpose.

Bibliography

M.R. Ay and S. Sarkar. Computed Tomography Based Attenuation Correction in PET/CT: Principles, Instrumentation, Protocols, Artifacts and Future Trends. *Iran J Nucl Med*, 15:1–29, 2007.

C. Bai, P. Kinahan, D. Brasse, C. Comtat, D.W. Townsend, C.C Meltzer, V. Villemagne, M. Charron, and M. Defrise. An analytic study of the effects of attenuation on tumor detection in whole-body PET oncology imaging. *J Nucl Med*, 44:1855–1861, 2003.

Dale L. Bailey. Transmission scanning in emission tomography. *Eur J Nucl Med*, 25:774–787, 1988.

D.L. Bailey, D.W. Townsend, P.E. Valk, and M.N. Maisey, editors. *Positron Emission Tomography: Basic Sciences*. Springer-Verlag London Limited, 2005.

J.D. Barnwell, J.K. Smith, and M. Castillo. Utility of Navigator-Prospective Acquisition Correction Technique (PACE) for Reducing Motion in Brain MR Imaging Studies. *AJNR Am J Neuroradiol*, 28: 790–791, 2007.

B. Belaroussi, J. Milles, S. Carme, Y.M. Zhu, and H. Benoit-Cattin. Intensity non-uniformity correction in MRI: Existing methods and their validation. *Med Image Anal.*, 10:234–246, 2006.

M. Bergström, Litton J, Eriksson L, Bohm C, and G. Blomqvist. Determination of Object Contour from Projections for Attenuation Correction in Cranial Positron Emission Tomography. *J Comput Assist Tomo*, 6:365–372, 1982.

Y. Berker, J. Franke, A. Salomon, M. Palmowski, H.C.W. Donker, Y. Temur, F.M. Mottaghy, C. Kuhl, D. Izquierdo-Garcia, Z.A. Fayad, F. Kiessling, and V. Schulz. MRI-Based Attenuation Correction for Hybrid PET/MRI Systems: A 4-Class Tissue Segmentation Technique Using a Combined Ultrashort-Echo-Time/Dixon MRI Sequence . *J. Nucl. Med.*, 53:796–814, 2012.

T. Beyer, P.E. Kinahan, D.W. Townsend, and D. Sashin. The use of X-ray CT for Attenuation Correction of PET Data. *IEEE*, 4:1573–1577, 1995.

K. Bilger, J. Kupferschlager, W. Muller-Schauenburg, F. Niisslin2, and R. Bares. Threshold Calculation for Segmented Attenuation Correction in PET with Histogram Fitting. *IEEE T Nucl Sci*, 48:43–50, 2001.

R.G. Boyes, J.L. Gunter, and C. Frost. Intensity non-uniformity correction using N3 on 3-T scanners with multichannel phased array coils. *Neuroimage*, 39:1752–1762, 2008.

C. Burger, Goerres G, Schoenes S, Buck A, Lonn AH, and GK. Von Schulthess. PET attenuation coefficients from CT images: experimental evaluation of the transformation of CT into PET 511-keV attenuation coefficients. *Eur J Nucl Med*, 29:922–927, 2002.

L. Caldeira, J.J. Scheins, P. Almeida, J. Seabra, and H. Herzog. Modified Median Root Prior Reconstruction of PET/MR Data Acquired Simultaneously with the 3TMR-BrainPET . In *IEEE Nuclear Science Symposium Conference Record-MIC21.S-30*, 2011.

JP. Carney, DW. Townsend, V. Rappoport, and B. Bendriem. Method for transforming CT images for attenuation correction in PET/CT imaging. *Med Phys*, 33:976–983, 2006.

C. Catana, A. van der Kouwe, T. Benner, M. Hamm, C. Michel, B. Fischl, M. Schmand, B. R. Rosen, and A. G. Sorensen. Is Accurate Bone Segmentation Required for MR-based PET Attenuation Correction? *Proc. Intl. Soc. Mag. Reson. Med.*, 17:592, 2009.

C. Catana, A. Kouwe, T. Benner, C.J. Michel, M. Hamm, M. Fenchel, B. Fischl, B. Rosen, M. Schmand, and A.G. Sorensen. Toward Implementing an MRI-Based PET Attenuation-Correction Method for Neurologic Studies on the MR-PET Brain Prototype. *J Nucl Med*, 51: 1431–1438, 2010.

Y. Censor, D.E. Gustafson, A. Lent, and H. Tuy. A new approach to the emission compurized tomography problem: simultaneous calculation of attenuation and activity coefficients. *IEEE T Nucl Sci*, 26:2775–2779, 1979.

C.A. Cocosco, V. Kollokian, R.K.-S. Kwan, G. Bruce Pike, and A.C. Evans. BrainWeb: Online interface to a 3D MRI simulated brain database. *NeuroImage*, 1997.

C. Comtat, P.E. Kinahan, and M. Defrise. Fast reconstruction of 3D PET data with accurate statistical modeling. *IEEE Transaction on Nuclear Science*, 45:1083–1089, 1998.

A.D. Costa, D.W. Petrie, Y.F. Yen, and M. Darangova. Using the axis of rotation of polar navigator echoes to rapidly measure 3D rigid-body motion. *Magnet Resson Med*, 53:150–158, 2005.

Nuno André da Silva. On the use of image derived input function for quantitative PET imaging with a simultaneous measuring MR-BrainPET. Master's thesis, Faculty of Sciences of University of Lisbon, 2012.

BM. Dawant, AP. Zijdenbos, and RA. Margolin. Correction of intensity variations in MR images for computer-aided tissue classification. *IEEE Trans Med Imaging*, 12:770 –781, 1993.

C.M. de Bazelair and G.D. Duhamel. MR imaging relaxation times of abdominal and pelvic tissues measured in vivo at 3.0T: preliminary results. *Radiology*, 230:652–659, 2004.

D. Delft and P. Kes. The discovery of superconductivity. *Physics Today*, pages 38–43, 2010.

J. Du, K. Borden, E. Diaz, M. Bydder, W. Bae, S. Patil, G. Bydder, , and C. Chung. Imaging of Metallic Implant Using 3D Ultrashort Echo Time (3D UTE) Pulse Sequence. *Proc. Intl. Soc. Mag. Reson. Med. 18*, 18, 2010.

L.J. Erasmus, D. Hurter, M. Naude, H.G. Kritzinger, and S. Acho. A short overview of MRI artefacts. *S Afr J Rad*, 8:13–17, 2004.

E.Rota Kops, G. Wagenknecht, J. Scheins, L. Tellmann, and H. Herzog. Attenuation Correction in MR-PET Scanners with Segmented T1-weighted MR Images. *Nuclear Science Symposium Conference Record (NSS/MIC), IEEE*, pages 2530–2533, 2009.

M. Filippi, N. Stefano, V. Dousset, and J.C. McGowan, editors. *MR Imaging in White Matter Diseases of the Brain and Spinal Cord*. Medical Ragiology, Diagnostic Imaging, Springer, 2005.

G. German and E.J. Hoffman. A study of data loss and mispositioning due to pileup in 2-D detectors in PET . *IEEE T Nucl ScI*, 37:671–675, 1990.

J.D. Gispert, S. Reig, J. Pascau, J.J Vaquero, P. Garcia-Barreno, and M. Desco. Method for bias field correction of brain T1-weighted magnetic resonance images minimizing segmentation error. *Hum Brain Mapp.*, 22:133–144, 2004.

N. Guillette, O. Sarrhini, R. Lecomte, and M. Bentourkia. Correction of partial volume effect in the projections in PET studies. *Nuclear Science Symposium Conference Record (NSS/MIC), 2010 IEEE*, pages 3541–3543, 2010.

M. Gunther and D.A. Feinberg. Ultrasound-guided MRI: Preliminary results using a motion phantom. *Magnet Resson Med*, 52:27–32, 2004.

M.J. Guy, I.A. Castellano-Smith2, M.A. Flower, G.D. Flux, R.J. Ott, and D. Visvikis. DETECT-dual energy transmission estimation CT-for improved attenuation correction in SPECT and PET. *IEEE T Nucl ScI*, 45:1261–1267, 1998.

Hamamatsu. Technical Information SD-28: Characteristics and use of Si APD (Avalanche Photodiode). Technical report, 2004.

H. Herzog. PET/MRI: Challenges, Solutions and Perspectives. *Zeitschrift für Medizinische Physik*, 2012. URL `http://dx.doi.org/10.1016/j.zemedi.2012.07.003`.

F. Hofheinz, J. Langner, B. Beuthien-Baumann, L. Oehme, J. Steinbach, J. Kotzerke, and J.Hoff1. Suitability of bilateral filtering for edge-preserving noise reduction in PET . *EJNMMI Research*, pages 1–23, 2011.

M. Hofmann, Steinke F, Scheel V, Charpiat G, Farquhar J, Aschoff P, Brady M, Schölkopf B, and BJ. Pichler. MRI-Based Attenuation Correction for PET/MRI: A Novel Approach Combining Pattern Recognition and Atlas Registration. *J Nucl Med*, 49:1875–1883, 2008.

M. Hofmann, Pichler B, Schölkopf B, and T. Beyer. Towards quantitative PET/MRI: a review of MR-based attenuation correction techniques. *Eur J Nucl Med Mol Imag*, 36:S93–S104, 2009.

J.E. Holmesa and G.M. Bydderb. MR imaging with ultrashort TE (UTE) pulse sequences: Basic principles. *Radiography*, 11:163–174, 2005.

Z. Hou, S. Huang, Q. Hu, and WL. Nowinski. A fast and automatic method to correct intensity inhomogeneity in MR brain images. *MICCAI*, 2006.

Z. Hu, N. Ojha, S. Renisch, V. Schulz, I. Torres, A. Buhl, D. Pal, G. Muswick, J. Penatzer, T. Guo, P. Bonert, C. Tung, J. Kaste, M. Morich, T. Havens, P. Maniawski, W. Schafer, R.W. Gunther, G.A. Krombach, and L. Shao. MR-based Attenuation Correction for a Whole-body Sequential PET/MR System. *IEEE Nuclear Science Symposium Conference Record*, pages 3508–3512, 2009.

SC. Huang, Hoffman EJ, Phelps ME, and DE. Kuhl. Quantititation in Positron Emission Computed Tomography: 2.Effects of Inaccurate Attenuation Correction. *J Comp Assist Tom*, pages 804–814, 1979.

Sung-Cheng Huang, Richard E. Carson, Michael E. Phelps, EdwardJ. Hoffman, Heinrich A. Schelbert, and David E. KuhI. A Boundary Methodfor AttenuationCorrectionin Positron Computed Tomograph. *J Nucl Med*, 22:627–637, 1981.

H. Jadvar and J.A. Parker. *Clinical PET and PET/CT*. Springer, 2005.

Ze-Xuan Ji, Quan-Sen Sun, and De-Shen Xia. A modified possibilistic fuzzy c-means clustering algorithm for bias field estimation and segmentation of brain MR image. *Computerized Medical Imaging and Graphics*, 35:383–397, 2011.

M.S. Judenhofer, C. Catana, B.K. Swann, S.B. Siegel, WI. Jung, R.E. Nutt, S.R. Cherry, C.D. Claussen, and B.J. Pichler. PET/MR Images Acquired with a Compact MR-compatible PET Detector in a 7-T Magnet. *Radiology*, 244:807–814, 2007.

A.C. Kak and Malcolm Slaney, editors. *Principles of Computerized Tomographic Imaging*. IEEE Press, 1988.

J.S. Karp, G. Muehllehner, He Qu, and Xiao-Hong Yan. Singles transmission in volume-imaging PET with a 137Cs source. *Phys Med Biol*, 40:929–944, 1995.

V. Keereman, Fierens Y, Broux T, De Deene Y, Lonneux M, and S. Vandenberghe. MRI-Based Attenuation Correction for PET-MRI Using Ultrashort Echo Time Sequences. *J Nucl Med*, 51:812–818, 2010.

Vincent Keereman. *MRI-Based Attenuation Correction for Emission Tomography*. PhD thesis, Faculteit Ingenieurswetenschappen en Architectuur, 2012.

P.E. Kinahan, D.W. Townsend, T. Beyer, and D. Sashin. Attenuation correction for a combined 3D PET-CT scanner. *Med Phys*, 25:2046–2053, 1998.

P.E. Kinahan, B.H. Hasegawa, and T. Beyer. X-Ray-Based Attenuation Correction for Positron Emission Tomography/Computed Tomography Scanners. *Seminars in Nuclear Medicine*, XXXIII:166–179, 2003.

A.S. Kiro, J.Z. Piao, and C.R. Schmidtlein. Partial volume effect correction in PET using regularized iterative deconvolution with variance control based on local topology. *Phys Med*, 53:2577–2591, 2008.

M.L. Kusano and C.B. Caldwell. Regional effects of an MR-based brain PET partial volume correction algorithm: a Zubal phantom study. *Nuclear Science Symposium Conference Record, 2005 IEEE*, 4:2204–2208, 2005.

K.J. LaCroix, B.M.W. Tsui, B.H. Hasegawa, and J.K. Brown. Investigation of the use of X-ray CT images for attenuation compensation in SPECT. *IEEE TRANSACTIONS ON NUCLEAR SCIENCE*, 41: 2793–2799, 1994.

S.H. Lai and M. Fang. A dual image approach for bias field correction in magnetic resonance imaging. *Magn Reson Imaging.*, 21:121–125, 2003.

R. Le Goff-Rougetet, V. Frouin, JF. Mangin, and B. Bendriem. Segmented mr images for brain attenuation correction in pet. *Proc. SPIE*, 2167:725–736, 1994.

Roger Lecomte. Novel detector technology for clinical PET. *Eur J Nucl Med Mol Imaging*, 36:S69–S85, 2009.

W.R. Leo, editor. *Tecniques for nuclear and particle physics experiment.* Springer Verlag, 1987.

B. Likar, M.A. Viergever, and F. Pernus. Retrospective correction of MR intensity inhomogeneity by information minimization. *Medical Imaging, IEEE Transactions*, 20:1398–1410, 2001.

S. Ljunggren. A simple graphical representation of Fourier-based imaging methods. *J. Magn Resson*, 54 (2):338–343, 1983.

P. Lohmann. Stability and Performance Evaluation of an MR-compatible BrainPET. Master's thesis, University of Applied Sciences, FH Aachen, 2012.

J. Luo, Y. Zhu, P. Clarysse, and I. Magnin. Correction of bias field in MR images using singularity function analysis. *EEE Trans Med Imaging*, 24:1067–1085, 2005.

J.R. Maclaren, P.J. Bones, R.P. Millane, , and R. Watts. Correcting Motion Artifacts in Magnetic Resonance Images. http://pixel.otago.ac.nz/ipapers/22.pdf.

D.W. McRobbie, E.A. Moor, M.J. Graves, and M.R. Prince, editors. *MRI From Picture to Proton*. Cambridge University Press, 2007.

CC. Meltzer, JP. Leal, HS. Mayberg, HN Jr. Wagner, and JJ. Frost. Correction of PET data volume effects in human cerebral cortex by mr imaging. *J Comp Assist Tomo*, 14:561–570, 1990.

P. Mollet, V. Keereman, E. Clementel, and S. Vandenberghe. Simultaneous MR-compatible emission and transmission imaging for PET using time-of-flight information. *IEEE T Med Imag*, 31:1734–1742, 2012.

HW. Müller-Görtner, JM. Links, JL. Prince, RN. Bryan, E. McVeigh, and JP. Leal. Measurement of radio tracer concentration in brain gray matter using positron emission tomography: MRI-based correction for partial volume effects. *J Cereb Blood Flow Metab*, 12:51–58, 1992.

R.V. Olsen, P.L. Munk, M.J. Lee, D.L. Janzen, A.L. MacKay, Q-S Xiang, and B. Masri. Metal Artifact Reduction Sequence: Early Clinical Applications. *Radiographics*, 20:699–712, 2000.

M.E. Phelps, E.J. Hoffman, N.A. Mullani, and M.M. Ter-Pogossian. Application of Annihilation Coincidence Detection to Transaxial Reconstruction Tomography. *J Nucl Med*, 16:210–224, 1974.

J.G. Pipe. Motion correction with PROPELLER MRI: Application to head motion and free-breathing cardiac imaging. *Magn Resson Med*, 42:963–999, 1999.

E.B. Podgorsak, editor. *Radiation Physics for Medical Physicists*. Springer, 2006.

P.V. Prasad, editor. *Magnetic Ressonance Imaging*. Human Press Inc., 2006.

E. Pusey, R.B. Lufkin, R.K.J. Brown, M.A. Solomon, D.D. Stark, R.W. Tarr, and W.N. Hanafee. Magnetic ressonance imaging artefacts: mechanism and clinical significance. *Radigraphics*, 6:891–911, 1986.

J. Rahmer, P. Bornert, J. Groen, and C. Bos. Three-Dimensional Radial Ultrashort Echo-Time Imaging with T2 Adapted Sampling. *Magnetic Resonance in Medicine*, 55::1075–1082, 2006.

MD. Robson, PD. Gatehouse, Bydder M, and GM. Bydder. Magnetic resonance: an introduction to ultrashort TE (UTE) imaging. *J Comp Assist Tomo*, 27:825–846, 2003.

Ye Rong. Development of a user-interface for attenuation template in hybrid MR-BrainPET Imaging. Master's thesis, Aachen University of Applied Sciences, 2009.

E. Rota Kops and H. Herzog. Alternative Methods for Attenuation Correction for PET Images in MR-PET Scanners. *IEEE*, 2007.

E. Rota Kops and H. Herzog. Template based Attenuation Correction for PET in MR-PET Scanners. *IEEE NSS/MIC Conference record, Dresden*, pages 4327–4330, 2008.

E. Rota Kops, H. Herzog, Schmid A, Holte S, and LE. Feinendegen. Performance characteristics of an eight-ring whole body PET scanner. *J Comp Assist Tomo*, 14:437–445, 1990.

E Rota Kops, P. Qin, M. Muller-Veggian, and H. Herzog. MRI Based Attenuation Correction for Brain PET Images. *Advances in Medical Engineering, Springer Proceedings in Physics Volume*, 114:93–97, 2007.

O. Rousset, A. Rahmim, A. Alavi, and H. Zaidi. Partial Volume Correction Strategies in PET. *PET Clinics*, 2:235–249, 2007.

OG. Rousset, Y. Ma, and AC. Evans. Correction for partial volume effects in PET: Principle and validation. *J Nucl Med*, 39:904–911, 1998.

G.B. Saha, editor. *Basics of PTE imaging: Physics, Chemistry, and regulations*. Springer, 2005a.

Gopal B. Saha. *Basics of PET Imaging-Physics, Chemistry, and Regulations*. Springer, 2005b.

A. Salomon, A. Goedicke, B. Schweizer, T. Aach, and V. Schulz. Simultaneous reconstruction of activity and attenuation for PET/MR. *IEEE T Nucl Sci*, 30:804:813, 2011.

H.P.W. Schlemmer, B.J. Pichler, M. Schmand, Z. Burbar, C. Michel, R. Ladebeck, K. Jattke, D. Townsend, C. Nahmias, P.K. Jacob, WD. Heiss, and C.D. Claussen. Silmultaneous MR/PET Imaging of the Human Brain: Feasibility Study. Radiology. *Radiology*, 248:1028–1035, 2008.

E. Schreibmann, T. Fox, J.A. Nye, D.M. Schuster, D.R. Martin, and J. Votaw. MR-based attenuation correction for hybrid PET-MR brain imaging systems using deformable image registration. *Med Phys*, 37: 2101–2109, 2010.

A. Scott, J. Keegan, and Professor David Firmin. Cardiac and respiratory motion in MRI of the heart . *RAD Magazine*, 36:23–24, 2010.

Y. Shao, S.R. Cherry, K. Farahani, K. Meadors, S. Siegel, R.W. Silverman, and P.K. Marsden. Simultaneous PET and MR imaging. *Phys Med Biol*, 42:1965–1970, 1997.

K. Shibuya, E. Yoshida, F. Nishikido, T. Suzuki, T. Tsuda, N. Inadama, T. Yamaya, and H. Murayama. Limit of Spatial Resolution in FDG-PET due to Annihilation Photon Non-Collinearity. *IFMBE Proceedings*, 14:1667–1671, 2007.

Paul Shreve and David W. Townsend. *Clinical PET-CT in Radiology: Integrated Imaging in Oncology*. Springer, 2011.

M. Soret, S.L. Bacharach, and I. Buvat. Partial-Volume Effect in PET Tumor Imaging. *J Nucl Med*, 48:932–945, 2007.

G.J. Stanisz, E.E. Odrobina, J.Phun, M. Escaravage, S.J. Graham, M.J. Bronskill, and R.M. Henkelman. T1, T2 Relaxation and Magnetization Transfer in Tissue at 3T. *Magnetic Resonance in Medicine*, 54:507–512, 2005.

M. Styner, C. Brechbuhler andG. Szekely, and G. Gerig. Parametric estimate of intensity inhomogeneities applied to MRI. *IEEE T Med Imag*, 19:153–165, 2000.

Y. Tai, K. Lain, M. Dahlbom, and E. Hoffman. A hybrid attenuation correction tecnique to compensate for lung density in 3-D total body PET. *IEEE T Nucl Sci*, 43:4543–4561, 1996.

Eiichi Tanaka, Tomohide Ohmura, and Takaji Yamashita. A new method for preventing pulse pileup in scintillation detectors. *Phys Med Biol*, 47:327–339, 2002.

Christopher J. Thompson, Nicole Ranger, Alan C. Evans, and Albert Gjedde. Validation of Simultaneous PET Emission and Transmission Scans. *J Nucl Med*, 32:154–160, 1991.

C.J. Thompson, A. Dagher, D.N. Lunney, S.C. Strother, and A.C.Evans. *International Workshop on Physics and Engineering of Computerized*

Multidimensional Imaging and Processing. SPIE - The International Society for Optical Engin, 1986.

D. Tomazevic, B. Likar, , and F. Pernus. Comparative evaluation of retrospective shading correction methods. *J Microsc*, 208:212–223, 2002.

W. Townsend. *Positron Emission Tomography*. Springer, 2003.

W. Townsend. Physical Principles and Technology of Clinical PET Imaging. *Ann Acad Med Singapore*, 33:133–145, 2004.

D.B. Twieg. The k-trajectory formulation of the NMR imaging process with applications in analysis and synthesis of imaging methods. *Med Phys*, 10 (5):610–621, 1983.

Vadim Kuperman, editor. *Magnetic Ressonance Imaging - Physical Principles and Applications*. Academic Press, 2000.

U. Vovk, F. Pernus, and B. Likar. Intensity inhomogeneity correction of multispectral MR images. *NeuroImage*, 32:54–61, 2006.

G. Wagenknecht, E. Rota Kops, L. Tellmann, and H. Herzog. Knowledge-based segmentation of attenuation-relevant regions of the head in T1-weighted MR images for attenuation correction in MR/PET systems. *IEEE NSS/MIC Conference record, Orlando*, pages 2530–2533, 2009.

J.P. Wansapura and S.K. Holland. NMR Relaxation times in the human brain at 3.0T. *J. Magn Resson Imaging*, 9:531:538, 1999.

C.C. Watson, A. Schaefer, W.K. Luk, and C.M. Kirsch. Clinical Evaluation of Single-Photon Attenuation Correction for 3D Whole-Body PET. *IEEE*, 46:1024–1031, 1999.

W.M. Wells, W.E.L. Grimson, R. Kikinis, and F.A. Jolesz. Adaptive segmentation of MRI data. *IEEE T Med Imag*, 15:429–442, 1996.

T.Z. Wong, R.E. Coleman, R.J. Hagge, S. Borges-Neto, and M.W. Hanson. PET Image Interpretation: Attenuation-Corrected (ATN) Vs Non-Attenuation Corrected (NATN) Images. *Clinical Positron Imaging*, 3, Issue 4:181, 2000.

M. Xu, P. D. Cutler, and W. K. Luk. Adaptive, Segmented Attenuation Correction for Whole-Body PET Imaging. *IEEE*, 43:331–336, 1996.

Siu K Yu and C. Nahmias. Segmented attenuation correction using artificial neural networks in positron tomography. *Phys Med Biol*, 41: 2189–2206, 1996.

H. Zaidi and B. Hasegawa. Determination of the Attenuation Map in Emission Tomography. *J Nucl Med*, 44:291–315, 2003.

H. Zaidi, ML. Montandon, and D.O. Slosman. Magnetic resonance imaging-guided attenuation and scatter corrections in three-dimensional brain positron emission tomography. *Med Phys*, 30:937–949, 2003.

Habib Zaidi, Marie-Louise Montandon, and Abass Alavi. Advances in Attenuation Correction Techniques in PET. *PET Clin*, 2:191–217, 2007.

S. Ziegler. Positron Emission Tomography: Principles, Technology, and Recent Developments. *Nucl Phys A*, 752:679–687, 2005.

Chapter 8

Annex A

The work developed during this master thesis lead already to the publication of one of the proposed methods, the Probabilistic Neural Network. The advantage of this method over the current methods is that a quick and an easy parameter optimization can be achieved. The publish article at the Nuclear Instruments & Methods In Physics Research A (2012), `http://dx.doi.org/10.1016/j.nima.2012.09.005` is disponibilized here.

Nuclear Instruments and Methods in Physics Research A ▮ (▮▮▮▮) ▮▮▮–▮▮▮

Contents lists available at SciVerse ScienceDirect

Nuclear Instruments and Methods in Physics Research A

journal homepage: www.elsevier.com/locate/nima

Skull segmentation of UTE MR images by probabilistic neural network for attenuation correction in PET/MR

A. Santos Ribeiro [a,b], E. Rota Kops [b,*], H. Herzog [b], P. Almeida [a]

[a] Institute of Biophysics and Biomedical Engineering, Lisbon, Portugal
[b] Forschungszentrum Juelich, INM4, Juelich, Germany

ARTICLE INFO

Keywords:
PET/MRI
Attenuation correction
Ultrashort echo time
Probabilistic neural network
Bone segmentation
Dice coefficients

ABSTRACT

Aim: Due to space and technical limitations in PET/MR scanners one of the difficulties is the generation of an attenuation correction (AC) map to correct the PET image data. Different methods have been suggested that make use of the images acquired with an ultrashort echo time (UTE) sequence. However, in most of them precise thresholds need to be defined and these may depend on the sequence parameters. In this study an algorithm based on a probabilistic neural network (PNN) is presented requiring little user interaction. *Material and methods:* An MR UTE sequence delivering two images (UTE1 and UTE2) by using two different echo times (0.07 ms and 2.46 ms, respectively) was acquired. The input features for the PNN algorithm consist of two patches of MR intensities chosen in both the co-registered UTE1 and UTE2 images. At the end, the PNN generates an image classified into four different classes: brain+soft tissue, air, csf, and bone. CT and MR data were acquired in four subjects, whereby the CT data were used for comparison. For each patient co-classification of the different classified classes and the Dice coefficients (D) were calculated between the MR segmented image and the respective CT image. *Results:* An overall voxel classification accuracy (compared with CT) of 92% was obtained. Also, the resulting D with regard to the skull and calculated for the four subjects show a mean of 0.83 and a standard deviation of 0.07. *Discussion:* Our results show that a reliable bone segmentation of MRI images as well as the generation of a reliable attenuation map is possible. *Conclusion:* The developed algorithms possess several advantages over current methods using UTE sequence such as a quick and an easy optimization for different sequence parameters.

1. Introduction

Due to lack of space and technical limitations in PET/MR scanners one main difficulty is the generation of an attenuation correction (AC) map to correct the PET image data. Several methods have been suggested to obtain the AC map from MR images whereby the main problem is that the signal for cortical bone from anatomical T1-weighted MR sequences is very low and similar to the air signal. One method relies at some extent on general anatomical knowledge [1] while other methods are based on other sequences than the T1-weighted one, such as the ultrashort echo time (UTE) sequence [2,3]. For these last methods precise thresholds need to be defined to accurately segment the MR images into three classes (bone, air and soft tissue). Furthermore, these thresholds may depend on the different sequence parameters. In this study one algorithm based on a probabilistic neural network (PNN) is presented requiring little user interaction. In addition the AC map is derived without any a priori anatomical assumption. A comparison with corresponding segmented CT images is presented, showing the co-classification of voxels and the Dice coefficients (D) for three different classes (air, bone and soft tissue) present in the field of view (FOV) of a 3 T MR/BrainPET scanner. Moreover, bone tissue was divided into three different regions (skull, occipital bone and facial+neck) and the Dvalues calculated for each region.

2. Material and methods

2.1. Data acquisition

CT and MR data were acquired in four subjects (one female and three males). The CT data were acquired on different scanners with different standard parameters. The MR UTE sequence installed at the 3 T MR/BrainPET scanner in the Forschungszentrum Juelich Lab was acquired with a flip angle=15°, two different echo times TE1=0.07 and TE2=2.46 ms, and TR=200 ms, resulting in 192 sagittal 192 × 192 images with a voxel size of 1.67 mm^3. Corresponding to the

* Corresponding author.
E-mail address: e.rota.kops@fz-juelich.de (E. Rota Kops).

0168-9002/$ - see front matter © 2012 Elsevier B.V. All rights reserved.
http://dx.doi.org/10.1016/j.nima.2012.09.005

different echo times, two images (UTE1 and UTE2) are delivered. The developed PNN algorithm utilizes information obtained from these two images.

2.2. PNN architecture

PNN consists of a feed-forward neural network with three layers shown in Fig. 1: an input layer (IL), a pattern layer (PL), and a summation layer (SL). Our aim is to obtain four distinct classes: brain+soft tissue, csf, bone, and air. Thus, the SL consists of four nodes corresponding to these four different classes. The PL consists of four pools, each corresponding to the four nodes of SL and each being built up of previously chosen training data of the corresponding classes to be segmented. The IL, representing the input features, feeds PNN.

2.3. PNN procedure

In this study the input features consist of two patches of MR intensities around a voxel of interest (VxOI) together with the six closest neighbors chosen in both the co-registered UTE1 and UTE2 images. The two obtained patches are stored in a vector that will be used in both training and classification steps.

In the training step $Ni=3$ example vectors (or training vectors) obtained from a training data set are stored for each class (Ci) to be classified and are given to the corresponding nodes in PL.

In the classification step the vector to be classified (segmenting vector) is obtained for every voxel (VxOI) and is given to the nodes in IL.

The output of the nodes in PL is calculated based on the combination of a radial basis function (RBF) with a Gaussian activation function and is given by

$$Oi_{PL} = \exp\left(\frac{-|x-Ti|^2}{2\sigma^2}\right) \quad (1)$$

where Oi_{PL} is the output of each node in PL, x is the segmenting vector in IL, Ti is the training vector in PL, and sigma (σ) the smoothing factor.

The output of the nodes in SL (segmented classes) calculated by a weighted summation of the nodes in PL that are connected to each of them is thus obtained by

$$p(x|Ci) = \frac{1}{Ni(2\pi)^{d/2}\sigma^d}\sum_{n=1}^{Ni} Oi_{PL} \quad (2)$$

where $p(x|Ci)$ is the probability density function of class Ci and d the dimension of the input vector.

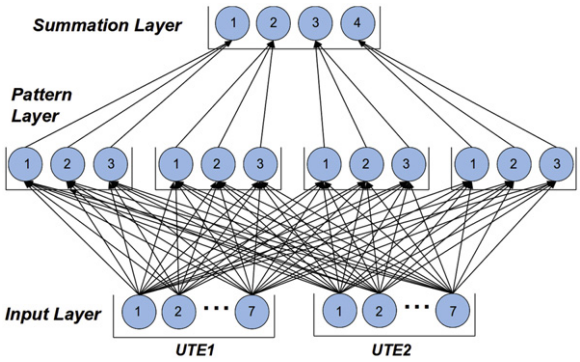

Fig. 1. Architecture of the proposed. PNN has three layers (SL, PL, and IL) with seven input nodes from UTE1 and seven input nodes from UTE2 in IL, four poles of three pattern nodes in PL, and four output nodes in SL.

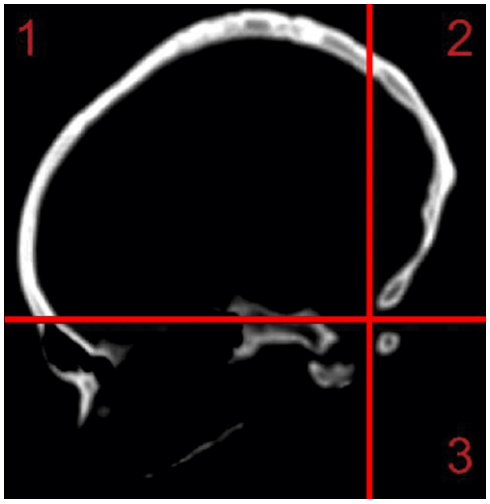

Fig. 2. Illustration of the three different regions (1 and 2—pure skull, 2—occipital bone, 3—facial and neck) for calculation of the Dice coefficients.

For each input feature in IL, PNN calculates the probability to be a member of one of the four different classes and assigns the current VxOI to the class with the highest probability.

2.4. Data processing and data analysis

After bias correction of MR inhomogeneities the PNN algorithm was applied to the UTE images for classification. As the purpose of this segmentation is to generate an AC map with three classes (bone, soft tissue and air), the voxels classified as csf were assigned the same class as soft tissue.

For each patient the co-classification of voxels

$$C_{class} = \sum(VOX_{CT} \bigcap VOX_{PNN}) \quad (3)$$

and the D values

$$D_{value} = \frac{2\times\sum(VOX_{CT} \bigcap VOX_{PNN})}{\sum(VOX_{CT})+\sum(VOX_{PNN})} \quad (4)$$

between the generated image and the respective CT image were obtained.

Motion artefacts presented in the MR images induce large errors in the classification of the images. Specifically, it induces blurring in the lower portion of the head (facial region) and in the neck region of the patients. These artefacts induced an over-classification of bone tissue in these regions. Therefore, both the co-classification and Dvalues give misleading results when they are applied to the entire bone. Consequently, Dvalues were calculated separately for the (whole) head and three different regions (Fig. 2 pure skull (1+2), facial+neck (3), and occipital bone (2)).

3. Results

The generated classified image exhibits a high visual similarity to the segmented CT image, with higher similarity for the skull and brain region and lower similarity for the facial and neck region, Fig. 3.

The fraction of correctly classified voxels was 92% aggregated over all patients (calculated from Table 1). Both air and soft tissue regions present high Dvalues, with approximately 0.97 and 0.85, respectively. Bone tissue region presented the lowest Dvalue ($D=0.53$). Misclassification of tissues showed to be low for air–soft/soft–air and air–bone/bone–air regions as can be observed by

Please cite this article as: A. Santos Ribeiro, et al., Nuclear Instruments & Methods In Physics Research A (2012), http://dx.doi.org/10.1016/j.nima.2012.09.005

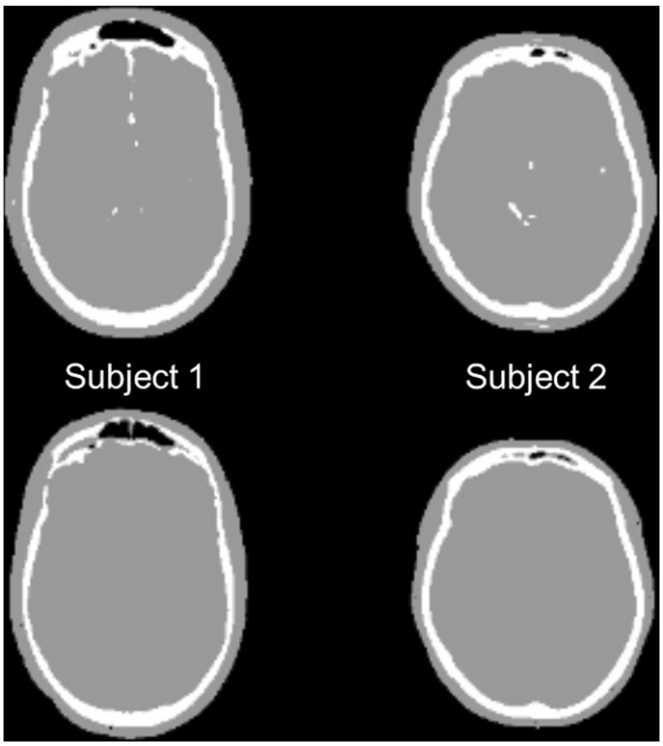

Fig. 3. Comparison between PNN segmentation (top) and CT (bottom) for two different subjects. Black corresponds to air, gray to brain+soft tissue+csf, white to bone.

Table 1
Co-classification of voxel classes between CT and images classified with PNN. The number of voxels intersecting the segmented tissue classes are aggregated over all four patients. In brackets is the Dice coefficients for each combination of tissues.

CT/PNN	Air	Soft	Bone	Total
Air	27,465,249 (0.97)	1,281,993 (0.06)	89,507 (0.01)	28,836,749
Soft	333,904 (0.02)	10,292,305(0.85)	1,606,721 (0.20)	12,232,930
Bone	21,006 (0.00)	281,289 (0.04)	1,975,419 (0.66)	2,277,714
Total	27,820,159	11,855,587	3,671,647	43,347,393

the low *D*values. Also, misclassification of bone–soft was low, yet misclassification of soft–bone is significant, therefore showing an over-classification of bone tissue in soft tissue region.

The *D*values for the whole head (e.g. for the FOV of the 3 T MR/BrainPET scanner) shows a mean ($\pm$ standard deviation) of 0.66 $\pm$ 0.07. The region of the head that shows the best result is the skull with a *D*value of 0.83 $\pm$ 0.07. The region that shows the most problematic results is the facial and neck region with a *D*value of 0.44 $\pm$ 0.06.

4. Discussion

Our results show that a reliable classification of air, bone and soft tissue classes of MR images is possible with the PNN algorithm. The algorithm showed high values for the co-classification of air and soft tissue classes. Compared to a recent method proposed by Berker et al. [4], our approach shows an overall co-classification higher than the one presented by Berker's article (92% vs 81%). Also, our method presents higher *D*values for all three classes: air (0.97 vs 0.92), soft tissue (0.85 vs 0.83) and bone (0.66 vs 0.54). Nonetheless, for air the

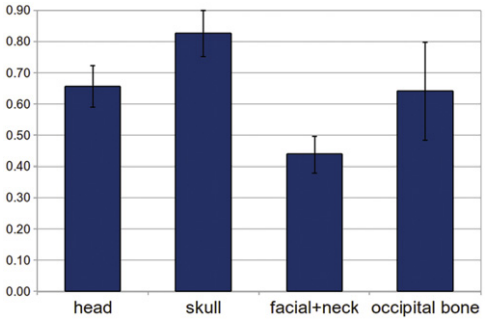

Fig. 4. Chart of the Dice coefficients for the whole head and the three different regions.

*D*value is highly dependent on the bounding box chosen and comparison between both techniques should be taken with care. For bone due to the amount of artefacts presented in the obtained images the *D*values give misleading results when they are applied to the entire bone.

In Fig. 4, very low *D*values were obtained for the facial+neck region, explaining the low co-classification and *D*values obtained for bone for the whole head. In opposite, the skull presented high *D*values, demonstrating the accuracy of the method for the classification of bone. Also, the occipital bone presented yielded acceptable results, whereby this region is normally difficult to segment accurately.

Nevertheless, some minor misclassification in the brain tissue was observed (Fig. 3). These results are inherent of the PNN algorithm, as the algorithm is based on the raw intensities of the MR-UTE images and no enhancement is performed as was done in the Keereman et al. [2], Catana et al. [3] or Berker et al. [4] methods. Moreover, the performance of our algorithm may be affected if the MR intensities differ substantially between patients, even if the ratio between the first echo and the second echo images is maintained.

5. Conclusion

The developed algorithm presented in this work shows advantages over current methods using the UTE sequence such as a quick and an easy optimization of the PNN in the case of different sequence parameters, whereby optimization of parameters of methods such as Keereman et al. [2] and Catana et al. [3] are not trivial. The method also proved to be robust and accurate to different patients where motion artefacts were not present. Finally, the final outcome of our method can only be tested with reconstructed PET data and this is work in progress.

References

[1] E. Rota Kops, G. Wagenknecht, J. Kaffanke, L. Tellmann, F. Mottaghy, M. Piroth, H. Herzog, Attenuation correction in MR-PET scanners with segmented T1-weighted MR images, in: Nuclear Science Symposium Conference Record, 2010.
[2] V. Keereman, Y. Fierens, T. Broux, Y.D. Deene, M. Lonneux, S. Vandenberghe, Journal of Nuclear Medicine 51 (2010) 812.
[3] C. Catana, A. van der Kouwe, T. Benner, C.J. Michel, M. Hamm, M. Fenchel, B. Fishl, B. Rosen, M. Schmand, A.G. Sorensen, Journal of Nuclear Medicine 51 (2010) 1431.
[4] Y. Berker, J. Franke, A. Salomon, M. Palmowski, H. Donker, Y. Temur, F. Mottaghy, C. Kuhl, D. Izquierdo-Garcia, Z. Fayad, F. Kiessling, V. Schulz, Journal of Nuclear Medicine 53 (2012) 796.

Please cite this article as: A. Santos Ribeiro, et al., Nuclear Instruments & Methods In Physics Research A (2012), http://dx.doi.org/10.1016/j.nima.2012.09.005

Chapter 9

Annex B

The full parameters of the Brainweb simulation for evaluation of the proposed bias correction algorithm with simulated T1, T2 and PD brain images is presented.

BrainWeb: custom MRI simulations request

Please choose the parameters for your simulation:

Simulation model (phantom)		
Phantom :	normal	
MR pulse sequence		
Set all parameters from template: T1 pulse sequence, and ICBM protocol. and/or customize the individual parameters below:		
Slice thickness [mm] :	1	this also specifies the amount of partial volume artifact; note that the in-plane pixel size is always 1x1mm range: 1...10
Scan technique :	SFLASH (spoiled FLASH)	type of pulse sequence
Repetition time (TR) [ms] :	18	
Inversion time (TI) [ms] :		only used for the inversion recovery (IR) pulse sequence
Flip angle [deg] :	30	ignored for all SE, DSE* and IR sequences (these use a fixed excitation flip angle of 90 deg) range: 1...150
Echo time(s) (TE) [ms] :	10	all pulse sequences use only one echo time, except the DSE_EARLY and DSE_LATE sequences which need two echo times separated by a comma (,)
Image Type :	magnitude	type of reconstructed output image
Imaging artifacts		
Noise reference tissue :	(brightest_tissue)	tissue that is to be used as a reference for the percent noise calculation (see below)
Noise level [%] :	3	the standard deviation of the gaussian noise that is to be added to the real and imaginary channels is given by the noise percent multiplied by the reference tissue intensity range: 0...100
Random generator seed :	1	seed used to initialize the random number generator used for noise simulations; if zero, a new pseudo-random seed will be generated everytime range: 0...2147483647
INU field :	field A	choice of a synthetic INU field shape; all of them are based on fields observed in real MR scans
INU ("RF") level [%] :	0	specifies the intensity non-uniformity level (a negative value inverts the field) range: -100...100

Your email :		When the requested simulation is completed, you will be notified at this address. NOTE: it is very important to correctly enter a valid email address, otherwise you won't be able to retrieve the data that you requested!

[Done] Undo changes

BrainWeb: custom MRI simulations request

Please choose the parameters for your simulation:

Simulation model (phantom)		
Phantom :	normal	
MR pulse sequence		
Set all parameters from template: T2 pulse sequence, and ICBM protocol. and/or customize the individual parameters below:		
Slice thickness [mm] :	1	this also specifies the amount of partial volume artifact; note that the in-plane pixel size is always 1x1mm range: 1...10
Scan technique :	DSE_LATE (dual echo spin echo, late echo)	type of pulse sequence
Repetition time (TR) [ms] :	3300	
Inversion time (TI) [ms] :		only used for the inversion recovery (IR) pulse sequence
Flip angle [deg] :	90	ignored for all SE, DSE* and IR sequences (these use a fixed excitation flip angle of 90 deg) range: 1...150
Echo time(s) (TE) [ms] :	35, 120	all pulse sequences use only one echo time, except the DSE_EARLY and DSE_LATE sequences which need two echo times separated by a comma (,)
Image Type :	magnitude	type of reconstructed output image
Imaging artifacts		
Noise reference tissue :	(brightest_tissue)	tissue that is to be used as a reference for the percent noise calculation (see below)
Noise level [%] :	3	the standard deviation of the gaussian noise that is to be added to the real and imaginary channels is given by the noise percent multiplied by the reference tissue intensity range: 0...100
Random generator seed :	2	seed used to initialize the random number generator used for noise simulations; if zero, a new pseudo-random seed will be generated everytime range: 0...2147483647
INU field :	field B	choice of a synthetic INU field shape; all of them are based on fields observed in real MR scans
INU ("RF") level [%] :	0	specifies the intensity non-uniformity level (a negative value inverts the field) range: -100...100

Your email :		When the requested simulation is completed, you will be notified at this address. NOTE: it is very important to correctly enter a valid email address, otherwise you won't be able to retrieve the data that you requested!

[Done] Undo changes

BrainWeb: custom MRI simulations request

Please choose the parameters for your simulation:

Simulation model (phantom)		
Phantom :	normal	
MR pulse sequence		
Set all parameters from template: PD pulse sequence, and ICBM protocol. and/or customize the individual parameters below:		
Slice thickness [mm] :	1	this also specifies the amount of partial volume artifact; note that the in-plane pixel size is always 1x1mm range: 1...10
Scan technique :	DSE_EARLY (dual echo spin echo, early echo)	type of pulse sequence
Repetition time (TR) [ms] :	3300	
Inversion time (TI) [ms] :		only used for the inversion recovery (IR) pulse sequence
Flip angle [deg] :	90	ignored for all SE, DSE* and IR sequences (these use a fixed excitation flip angle of 90 deg) range: 1...150
Echo time(s) (TE) [ms] :	35, 120	all pulse sequences use only one echo time, except the DSE_EARLY and DSE_LATE sequences which need two echo times separated by a comma (,)
Image Type :	magnitude	type of reconstructed output image
Imaging artifacts		
Noise reference tissue :	(brightest_tissue)	tissue that is to be used as a reference for the percent noise calculation (see below)
Noise level [%] :	3	the standard deviation of the gaussian noise that is to be added to the real and imaginary channels is given by the noise percent multiplied by the reference tissue intensity range: 0...100
Random generator seed :	3	seed used to initialize the random number generator used for noise simulations; if zero, a new pseudo-random seed will be generated everytime range: 0...2147483647
INU field :	field C	choice of a synthetic INU field shape; all of them are based on fields observed in real MR scans
INU ("RF") level [%] :	0	specifies the intensity non-uniformity level (a negative value inverts the field) range: -100...100

Your email :		When the requested simulation is completed, you will be notified at this address. NOTE: it is very important to correctly enter a valid email address, otherwise you won't be able to retrieve the data that you requested!

[Done] Undo changes

Chapter 10

Annex C

The reconstruction of the obtained PET images with the proposed methods (masked for brain tissue) from which the relative differences between MR-AC and Scaled CT-AC maps were calculated (Figure 6.20). Visually no high differences are observed between the different methods.

d−pnn (ute)

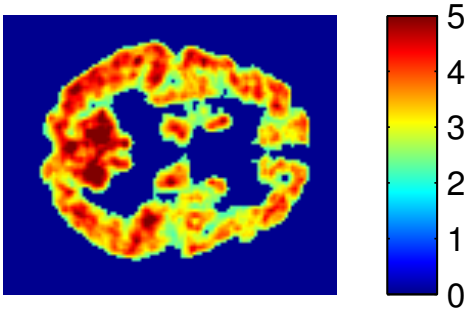

d−ffnn (ute)

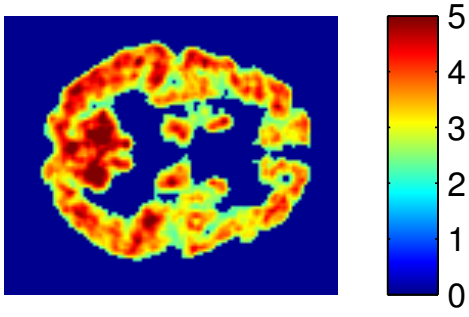

d−pnn (ute+template)

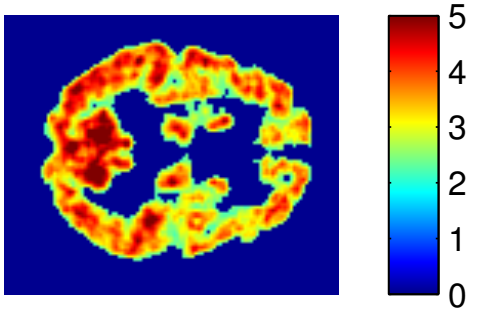

d−ffnn (ute+template)

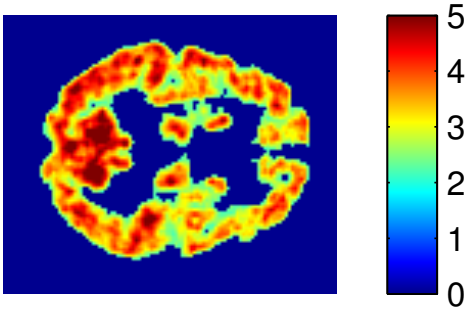

s−ffnn

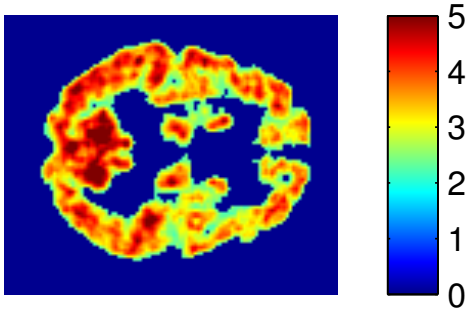

s−som

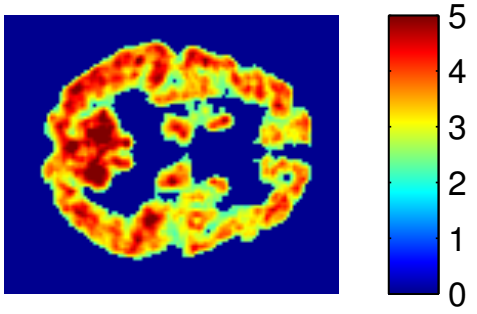

d−catana

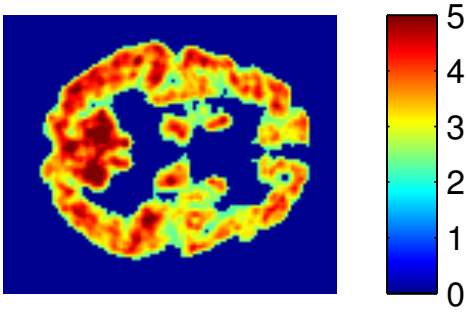

d−keereman

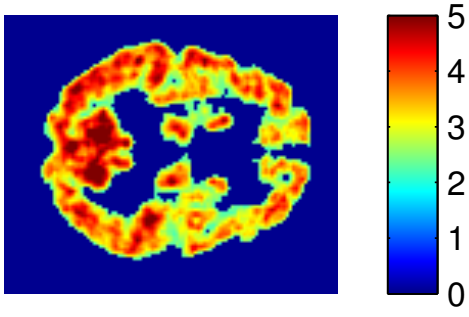

s−template

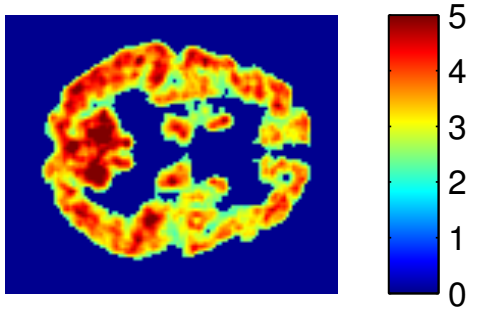

d−ct

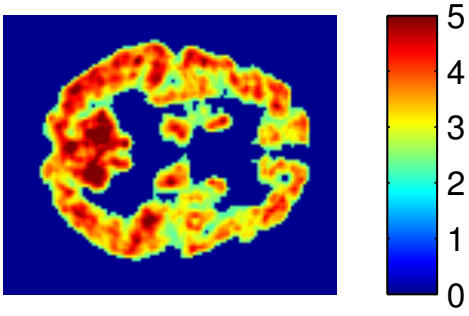

s−ct